

AD-A079 980

RAYTHEON CO WALTHAM MASS RESEARCH DIV  
P-TYPE GALLIUM ARSENIDE EPITAXIAL GROWTH. (U)  
AUG 79 S R STEEL, K K JOHNSON

F/G 20/12

F33615-78-C-1456

UNCLASSIFIED

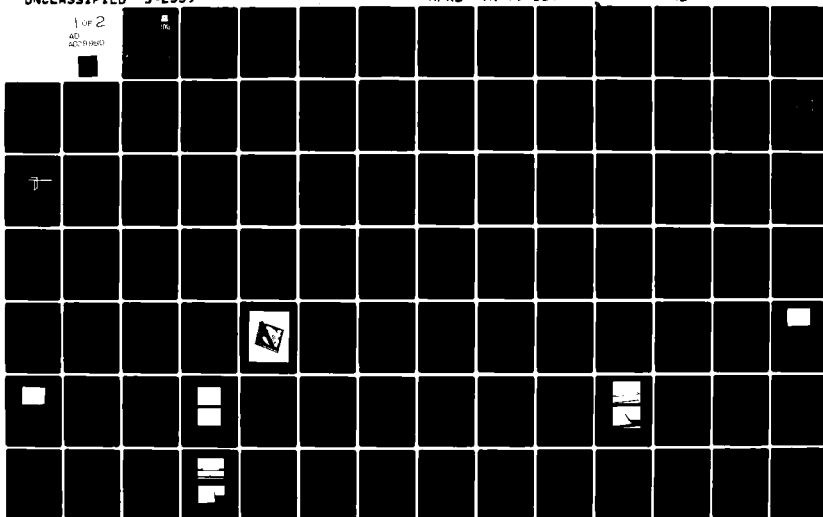
S-2559

AFAL -TR-79-1144

NL

1 OF 2

AD  
A079980



AFAL-TR-79-1144

P-TYPE GALLIUM ARSENIDE EPITAXIAL GROWTH

ADA079980

Raytheon Company  
28 Seyon Street  
Waltham, Massachusetts 02154

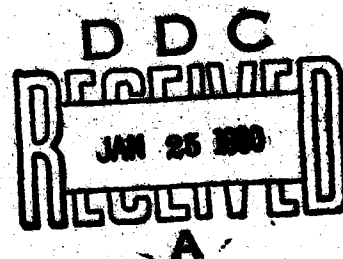
October 24, 1979

TECHNICAL REPORT AFAL-TR-79-1144

Final Report for Period 22 May 1978 to 22 May 1979

Approved for public release; distribution unlimited.

AIR FORCE AVIONICS LABORATORY  
AIR FORCE WRIGHT AERONAUTICAL LABORATORIES  
AIR FORCE SYSTEMS COMMAND  
WRIGHT-PATTERSON AIR FORCE BASE, OHIO 45433



80 1 25 057

DDC FILE COPY

# NOTICE

When Government drawings, specifications, or other data are used for any purpose other than in connection with a definitely related Government procurement operation, the United States Government thereby incurs no responsibility nor any obligation whatsoever, and the fact that the government may have formulated, furnished, or in any way supplied the said drawings, specifications, or other data, is not to be regarded by implication or otherwise as in any manner licensing the holder or any other person or corporation, or conveying any rights or permission to manufacture, use, or sell any patented invention that may in any way be related thereto.

This report has been reviewed by the Information Office (OI) and is releasable to the National Technical Information Service (NTIS). At NTIS, it will be available to the general public, including foreign nations.

This technical report has been reviewed and is approved for publication.

Gary L McCoy

Richard Z Renshaw

FOR THE COMMANDER

William B. Shuman

"If your address has changed, if you wish to be removed from our mailing list, or if the addressee is no longer employed by your organization please notify AFAL/DHM-1, W-PAFB, OH 45433 to help us maintain a current mailing list".

Copies of this report should not be returned unless return is required by security considerations, contractual obligations, or notice on a specific document.

SECURITY CLASSIFICATION OF THIS PAGE (When Data Entered)

19 REPORT DOCUMENTATION PAGE		READ INSTRUCTIONS BEFORE COMPLETING FORM	
1. REPORT NUMBER 18 AFAL TR-79-1144 /		2. GOVT ACCESSION NO.	
3. TITLE (and Subtitle) P-Type Gallium Arsenide Epitaxial Growth		4. RECIPIENT'S CATALOG NUMBER 9	
5. AUTHOR(s) 10 S. R. Steele, A. D. Barlas K. K. Johnson, L. Holway, Jr B. D. Lauterwasser,		6. TYPE OF REPORT & COVER SHEET Final Technical Report 22 May 1978 - 22 May 1979	
7. PERFORMING ORGANIZATION NAME AND ADDRESS Raytheon Research Division 28 Seyon Street Waltham, Massachusetts 02154		8. CONTRACT OR GRANT NUMBER(s) 14 S-2559	
9. CONTROLLING OFFICE NAME AND ADDRESS AFAL/DHR, WPAFB, OH 45433		10. PROGRAM ELEMENT, PROJECT, TASK AREA & WORK UNIT NUMBERS 15 F33615-78-C-1456	
11. MONITORING AGENCY NAME & ADDRESS (if different from Controlling Office)		12. REPORT DATE 16 2002-01-46 17 01	
13. DISTRIBUTION STATEMENT (of this Report) approved for public release; distribution unlimited.		14. SECURITY CLASS. (of this report) Unclassified	
15. DISTRIBUTION STATEMENT (of the abstract entered in Block 20, if different from Report)		16. DECLASSIFICATION/DOWNGRADING SCHEDULE	
17. SUPPLEMENTARY NOTES			
18. KEY WORDS (Continue on reverse side if necessary and identify by block number) double-drift IMPATT diodes, Read-type diodes, epitaxial gallium arsenide, p-type dopants, zinc iodide, zinc alkyls, hole saturation velocity, hole ionization coefficients			
19. ABSTRACT (Continue on reverse side if necessary and identify by block number) At the beginning of this program, the rapid development of double-drift GaAs IMPATT diodes at X-band was being retarded by limited knowledge of the optimum growth conditions and the basic physical properties of p-type GaAs. Although p-type material with doping levels suitable for X-band double-drift devices was grown before this program began, profile control was sometimes erratic and wafer yield was poor. There was also a serious			

DD FORM 1 JAN 73 1473

EDITION OF 1 NOV 65 IS OBSOLETE

SECURITY CLASSIFICATION OF THIS PAGE (When Data Entered)

272 320

500

need for further data on hole velocities and ionization coefficients at the temperatures and electric fields existing in double-drift devices. This program set out to address these problems.

In the first task of this program, we explored three p-type doping techniques, one involving zinc alkyl, and two involving zinc iodide formed as needed by chemical reaction. The zinc alkyl process was found to be chiefly useful for p++ contacts; the two zinc iodide processes gave useful p-doping at levels suitable for devices from X- to Ka-band.

In the second task of this program, we measured hole velocities as a function of electric field and temperature. <sup>which</sup> Our velocities averaged about 70 percent of those reported previously. We also determined ionization coefficients at very high fields ( $6 \times 10^5$  v/cm) typical of high power Ka-band devices. These are in rough agreement with values reported earlier.

In the third task, we grew X-band and Ka-band p-type low-high-low Read wafers with good reproducibility, using the zinc iodide formed as needed by chemical reaction.

### FOREWORD

This final report was submitted by Raytheon Research Division, under Contract No. F33615-78-C-1456, with the Air Force Avionics Laboratory, Air Force Systems Command, Wright Patterson Air Force Base, Ohio. Mr. Gary McCoy is the Laboratory Project Engineer.

The work was performed in the semiconductor laboratory, Raytheon Research Division, Waltham, Massachusetts. The Semiconductor Laboratory Manager is Mr. R. W. Bierig. The Program Manager was Mr. S. R. Steele. The growth experiments using  $I_2 + HI$ , as well as the growth of hole velocity wafers, were directed by Ms. K. K. Johnson. The p-Read wafers were grown by Dr. B. D. Lauterwasser. The measurement samples were prepared under the direction of Dr. M. G. Adlerstein. The physical measurements were carried out under the direction of Dr. L. H. Holway, Jr. Wafer characterization was performed under the direction of Dr. A. D. Barlas. The SEM photographs were prepared by Dr. O. Guentert.

This report was given the Raytheon internal document number S-2559.

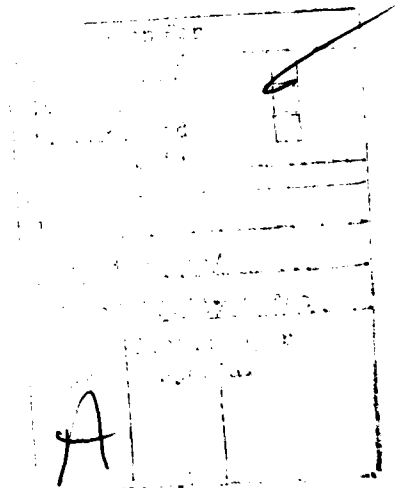


## TABLE OF CONTENTS

<u>SECTION</u>	<u>PAGE</u>
I <u>INTRODUCTION</u> .....	1
1.1   Objective .....	1
1.2   Goals .....	1
1.3   Tasks .....	2
1.3.1   Task I:   Epitaxial growth experiments .....	2
1.3.2   Task II:   Physical Measurements .....	2
1.2.3   Task III:   Demonstration growth of p-Read structures .....	3
1.4   Summary .....	3
II <u>EPITAXIAL GROWTH EXPERIMENTS</u> .....	4
2.1   Introduction .....	4
2.2   p-Doping Techniques .....	4
2.2.1   Introduction .....	4
2.2.2   Direct vaporization .....	5
2.2.3   Doped source .....	6
2.2.4   Zinc alkyls .....	6
2.2.5   Zinc iodide doping .....	7
2.3   Epitaxial Growth System .....	8
2.3.1   Introduction .....	8
2.3.2   Microprocessor control .....	8
2.3.3   Gas-handling system .....	11
2.3.4   Doping networks .....	11
2.3.5   p-doping by reactive transport .....	12
2.4   Reactive Transport Experiments .....	16
2.4.1   HI reactive transport .....	17
2.4.2   I <sub>2</sub> reactive transport .....	20
2.4.3   Comparison of HI and I <sub>2</sub> reactive transport doping methods .....	24

# TABLE OF CONTENTS (Continued)

<u>SECTION</u>	<u>PAGE</u>
2.5 Run Procedures .....	28
2.6 Growth of Multilayer Structures .....	29
2.7 $n^{++}p$ Junction Growth .....	35
2.8 p-Read Growth .....	36
III <u>WAFER CHARACTERIZATION</u> .....	45
3.1 Introduction .....	45
3.2 Measurement Technique .....	45
3.3 System Description .....	48
3.4 Limitations of p-GaAs Material Characterization .....	50
3.5 Evaluation of p-n Junctions .....	54
IV <u>HOLE VELOCITY MEASUREMENTS</u> .....	61
4.1 Introduction .....	61
4.2 Measurement Technique .....	65
4.2.1 Determination of area and doping densities .....	65
4.2.2 Experimental setup .....	65
4.2.3 Thermal effects .....	69
4.2.4 Data validation .....	71
4.3 Data Reduction Methods .....	75
4.4 Results .....	78
4.5 Discussion of the Results .....	85
V <u>IONIZATION COEFFICIENTS IN GaAs</u> .....	89
5.1 Introduction .....	89
5.2 Measurements .....	91
5.3 Data Reduction .....	93
5.3.1 Wafer 33205 .....	93
5.3.2 Other Wafers .....	105
5.4 Results .....	108
5.5 Discussion of Results .....	110



TABLE OF CONTENTS (Continued)

<u>SECTION</u>	<u>PAGE</u>
VI PROGRAM ACHIEVEMENTS AND RECOMMENDATIONS .....	112
6.1 Introduction .....	112
6.2 Overall Results .....	112
6.2.1 Epitaxial growth .....	113
6.2.2 Wafer characterization .....	113
6.2.3 Physical measurements .....	115
6.3 Deliveries .....	115
6.4 Recommendations for Future Work .....	115
REFERENCES .....	117

# LIST OF ILLUSTRATIONS

<u>FIGURE</u>	<u>TITLE</u>	<u>PAGE</u>
1	Schematic Diagram of VPE System, Showing Doping Networks and Reactor Geometry.	9
2	Block Diagram of Microprocessor - VPE System Interaction.	10
3	Diagram of Iodine Vaporizer.	14
4	Diagram of Retort and Heated Line.	15
5	Partial Pressures of Zn over Zinc Arsenide, Zinc, and Zinc Iodide as a Function of Temperature.	18
6	Hole Concentrations Obtained at Various Zinc Arsenide Temperatures with a Constant HI and Dilute Gas Flow.	21
7	Hole Concentrations Experimentally Obtained as a Function of Iodine Concentration with Various Retort and I <sub>2</sub> Vaporizer Temperatures and Hydrogen or Helium as the I <sub>2</sub> Carrier Gas.	23
8	P-Doping Profiles on Silicon-Doped Substrates Produced at Various Retort Temperatures using 0.14 ppm I <sub>2</sub> .	25
9	Doping Profile of Wafer 51333.	26
10	Map of Surface Capacitance of Wafer 51333.	27
11	Doping Profile of Wafer 51306.	33
12	Doping Profile of Wafer 51310.	34
13	X-Band P-Type Wafer Profile.	41
14	Ka-Band P-Type Wafer Profile.	42
15	Characterization Sample Showing the 8 Diodes at Different Depth.	47
16	Block Diagram of the Digital Profiler.	49
17	Doping Profile for Wafer 91301 Reconstructed from C-V Data Taken from Several Step-Etched Schottky Barrier Diodes.	51
18	Doping Profile for Wafer 91301-1 Reconstructed from Third and Fourth Etch-Step of Schottky Barrier Diodes.	53
19	Surface Capacitance Map of Wafer 51636.	55
20	Junction Capacitance Map of Wafer 51618.	56
21	Junction Capacitance Map of Wafer 51631.	57
22	Mesa Structures Using Two Different Ohmic Contacts	59
23	Improved I-V Characteristics of 3 Mil Mesas.	60

LIST OF ILLUSTRATIONS (Continued)

<u>FIGURE</u>	<u>TITLE</u>	<u>PAGE</u>
24	Schematic Diagram of Simplest Hole Velocity Experiment.	63
25	Sample Geometry for Experiment.	64
26	Microphotograph of Mesa Device.	67
27	Diagram of the Equipment for Hole-Velocity Measurements.	68
28	Current from VMS-270, Device No. 8.	70
29	Variation of I-V Plots from Leading Edge to Trailing Edge of Pulse in VMS-270, Device No. 12.	72
30	I-V Measurements on Five Devices from Wafer No. 51306.	73
31	Sample No. 3 at 440X and 2200X Magnification.	74
32	I-V Curves.	76
33	The Solid Curve is the Measured I-V Curve Renormalized to $v_{app}$ and $\bar{E}$ .	77
34	Change of Electric Field Due to the Changing Cross Section and Doping Nonuniformity in Device No. 7.	80
35	The Solid Curve is the $v(E)$ Curve, which has been used to Calculate the Dotted Curve, which is Normalized Version of the Expected I-V Curve.	81
36	Velocity-Field Characteristics for $T = -18^{\circ}\text{C}$ , $26^{\circ}\text{C}$ , and $99^{\circ}\text{C}$ .	83
37	Saturated Hole Velocities as a Function of Temperature from Wafer No. 51310.	84
38	I-V Curve from a Device with a Nominal Doping of $5 \times 10^{15}\text{cm}^{-3}$ .	86
39	Profile of Doping Density vs. Distance for Wafer No. 51165.	88
40	Electric Field vs. $x_{tot} - x_n + x_p$ for Wafers 32506, 33205, 91216, and 51165.	92
41	Current as a Function of Reverse Bias.	94
42	Plot of the Doping Profile of the Double-Drift Read Wafer No. 33205, which is Used for a Determination of the Ionization Coefficient.	95
43	Breakdown Electric Field.	97
44	Plot of the Electric Field vs. $x_{tot}$ .	99
45	Triangular and Rectangular Fields.	100

LIST OF ILLUSTRATIONS (Continued)

<u>FIGURE</u>	<u>TITLE</u>	<u>PAGE</u>
46	Plot of the Electric Field Producing an Electron Ionization Coefficient of $7.2 \times 10^4 \text{cm}^{-1}$ for Various Temperatures as Measured on Devices No. 3 and No. 6.	104
47	Curves of a vs. b for Specific Wafers, with $M = 2$ .	106
48	Curves of a vs. b for $M = 1$ .	107
49	Comparison of Ionization Coefficients from the Present Experiment with the Results of Earlier Investigators	109
50	Values of $\alpha$ and $\beta$ .	111

LIST OF TABLES

<u>TABLE</u>	<u>TITLE</u>	<u>PAGE</u>
1	Hydrogen Iodide Content of Various Tanks	19
2	Results of Growth Runs Using Helium As $I_2$ Transport Gas	24
3	Characteristics of $p^+-p-p^+$ Wafers	30
4	Growth Conditions of $p^+-p-p^+$ Wafers	32
5	Sequence of Steps Used to Grow P-Read Wafers	38
6	X-Band P-Read Wafers	43
7	Ka-Band P-Read Wafers	44
8	Characteristics of $p^+-p-p^+$ Velocity Measurement Samples	66
9	Area of Device	75
10	Parameters for Etched VMS 278	82
11	Temperature Dependence of Device 6 from Wafer No. 33205	103

## SECTION I INTRODUCTION

### 1.1 Objective

The overall objective of this exploratory development program was to provide improved techniques for epitaxially growing p-type gallium arsenide with the doping profiles needed for double-drift avalanche diodes in the 8 to 60 GHz frequency range. A concomitant and equally important effort was the quantitative measurement of two critical materials parameters - hole ionization coefficient and hole velocity - which must be accurately known for proper device design.

### 1.2 Goals

This program was confined to the epitaxial growth and characterization of p-type material. The fabrication of devices was specifically excluded to allow maximum opportunity for experimenting with p-type doping techniques. The epitaxial material was to be thoroughly characterized to determine its quality. Ionization coefficients and hole velocities were to be measured on selected samples. These measurements were to be carried out under conditions resembling (as closely as possible) actual device operating conditions; therefore the effects of temperature variation and high electric field were to be assessed.

This program was not expected to result in a highly perfected p-type materials technology. It was intended to provide a sound basis for further development of one or more doping techniques having the potential to meet the stringent specifications demanded by avalanche diodes. Therefore, doping techniques were to be evaluated in each of the following contexts:

- a) Carrier concentration, with precise control over the  $10^{15}$  to  $10^{19}$   $\text{cm}^{-3}$  range;
- b) Layer thickness, from a few hundred angstroms to 5 micrometers with a tolerance of  $\pm 10$  percent;
- c) Multilayer structures with step-doping changes;

- d) High quality p:n junctions;
- e) Surface quality, mirrorlike;
- f) Yield, 20 percent or more wafers meeting all parameters.

### 1.3 Tasks

#### 1.3.1 Task I: Epitaxial growth experiments

Task I of this program was intended to optimize growth procedures for p-type gallium arsenide epitaxy. At least two p-doping techniques were to be evaluated. The goal was to determine the strength and weakness of each technique and to decide which offered the greater potential for further development.

At the start of the program, Raytheon scientists had established the state of the art for p-type GaAs epitaxy as part of their continuing development of double-drift diodes. However, the reproducible growth of p-type epitaxial layers was still a limiting factor in the fabrication of double-drift diodes. This task was intended to help correct this deficiency.

Each epitaxial growth technique was to be evaluated in terms of the goals listed in Sec. 1.2 above.

#### 1.3.2 Task II: Physical Measurements

In order to design double-drift diodes properly, it is necessary to know the electron and hole drift velocities and the ionization coefficients of both p- and n-type material as a function of electric field and temperature. Although there is adequate information for n-type material, little data on p-type material appears in the literature. The objective of this program was to provide supplementary physical property data on p-type material. The effort was subdivided into two tasks: the first aimed at hole velocity measurements, the second, measurement of ionization coefficients.

### 1.3.3 Task III: Demonstration growth of p-Read structures

The third task was intended to test the growth techniques evaluated under this contract by making twenty growth runs aimed at producing p-type Read wafers, ten with X-band parameters, and ten with Ka-band parameters. The results of this set of experiments were to be tabulated and used as a guide for forming conclusions and offering recommendations for further development.

### 1.4 Summary

During the past several years, notable progress has been made in the absolute power-generating capability of GaAs IMPATT diodes. In the early years, the major advances were made in n-type single-drift diodes, first in flat profile devices (with efficiencies up to 17 percent), then in Read-profile devices (with efficiencies up to 35 percent). In principle, even higher powers and efficiencies appeared possible from double-drift GaAs devices but only scattered results were being obtained experimentally. When GaAs double-drift diodes were first demonstrated in the middle 70's it quickly became apparent that knowledge of both growth processes and hole transport properties in p-type GaAs were limiting more rapid development.

At the beginning of this program, the growth of n-type structures was under relatively good control, as was knowledge of their electron transport properties. The growth of p-type structures suitable for X-band operation was, however, quite erratic. The knowledge of hole transport properties was limited to the results published by a single worker, and his results did not explain the experimental performance of double-drift devices. This program was initiated to remedy these deficiencies.



## SECTION II

### EPITAXIAL GROWTH EXPERIMENTS

#### 2.1 Introduction

During the past several years, notable progress has been made in the dc-to-rf conversion efficiencies and absolute power generation capability of GaAs IMPATT diodes (Adlerstein et al., 1975; Adlerstein et al., 1978; Hierl et al., 1977). Beginning in early 1973, n-type GaAs IMPATT diodes displayed a quantum jump in performance (Kim et al., 1973). The impetus for this advance in the state of the art was the development of technology which permitted the growth of controlled n-type GaAs structures (Steele et al., 1975). In principle, even higher powers and efficiencies are possible from GaAs double-drift IMPATT diodes (Kuvass, 1976). Encouraging results have been reported; however, at the lower frequencies the major improvement has been in power rather than efficiency (Wallace et al., 1977). Until recently, experimental difficulties in the growth of higher quality p-type GaAs inhibited more rapid progress (Goldwasser et al., 1975). A major goal of this program was to improve the technology for the growth of p-type structures so that it more nearly approaches that of the n-type structures.

The experimental work was carried out in an  $\text{AsCl}_3$  open tube VPE reactor because this system is the one most commonly used to produce IMPATT wafers. With suitable modifications the technology developed here can be adapted to other vapor epitaxial systems.

#### 2.2 p-Doping Techniques

##### 2.2.1 Introduction

In order to achieve epitaxial layers of closely controlled carrier concentration in the  $\text{AsCl}_3$  open tube VPE reactor, it is necessary to introduce a precise amount of a volatile dopant into the reactor vapor stream in the vicinity of the substrate. Elements which have been used as p-type dopants in GaAs include cadmium, zinc, beryllium, magnesium, manganese and, under gallium-rich conditions, germanium. Several p-doping techniques using these materials have been tried in our laboratory and others.

In this section, we will discuss the general techniques used by the industry, prior to this contractual effort, to effect p-type doping in GaAs. In the course of this discussion some of the limitations of these processes will become apparent. We will then briefly describe some of the specific p-doping techniques which have been experimentally evaluated in our own laboratory. The more promising will be discussed in greater detail later in this report.

### 2.2.2 Direct vaporization

A technique which we have chosen not to utilize (but which has been used with varying success by many other laboratories) is direct vaporization. In this technique, substances such as cadmium or zinc metal are used as dopants by heating them so that transport into the reactor can be effected with a carrier gas.

In the most common arrangement, a small amount of the metal is placed in a heated side arm with a metered flow of hydrogen or some other carrier gas passing over it to carry the vapors into the reactor (Ettenberg and Neuse, 1975). Precautions must be taken to ensure that all parts of the vapor path between the metal and the substrate are held at a temperature above that of the dopant source; otherwise condensation occurs, and the doping is unpredictable.

The actual acceptor concentration in the epitaxial layer, whether using this method or others, depends upon the doping efficiency, defined as that fraction of the dopant atoms available in the vapor stream which incorporate into the growing epitaxial layer. Ideally, the doping efficiency is independent of widely varying dopant concentrations in the vapor stream. If this is true, the hole concentration can be readily controlled by varying the temperature of the doping material or by varying the flow of carrier gas. This method has been found to be practical by various workers, although an objective evaluation is difficult because of the paucity of detail reported in the literature.

The principal limitation of the direct vaporization technique is its inherently slow response which makes rapid doping level changes difficult. One method used to initiate or halt p-doping is to hold the solid dopant material in the cold region of a side arm to the reactor when no p-doping is required.

The dopant holder is arranged to be movable, and the side arm in which it moves is provided with a large temperature gradient. P-type doping is initiated by positioning the dopant in a predetermined hot zone where its vapor pressure is appropriate for transport into the reactor. Changes in doping level are made by moving the dopant to a different temperature zone or by changing the carrier gas flow. Alternately, the dopant is placed in a vaporizer held at a constant temperature, with the dopant transport regulated by the flow of a carrier gas. In each arrangement, the vapor path between the dopant and the substrate must be kept at a temperature above that at which dopant condensation occurs. Some difficulties of achieving dopant transport by vaporization are: the strong dependence on dopant temperature, the possibility of dopant condensation en route to the substrate, and the fact that doping cannot be readily initiated, terminated, or controlled by room-temperature gas-control equipment.

#### 2.2.3 Doped source

One technique which was used in the early days of GaAs epitaxy for n-type doping was to provide a source, either gallium or gallium arsenide, doped to a specific level with tin (Wolfe et al., 1968). The source material is transported as the chloride by passing the reaction products of  $\text{AsCl}_3$  and  $\text{H}_2$  over it. Since the transport rate of tin is fortuitously about the same as that of gallium, this system works very well. The similar use of zinc or other p-type dopants has not been useful because their transport rate is quite different from that of gallium and as a consequence doping control is poor.

#### 2.2.4 Zinc alkyls

One early approach to the p-doping of GaAs was to use a constant temperature vaporizer loaded with dimethyl or diethyl zinc (Conrad and Haisty, 1966). A metered flow of inactive carrier gas was passed over or through the metal organic compound to transport it into the reactor. Reproducible results were claimed at hole concentrations suitable for optoelectronic devices.

We have similarly used prepared mixtures of dimethyl or diethyl zinc diluted to 50 to 500 ppm with hydrogen (Steele et al., 1979). Dimethyl zinc diluted with hydrogen appears to be somewhat more stable in the gas cylinder than does diethyl zinc but otherwise we have seen little difference between the two compounds.

Doping was accomplished by metering a small flow of the doping mixture into the reactor through a fused silica doping tube terminating between source and substrate. Equipment and procedures similar to those described later in this report were used. Epitaxial layers with hole concentrations greater than  $10^{19}\text{cm}^{-3}$  were readily achieved, even in  $p^{++}$  contact layers only a few tenths of a micrometer in thickness. In growing these highly doped contact layers, we found it desirable to maintain the zinc alkyl flow for approximately two minutes after terminating growth and beginning wafer cooling. If this was not done the surface was invariably lower doped than the interior of the layer.

We were able to grow p-type layers reproducibly with hole concentrations greater than  $5 \times 10^{16}\text{cm}^{-3}$  using this technique. Low doped layers have been grown with hole concentrations between  $5 \times 10^{14}\text{cm}^{-3}$  and  $5 \times 10^{16}\text{cm}^{-3}$  using dilute  $\text{Me}_2\text{Zn}$  as a dopant. We found, however, that the net hole concentration was poorly controlled at the lower doping levels.

#### 2.2.5 Zinc iodide doping

Some of the difficulties mentioned in the previous sections may be overcome by using zinc iodide vapor, generated as needed, for the p-type dopant (Silvestri and Fang, 1964). Most of the p-type doping experiments carried out under this contract used this approach. Two distinct techniques were explored during the course of this work. The first used hydrogen iodide as the transporting reagent, the second used iodine. These two methods are described in some detail in later sections.

## 2.3 Epitaxial Growth System

### 2.3.1 Introduction

All of the epitaxial growth experiments on this program were carried out in an open tube  $\text{AsCl}_3\text{-H}_2\text{-Ga}$  vapor-phase epitaxy system, using silicon as the donor impurity and zinc as the acceptor impurity. A schematic diagram of the system is shown in Fig. 1. A movable furnace with six independently controlled temperature zones allows us to maintain an accurate and reproducible temperature profile inside the reactor. Typically, the gallium source is maintained at  $820^\circ\text{C}$  while the temperature at the substrate is held at  $750^\circ\text{C}$ . A linear temperature gradient is maintained between source and substrate. The furnace is aligned on two tracks which permits it to be rolled back from the growth position at the end of each run. In the rolled-back (standby) position, the furnace assists with the bakeout of the heated line. The bakeout procedure is described in a later section.

### 2.3.2 Microprocessor control

During the final quarter of the contract period, the VPE reactor dedicated to this project was put under microprocessor control. A software package developed in-house allows the computer to store up to 80 program steps in up to four program locations in its memory. Thus, several growth sequences may be preprogrammed into the computer and called as needed. During each program step, the computer adjusts gas flows to programmed levels via the flow controllers, actuates selected solenoids in the doping networks via a switch bank, and accurately keeps track of elapsed step time. At the present time, switch status and flow data are automatically recorded during each program step. Provision is currently being made to place temperature control and data taking under computer control as well. A schematic diagram of the interaction between computer and reactor is shown in Fig. 2.

Microprocessor control of the VPE reactor offers several advantages over manual control. In general, electronic switching is more reliable than mechanical switching (prior to installation of the microprocessor, the solenoid switches

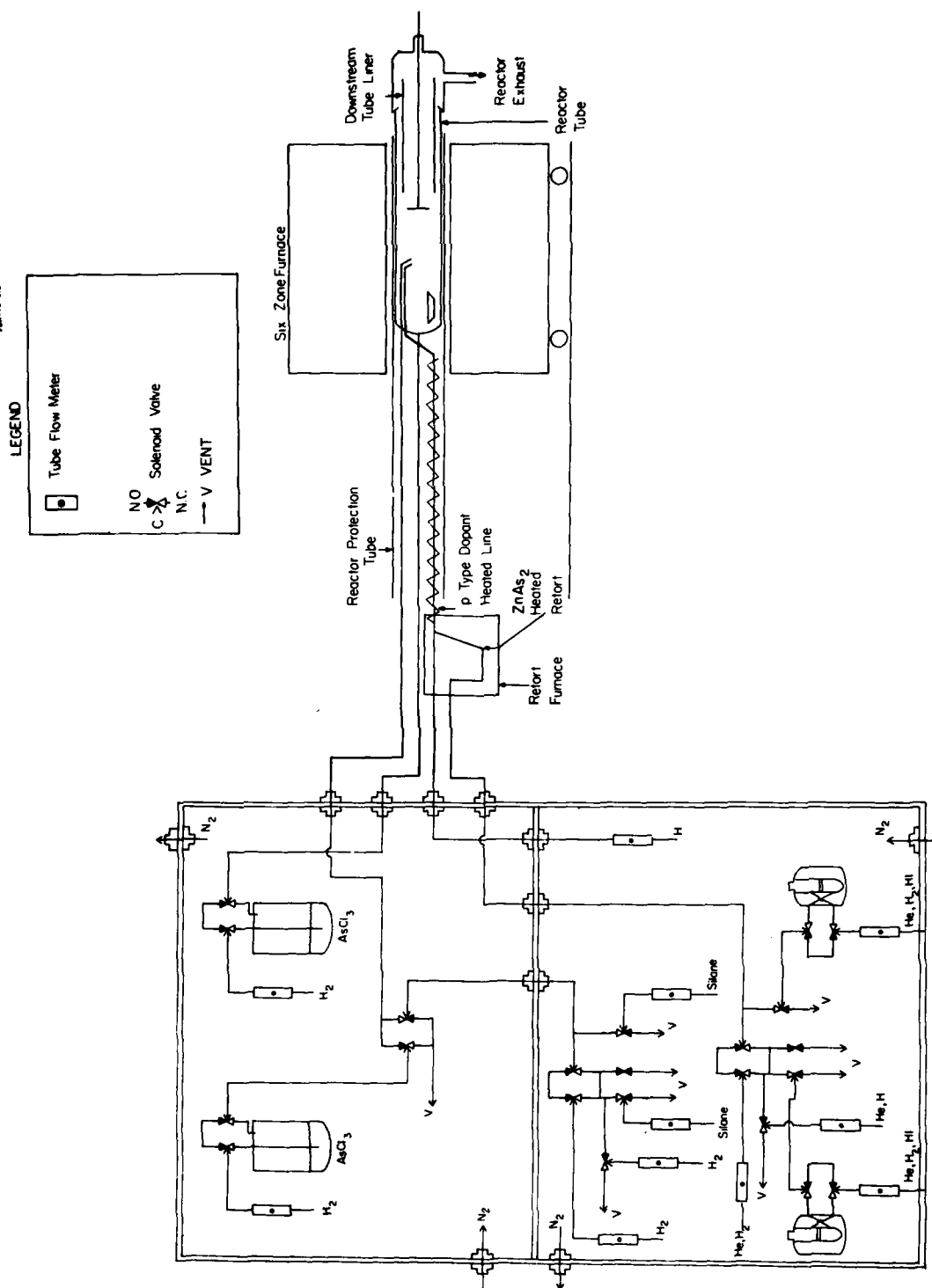


Figure 1. Schematic Diagram of VPE System, Showing Doping Networks and Reactor Geometry.

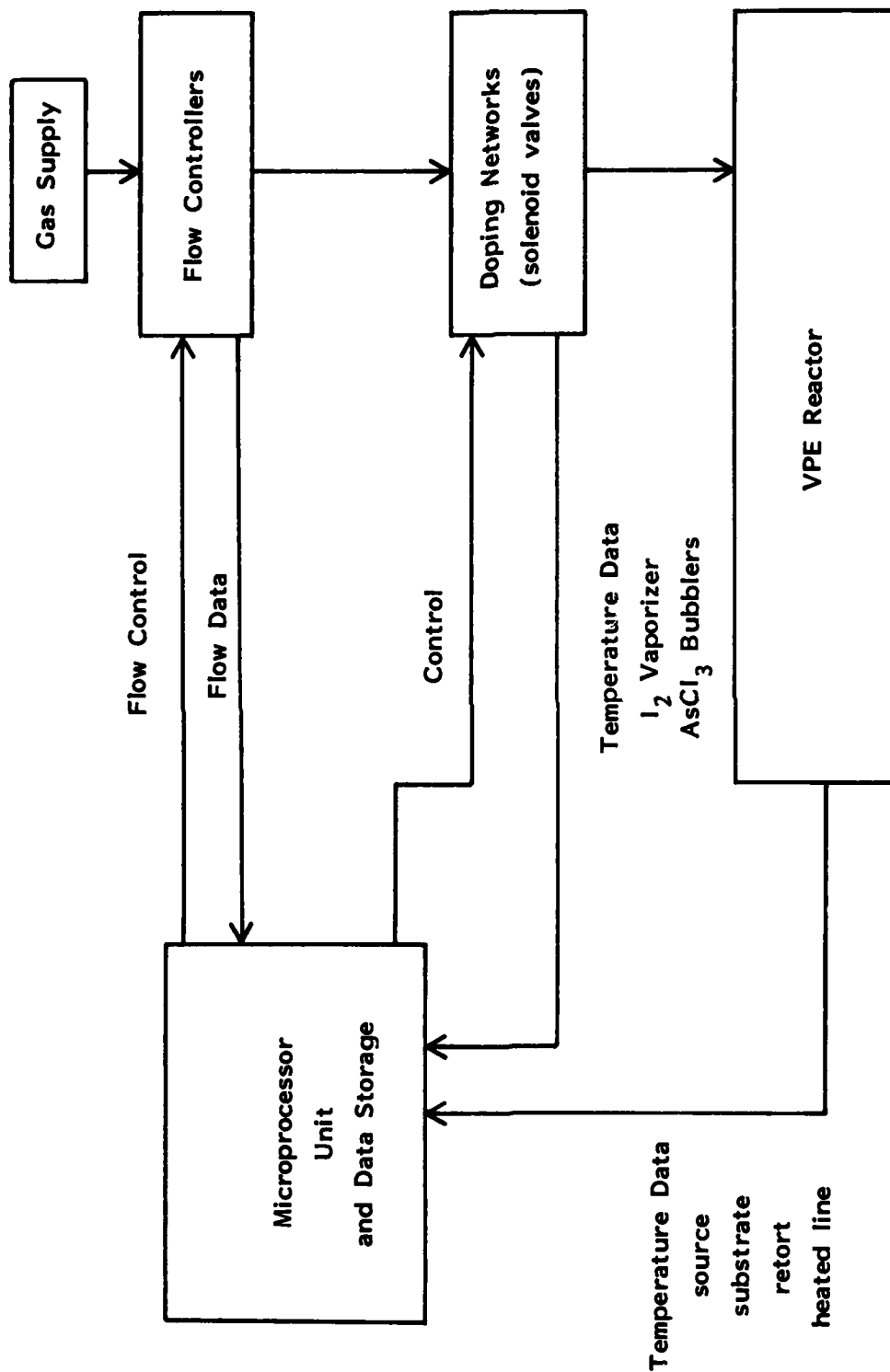


Figure 2. Block Diagram of Microprocessor - VPE System Interaction.

were actuated by a cam connected to a series of mechanical clocks). Program steps can be timed more accurately with the microprocessor. Finally, data accumulation and retrieval become more reliable and orders of magnitude faster with the computer. In general, the entire system is far less operator-dependent.

### 2.3.3 Gas-handling system

Although not shown in Fig. 1, each of the gas inlet lines contains a mass flow controller calibrated for hydrogen gas. Pure hydrogen is obtained by passing commercially obtained  $H_2$  through a palladium diffuser. In cases where helium is used instead of hydrogen (as in the p doping network described below), the flow controllers are circumvented and needle valves are used to regulate flows. As a secondary check on gas flows, each line also includes a rotometer. The flow meters, as well as all components of the doping networks, are housed in glove boxes which are continually flushed with nitrogen. Thus any leaks which arise admit nitrogen rather than oxygen into the reactor. At any time, by actuating a single switch, the entire system can be purged with either hydrogen, helium, or nitrogen. This feature not only allows flexibility in the doping technique used, but also provides an additional safety measure. All components of the gas handling system are constructed of relatively inert materials (pyrex, silica, teflon, or stainless steel) to reduce the risks of contamination and/or corrosion.

Two arsenic trichloride bubblers are included in the system, one to supply  $AsCl_3$  to the source via the grow line and the other which can supply  $AsCl_3$  directly to the substrate via the etch line. Each bubbler is jacketed and provided with its own constant temperature circulator so that the concentrations of  $AsCl_3$  in the individual gas streams may be separately controlled. Associated with each bubbler are pairs of three-way teflon solenoid valves which are actuated together to divert the stream of hydrogen gas either through the bubbler or directly into the reactor.

### 2.3.4 Doping networks

Both the p-type and the n-type doping networks are built around similar



designs. Each provides for two separate sources of doping gas, one of high concentration and one of low concentration. The high concentration line contains a reservoir which allows a fixed volume of gas of any desired concentration (up to the concentration of the source gas) to be injected into the reactor in the form of a quasi-discrete charge. This technique is used to produce doping spikes such as are required in the growth of Read profile devices. Provision is made for each gas stream which enters a doping network to be vented through its own exhaust bubbler when not diverted into the reactor. Thus a steady-state gas flow may be established (and thus an equilibrium dopant concentration) before the doping gas enters the reactor. In addition, the vent bubblers provide a useful check on both doping flows and flow rates.

Silicon is used to provide donor impurities in the epitaxial layer. Silicon is obtained in the form of silane ( $\text{SiH}_4$ ) gas diluted with hydrogen which is purchased from commercial vendors. Zinc is used for p-type doping. As discussed in Sec. 2.2, several methods exist for transporting zinc into the reactor. If dimethyl zinc or hydrogen iodide is used, then there is no difference between the p- and n-doping networks. Dimethyl zinc is obtained in the form of a prepared gas mixture from a commercial vendor as is the hydrogen iodide used for reactive transport.

#### 2.3.5 p-doping by reactive transport

The method of transporting zinc principally used on this contract was to form a volatile compound by reaction between solid zinc (in the form of either pure zinc or a solid zinc compound) and a gas, and then to transport the vapor into the reactor with a carrier gas. We have successfully used zinc arsenide ( $\text{ZnAs}_2$ ) heated in a retort to between  $200^\circ\text{C}$  and  $425^\circ\text{C}$  and hydrogen iodide or iodine vapor to form zinc iodide which is carried into the reactor by either hydrogen or helium.

Both HI and  $\text{I}_2$  are used routinely in our laboratory as reactants in the  $\text{ZnI}_2$  doping process. HI is obtained in the form of a gas from a commercial vendor and is brought into the p-doping network in the same manner as each of

the other gases we use. For reasons which are discussed in Sec. 2.4, we have chosen to use  $I_2$  exclusively in the growth of p-Read wafers. This dopant required an additional apparatus, which is described below.

The iodine vapor is generated in a vaporizer, a drawing of which is shown in Fig. 3. The flow of carrier gas (either He or  $H_2$ ) normally bypasses the vaporizer, but may be directed into the vaporizer by means of two coupled solenoid valves (in the same manner in which gas flow is directed into the  $AsCl_3$  bubblers). The vaporizer is maintained at a constant temperature by circulating temperature stabilized water or water-methanol mixture through a surrounding jacket. The unit is designed so that the entering He, the iodine, and the He +  $I_2$  that leaves the unit are all cooled in the jacket. This allows the helium to become saturated, but not supersaturated, with iodine at any temperature. The helium passes through a layer of iodine crystals about 1.2 square inches in area and 1/4 inch thick so that the output gas stream is equilibrated with the vapor. The flow of carrier gas through the vaporizer was usually between 2 and 10 sccm in our experiments. Two identical vaporizers are used in our p-doping network. One is usually maintained at 16°C and one at -5 to -20°C so that doping sources of high and low concentration are available, just as in the n-network. When HI is used, two cylinders filled with mixtures of high and low concentrations are provided.

We have retained complete flexibility with our VPE reactor in the choice of p-doping technique available to us. The gas inlet lines to the p-doping network may be supplied with either HI (or  $Me_2Zn$ ) from tanks or with high-purity  $H_2$  or He. In the latter case, the iodine vaporizers are used to generate  $I_2$ . When HI is used, the vaporizers are simply bypassed.

In order to generate zinc iodide, the HI or  $I_2$  vapor must be reacted with  $ZnAs_2$  crystals. This reaction occurs at elevated temperature inside a heated retort. A diagram of the retort, its surrounding furnace, and the heated line which carries the reaction products into the reactor is shown in Fig. 4. The entire length of the heated line is maintained at a temperature above that of the retort in order to avoid condensation of the zinc iodide before it enters

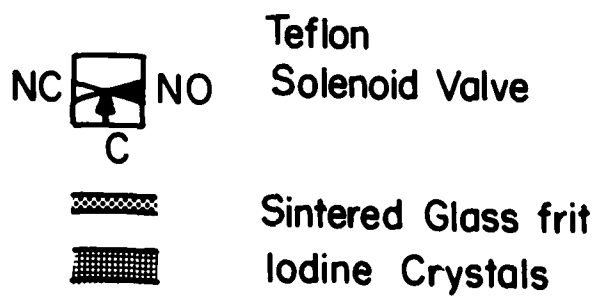
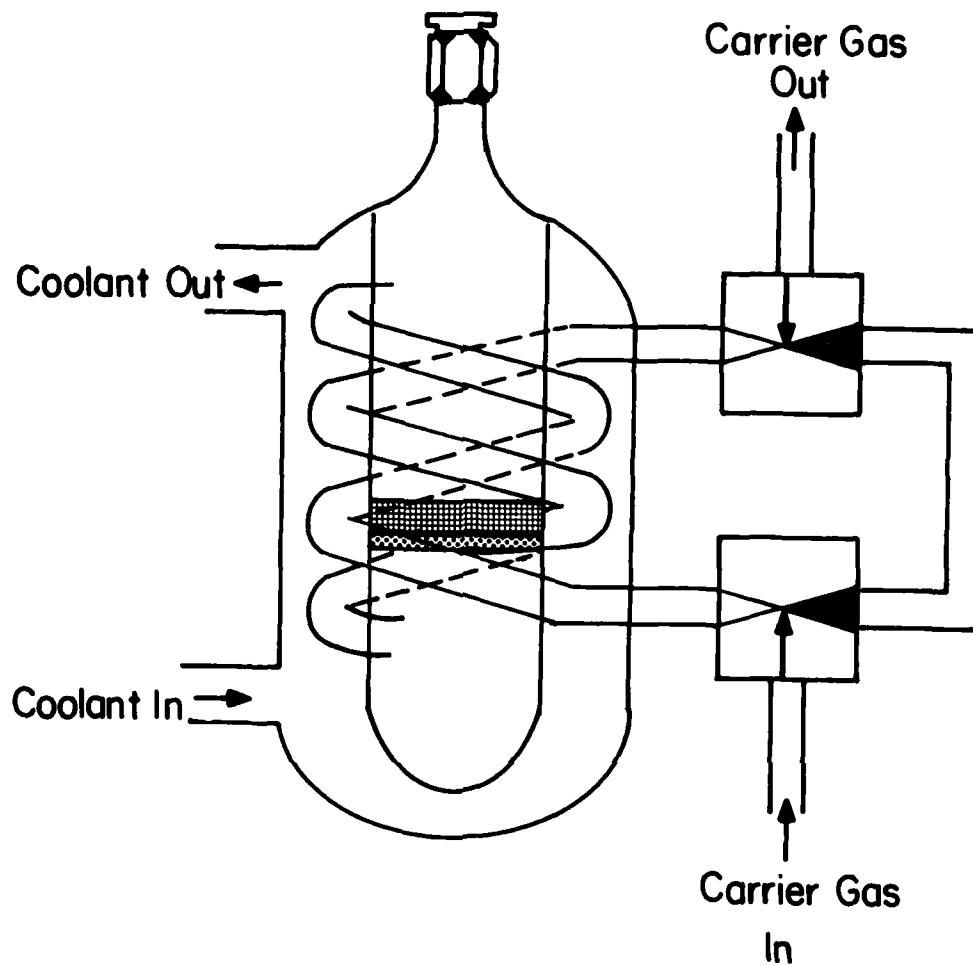


Figure 3. Diagram of Iodine Vaporizer.

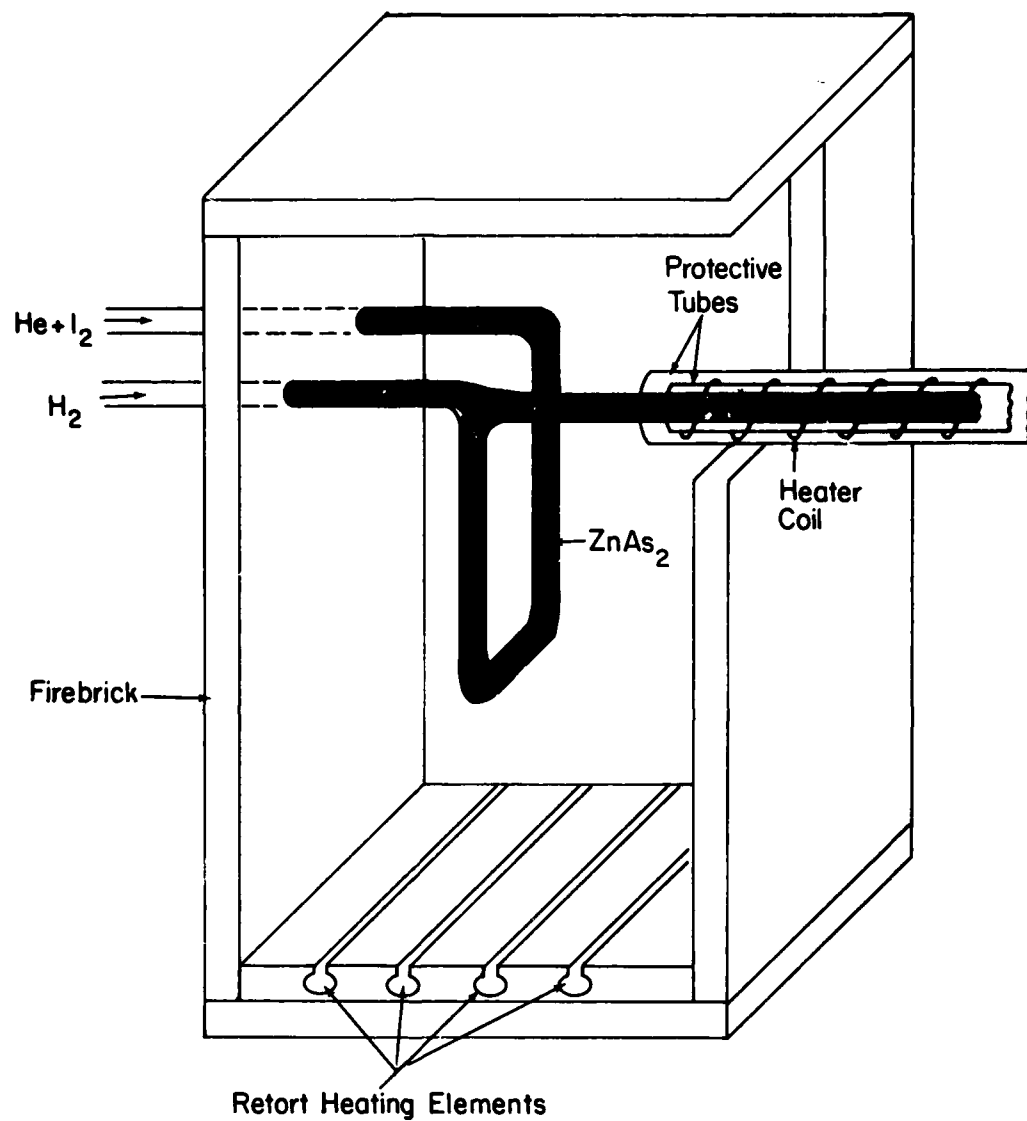


Figure 4. Diagram of Retort and Heated Line. Arrows indicate directions of p-doping and retort bypass gas flows.

the reactor. A bypass line is provided and continuously flushed with  $H_2$  to purge the line when no zinc iodide is being generated.

#### 2.4 Reactive Transport Experiments

The growth experiments made in connection with this contract have emphasized optimization of  $ZnI_2$  reactive transport doping. This doping technique generates a volatile compound,  $ZnI_2$ , by reaction between solid zinc arsenide and a reactive gas, either HI or  $I_2$ . The reaction occurs in a temperature controlled retort, just described, at temperatures ranging between 200 to 450°C. The  $ZnI_2$  vapor is then transported into the reactor with a carrier gas, usually helium, via a heated line.

Zinc arsenide is used as the solid reactant because of its low vapor pressure. Figure 5 plots the partial pressure of zinc over zinc arsenide, zinc, and zinc iodide as a function of temperature. (Munir, et al., 1974; Schoonmaker and Lemmerman, 1972; Handbook of Chemistry and Physics.) The vapor pressure of zinc iodide is three orders of magnitude greater than that of zinc arsenide. The partial pressure of zinc over zinc arsenide at our standard retort temperatures is relatively low so that little zinc enters the reactor vapor stream when helium alone is passed over the zinc arsenide. However, volatile zinc iodide is formed when dilute hydrogen iodide or iodine is passed over the zinc arsenide under the same conditions. The reaction is such that the amount of volatile  $ZnI_2$  formed is proportional to the amount of HI or  $I_2$  introduced into the retort. Therefore, by controlling the flow of the reactive gas into the retort, we can effectively control the introduction of zinc iodide into the reactor and in turn, the epitaxial hole concentration.

The percentage of HI or  $I_2$  that reacts with zinc arsenide to form  $ZnI_2$  has not been determined. Therefore, we are unable to calculate the  $ZnI_2$  concentration in the reactor during growth. Instead, we calculate the HI or  $I_2$  concentration for the run as if the HI or  $I_2$  is simply diluted with the total flow in the reactor. The doping efficiency of HI or  $I_2$  is really a function of the percentage that reacts in the retort to form  $ZnI_2$ , combined with the actual efficiency of Zn incorporation at the substrate surface.

#### 2.4.1 HI reactive transport

Under company funding we have previously demonstrated reproducible p-type doping between  $5 \times 10^{15}$  and  $1 \times 10^{18} \text{ cm}^{-3}$  using HI reactive transport. In fact, this system has been used to produce p-type layers for EHF double-drift IMPATT diodes for another AFAL contract (F33615-77-C-1186).

We use hydrogen iodide diluted in hydrogen obtained from various commercial vendors. HI concentrations quoted for run conditions are based on the vendors' analysis. We have purchased HI from several vendors and all have difficulty in providing HI concentrations to our specification. On several occasions we have tried two cylinders obtained from the same vendor with the same nominal HI concentration and obtained very different doping efficiencies. With this uncertainty in concentration, we had several cylinders of HI sampled and measured for iodide content by an independent laboratory. The results are shown in Table 1. Unfortunately, each tank analyzed at  $\sim 100$  ppm although the nominal concentration differed widely, and the validity of this measurement is also in question.

Lacking a certain means of prequalifying HI tanks for iodine concentration, we are reduced to the time-consuming procedure of placing new tanks on line to grow a p-layer with nominal reactor settings, measuring the hole concentration of the resulting epitaxy, and adjusting HI flow and retort temperature to achieve the requisite p-doping level. If, after making several runs on a tank, we cannot obtain controlled p-doping, the tank is discarded and another one put on line. This often turns into a very time-consuming task.

The amount of p-doping introduced into the system can be varied either by varying the gas flow or by varying the HI concentration in the original mixture. Depending on the range of doping desired, we use cylinders of HI at concentrations of 100 ppm or 10,000 ppm in hydrogen. Two cylinders are used in a single run when a multilayer structure, requiring a wide range of doping, is grown.

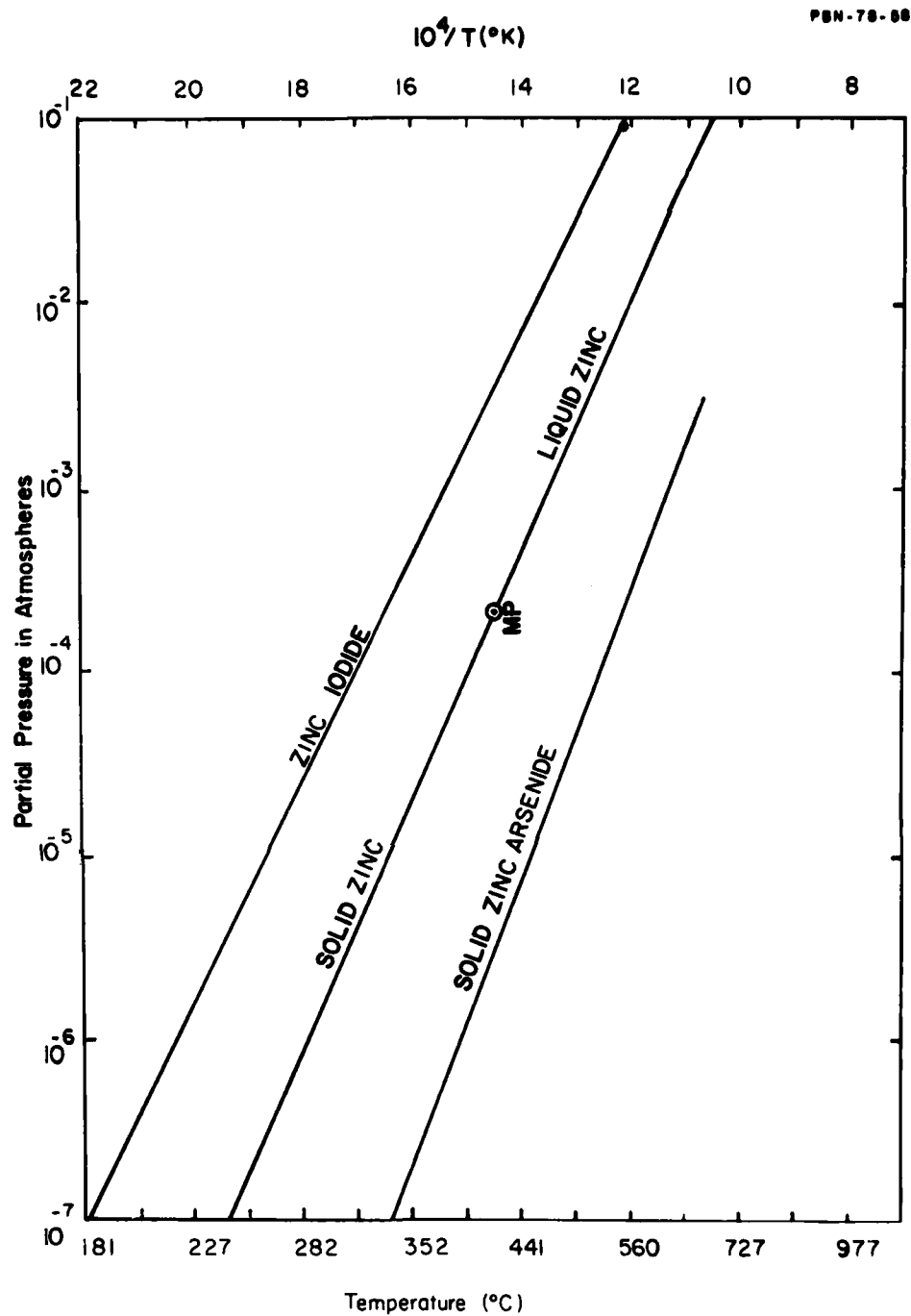


Figure 5. Partial Pressures of Zn over Zinc Arsenide, Zinc, and Zinc Iodide as a Function of Temperature.

**TABLE 1**  
**HYDROGEN IODIDE CONTENT OF VARIOUS TANKS**

	<u>Tank No.</u>	<u>Vendor's Analysis (ppm)</u>	<u>Mass Spectrographic Analysis* (ppm)</u>
Vendor #1	71128	11,000	93
Vendor #2	1A010513	98	100
	1A010125	955	100
Vendor #3	H68718	995	87
	71117	98	107
Vendor #4	1186	98	86
	7235	98	93
	417	995	121
	7047	995	114

\* *By an independent laboratory.*



Control of acceptor incorporation can also be achieved by varying the retort temperature. We have found that the doping obtained using a given HI concentration is exponentially dependent on the reciprocal of the absolute temperature of the zinc arsenide (Fig. 6). In general, we set the retort temperature to a value compatible with the desired doping range, usually between 300 and 425°C, and adjust the HI flow through the retort to produce the prescribed doping level.

Hydrogen iodide is introduced into a helium flushed doping network via solenoid valves, and directed into the retort. The gas mixture flowing through the retort is comprised of hydrogen iodide, hydrogen, and helium. Our experience is that when hydrogen is used in place of helium as the carrier gas, higher acceptor incorporation results, presumably due to a more efficient reaction between the HI and zinc arsenide.

This doping method was used to grow the  $p^{++}$ - $p$ - $p^{++}$  sandwich structures which will be described in Sec. 2.6.

#### 2.4.2 I<sub>2</sub> reactive transport

Most of our doping experiments during the first half of the contract period were designed to investigate the iodine reactive transport doping method and evaluate it as an alternative to HI reactive transport.

The major difference between the HI and I<sub>2</sub> reactive transport systems is the nature of the reactive gas source. The difficulty in obtaining HI cylinders with known concentrations has already been discussed. With control of the I<sub>2</sub> vaporizer temperature (and therefore the I<sub>2</sub> vapor pressure), the concentration of I<sub>2</sub> in the carrier gas passing through the retort is known.

In one of our first runs, we grew two p-type layers, one using HI and the other using I<sub>2</sub>. The results are listed here for comparison:

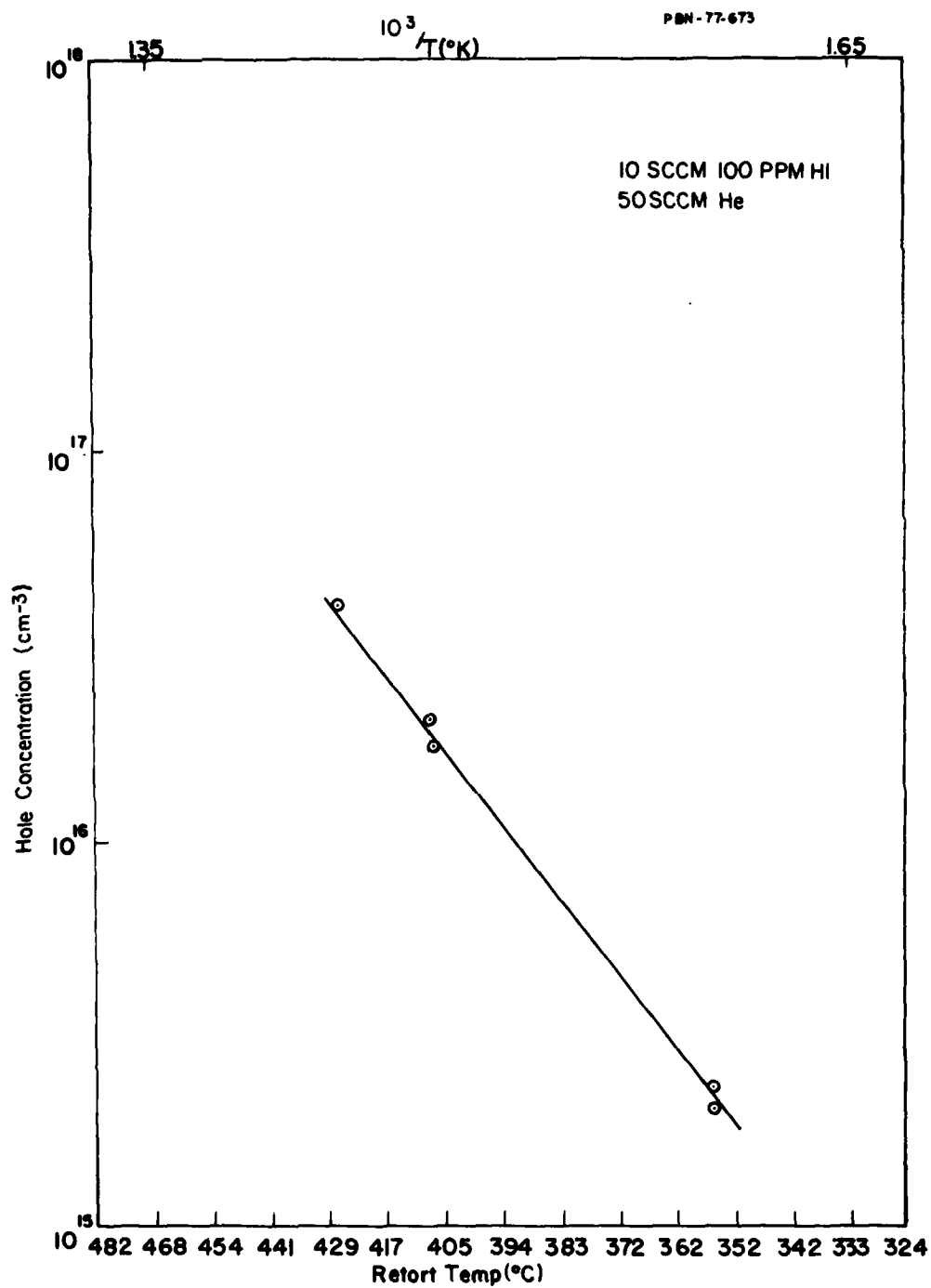


Figure 6. Hole Concentrations Obtained at Various Zinc Arsenide Temperatures with a Constant HI and Dilute Gas Flow.

Concentration (ppm)	Reactive Gas	Hole Concentration ( $\text{cm}^{-3}$ )	Doping Efficiency ( $\text{cm}^{-3}$ per ppm of iodine)
1.87*	HI	$6 \times 10^{16}$	$3.2 \times 10^{16}$
0.66	I <sub>2</sub>	$7 \times 10^{17}$	$1.06 \times 10^{18}$

Doping efficiency is calculated by dividing the resulting hole concentration by the impurity concentration, in this case HI or I<sub>2</sub>. The higher doping efficiency of I<sub>2</sub> is far greater than would be expected due to the two iodine atoms present in I<sub>2</sub> compared to the one atom in HI.

Figure 7 shows the doping results from many growth runs. Each run was made at a fixed vaporizer and retort temperature using helium to flush the p-network. Most of these runs incorporated several different doping levels obtained by varying the flow of carrier gas, either hydrogen or helium, through the vaporizer. There is a roughly linear dependence of hole concentration on I<sub>2</sub> concentration. Careful examination of the figure will make apparent several trends. Helium substituted for hydrogen as the carrier gas through the vaporizer seems to lower the doping level when other conditions are kept the same. Lower retort temperatures also produce lower doping, but the change is not as dramatic as in the HI system. The small effect of retort temperature on doping was unexpected and warranted further investigation.

Using helium as the I<sub>2</sub> transport gas, we grew p-type material on n<sup>++</sup> substrates with 0.14 ppm I<sub>2</sub> at various retort temperatures. Table 2 shows the results of these experiments. Clearly, retort temperatures below 200°C are not useful in producing p-type material.

These experiments were made without pre-conditioning the retort with HI before initiating growth. Also, the p-type growth was followed by an unintentionally doped layer. This was grown by simply turning off the I<sub>2</sub> while

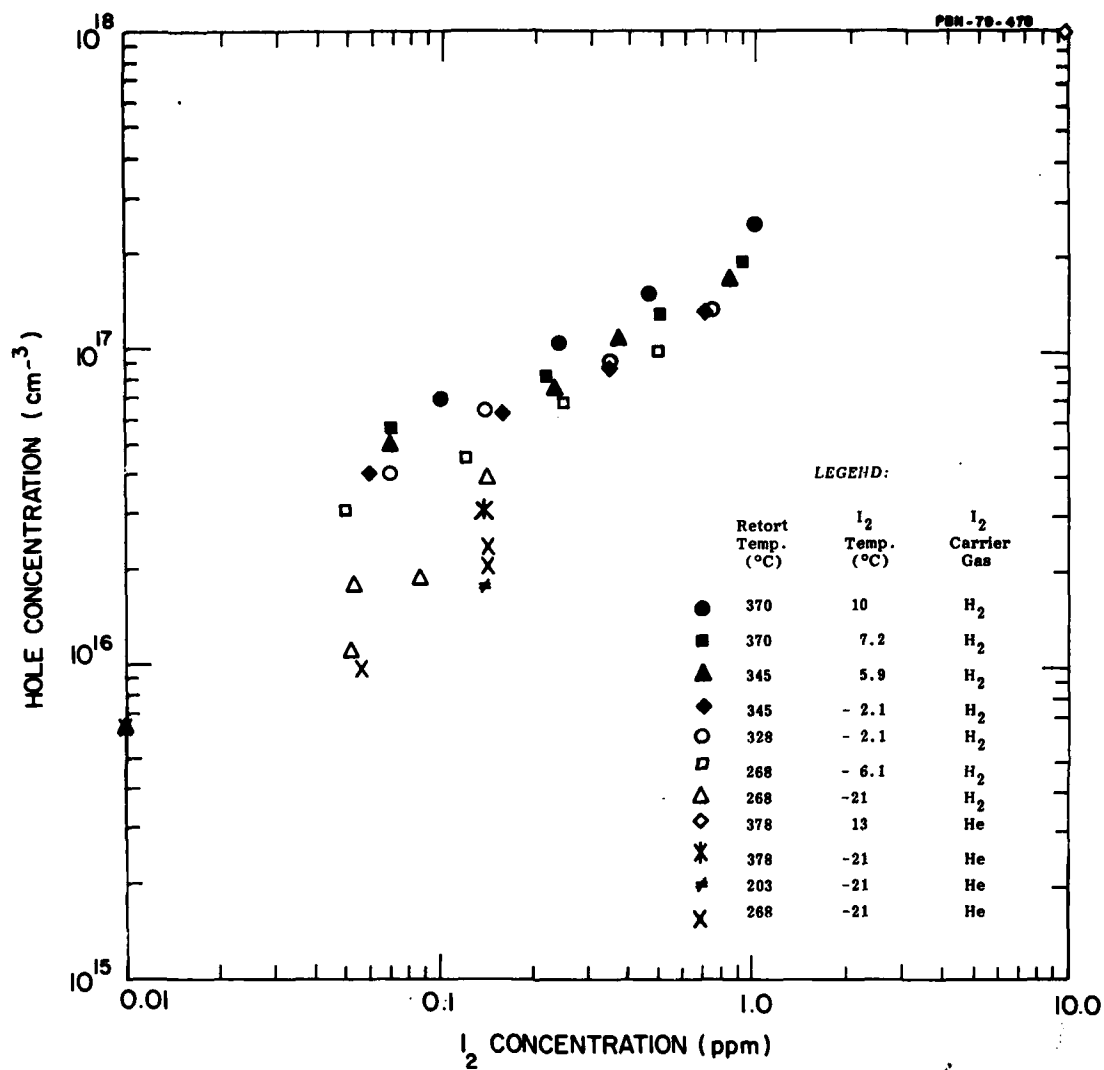


**Figure 7.** Hole Concentrations Experimentally Obtained as a Function of Iodine Concentration with Various Retort and  $\text{I}_2$  Vaporizer Temperatures and Hydrogen or Helium as the  $\text{I}_2$  Carrier Gas.

growth continued. The doping profiles of these runs are evidence of how fast the p-type doping turns on and off at various retort temperatures. Figure 8 shows the Schottky profiles for the three runs that produced p-type doping. As the retort temperature is increased, doping turn-on is faster but turn-off is slower.

TABLE 2  
RESULTS OF GROWTH RUNS USING HELIUM AS I<sub>2</sub> TRANSPORT GAS

<u>Run No.</u>	<u>Retort Temp. (°C)</u>	<u>I<sub>2</sub> Concentration (ppm)</u>	<u>Carrier Concentration (cm<sup>-3</sup>)</u>	<u>Type</u>
51332	378	0.14	$3.0 \times 10^{16}$	P
51328	263	0.14	$2.4 \times 10^{16}$	P
51329	203	0.14	$1.5 \times 10^{16}$	P
51331	180	0.14	(10-13 pf)	?
51330	152	0.14	$7.0 \times 10^{14}$	N

To establish doping uniformity using this doping technique, we grew a ten-micron-thick layer using a constant flow of I<sub>2</sub> vapor into the retort. Figure 9 shows the doping profile of this wafer based on C-V measurements taken on a step-etched sample. The doping is very uniform, except very close to the n<sup>++</sup> substrate where the hole concentration falls off slightly. Figure 10 shows a map of surface capacitance for the same wafer. The excellent uniformity across the surface is typical of our reactors.

#### 2.4.3 Comparison of HI and I<sub>2</sub> reactive transport doping methods

Based on the experiments made during this contract with the I<sub>2</sub> reactive transport system and our past experience with the similar HI system, we find the I<sub>2</sub> system has many distinct advantages.

Perhaps the most desirable feature of the I<sub>2</sub> system is that the need to rely on outside vendors for a very uncertain supply of HI is eliminated. Not only are the time consuming HI cylinder qualification runs eliminated, but runs made this year will be comparable to runs made next year.

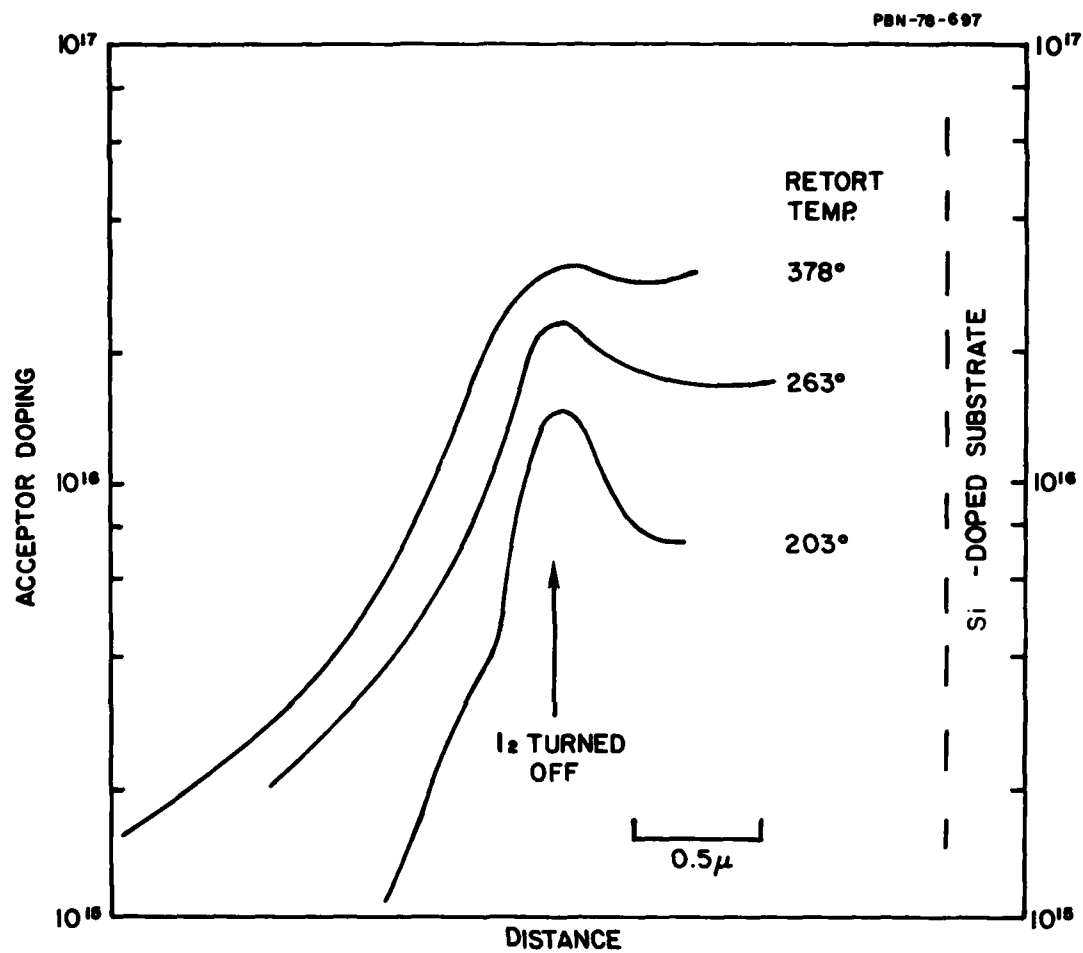


Figure 8 P-Doping Profiles on Silicon-Doped Substrates Produced at Various Retort Temperatures using 0.14 ppm  $I_2$ .

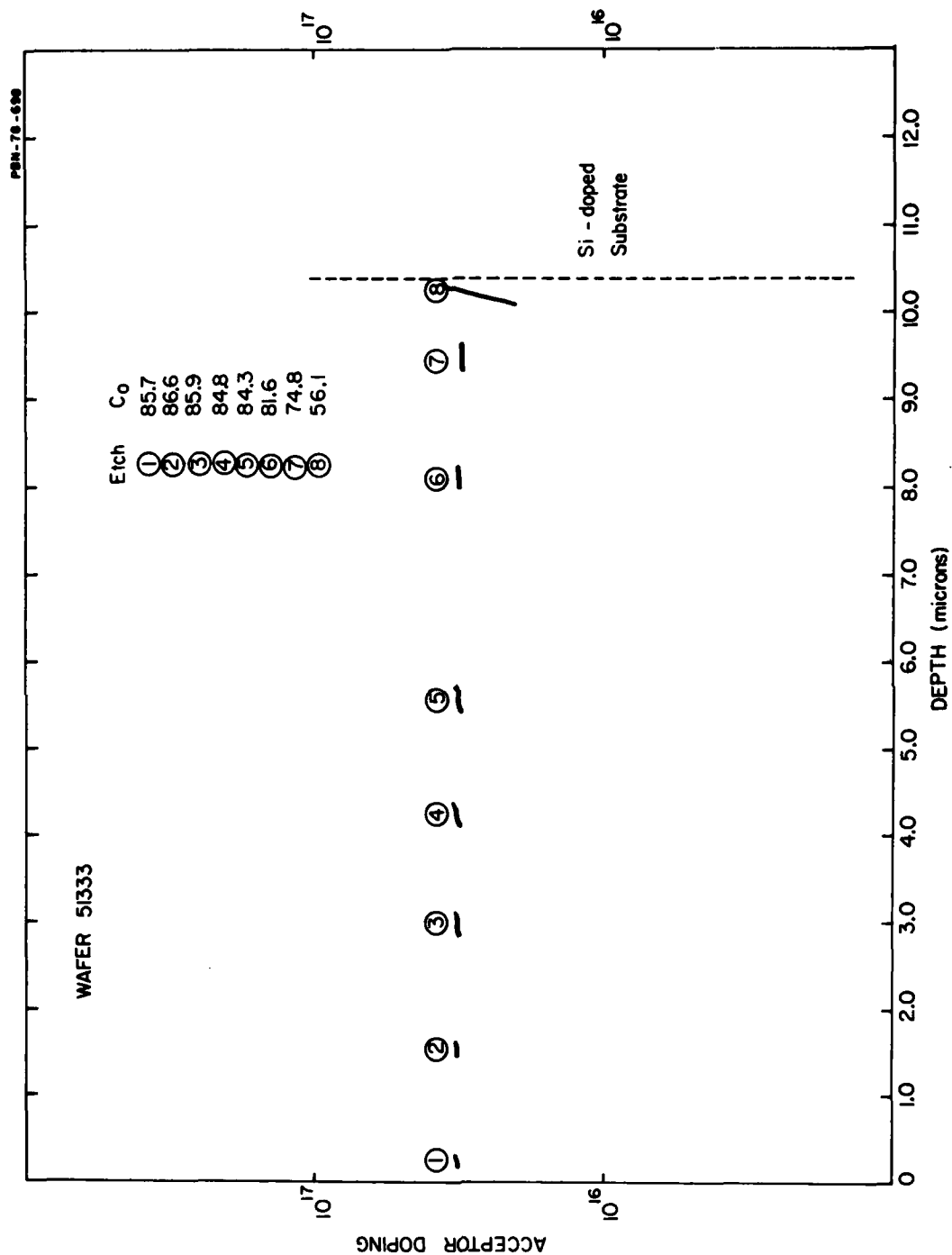


Figure 9 Doping Profile of Wafer 51333.

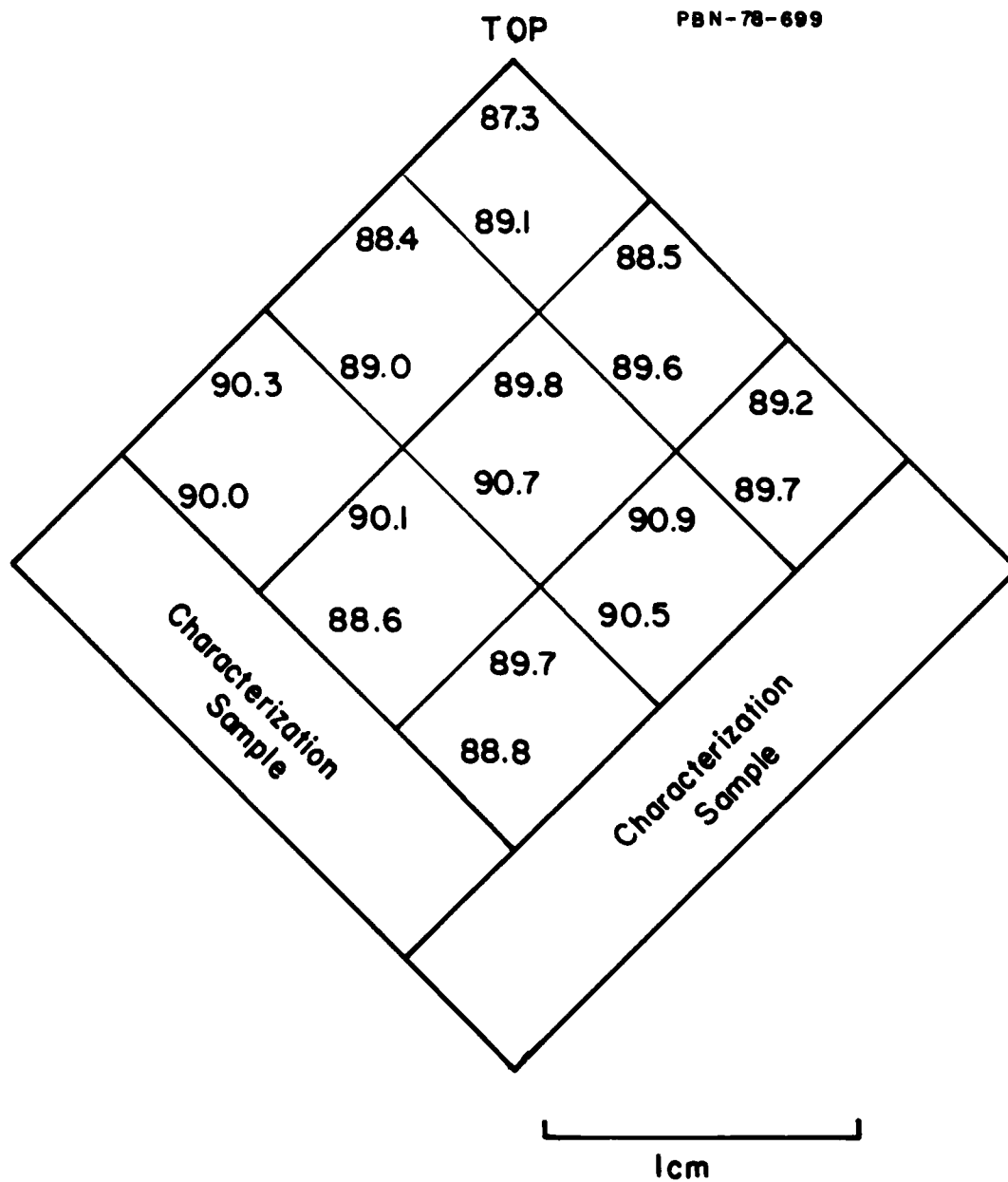


Figure 10 Map of Surface Capacitance of Wafer 51333.



Because the doping efficiency in the  $I_2$  system is less sensitive to the retort temperature than when HI is used, less precise control over retort temperature is required. This makes for better doping reproducibility from day to day.

Control over reactive gas concentration is also more flexible in the  $I_2$  system. Either the  $I_2$  vaporizer temperature or the flow of carrier gas or both can be controlled to effect changes in  $I_2$  concentration and the resultant p-doping level.

## 2.5 Run Procedures

There are a number of procedures which are carried out both before and after the actual growth of the epitaxial wafer and which we have found to be essential to successful wafer growth. Since these procedures are routinely followed as part of each of our epitaxial growth runs, it is appropriate that they be mentioned here.

Before a growth run commences, the furnace is allowed to warm up for two hours in the standby position, and one additional hour in the growth (or rolled on) position. This allows both the furnace and the reactor to reach thermal equilibrium. One-half hour before the furnace is rolled on, a polished and etched substrate is loaded into a vitreous silica sled and placed in the pre-growth position in the reactor. Substrates are polished with a bromine-methanol mixture. Immediately prior to loading, they are etched with a  $H_2SO_4:H_2O_2:H_2O$  (7:2:1) mixture, thoroughly rinsed with deionized water, and dried in a filtered stream of nitrogen.

The growth run starts with the insertion of the sled and substrate to the growth position. The first step is a five-minute preheat during which the substrate, retort oven, and heated line are brought up to temperature. The preheat is followed by a 20-minute step in which  $AsCl_3$  flowing down the grow line resaturates the gallium source while  $AsCl_3$  directed down the etch

line removes a thin surface layer from the substrate. These two steps (preheat and etch/presaturation) are included in every run. The growth sequence generally starts with Step 3.

Between growth runs, the retort and heated line are baked out for 45 minutes at 500°C. This removes any residual zinc or zinc iodide which may have been deposited in the retort or line. Following the bakeout, the furnace is rolled into the growth position (having been rolled back at the conclusion of the preceding run) with all zones set at >850°C.  $\text{AsCl}_3$  is admitted through both the etch and grow lines both to resaturate the source and to clean deposits off of the sled and reactor tube. Following this vapor etch/saturation, the reactor glassware (sled, dump tube, and end cap) is cleaned in aqua regia, dried, and replaced in the reactor tube. The system is then ready for the next run.

## 2.6 Growth of Multilayer Structures

Controlled and reproducible growth of multilayer structures requires growth and doping techniques that, in addition to providing reproducible growth rates and doping levels, are capable of rapid turn-on and turn-off of doping. This is especially important when sharp doping transitions over several decades or p-n junctions are required. If doping is not initiated or terminated quickly, broad interfaces and compensated p-n junctions will result. We demonstrated the capability of HI transport system for the production of multilayer p-type structures by growing wafers with doping profiles suitable for hole velocity samples.

Eight  $\text{p}^{++}\text{-p}^{++}$  sandwich structures were grown on semi-insulating substrates for the hole velocity measurements described in Sec. 4.0. The characteristics of the wafers are shown in Table 3. The arsenic trichloride mole fraction was set at approximately  $5 \times 10^{-3}$  and the zinc arsenide retort temperature was 380°C. The measured substrate temperature was 740°C. After the usual vapor etch, a five-minute growth pause was introduced during

TABLE 3  
CHARACTERISTICS OF p<sup>+</sup>-p-p<sup>+</sup> WAFERS

Run Number	Substrate Boule Slice	p <sup>+</sup> Buffer		p Active			p <sup>+</sup> Contact	
		Co <sup>*</sup> (pF)	t (μm)	Near Buffer (× 10 <sup>15</sup> cm <sup>-3</sup> )	Median (× 10 <sup>15</sup> cm <sup>-3</sup> )	Near Contact (× 10 <sup>15</sup> cm <sup>-3</sup> )	Co <sup>*</sup> (pF)	t (μm)
51304	SE3-108	300	1.1	5.0	3.8	3.0	487	0.4
51305	SE3-113	NA	3.9	3.5	4.5	5.0	450	2.0
51306	SE3-114	380	4.0	10.0	15.0	20.0	390	2.0
51307	SE3-115	NA	3.8	7.0	10.0	15.0	365	2.0
51308	SE6-305	366	3.9	7.0	15.0	23.0	367	2.0
51309	SE6-306	401	4.0	7.0	6.0	6.5	357	2.0
51310	SE6-308	345	3.8	7.0	4.8	5.5	400	1.9
51311	SE6-307	NA	3.8	14.0	7.3	8.6	330	1.9

\* for 16 mil diam Schottky

which the same flow of nominal 10,000 ppm hydrogen iodide to be used to grow the  $p^+$  layers, was directed, together with the helium flush, through the zinc arsenide retort. The  $p^+$  layer was grown with a high HI concentration, followed by another growth pause, the low doped p region, and finally the  $p^+$  contact layer. Various growth pauses and hydrogen iodide flows were tried in an attempt to flatten the long p-active layer. The growth conditions for these wafers are listed in Table 4.

The uniformity of doping through the thickness of the p-active layer is particularly difficult to determine in thick samples such as these because of the deep step etches required for measurement. In general, however, the results indicate that we can achieve reasonably flat p-type doping using the hydrogen iodide process in the range from  $5 \times 10^{15}$  to  $2 \times 10^{16}$  holes per  $\text{cm}^3$ .

Either because of a thin  $p^+$  buffer or excessive nonuniformity of the p-active layer, several of these wafers were not processed into hole velocity samples. Of the wafers processed, only 51306 and 51310 yielded devices from which measurements could successfully be taken. Their profiles, reconstructed from C-V measurements on step-etched samples, are shown in Figs. 11 and 12.

TABLE 4  
GROWTH CONDITIONS OF p<sup>+</sup>-p<sup>+</sup> WAFERS

Wafer	Pregrowth Pause (min)	p <sup>+</sup> Buffer		Pause		p Active		p <sup>+</sup> Contact	
		Time (min)	HI (ppm)	Time (min)	HI (ppm)	Time (min)	HI (ppm)	Time (min)	HI (ppm)
51304	0	5	59	10	0.9	25	0.9	2	59
51305	5	20	59	10	1.6	180	1.6	10	59
51306	5	20	58	10	2.8	120	2.8	10	58
51307	5	20	59	10	2.1	120	2.1	10	59
51308	5	20	55	10	2.0	100	2.0	10	55
51309	5	20	75	0.5	1.5	100	1.5	10	78
51310	5	20	152	0.1*	1.6	100*	1.6	10	152
51311	5	20	146	2.0	1.9	100	1.9	10	152

\* Programmer malfunction, times uncertain

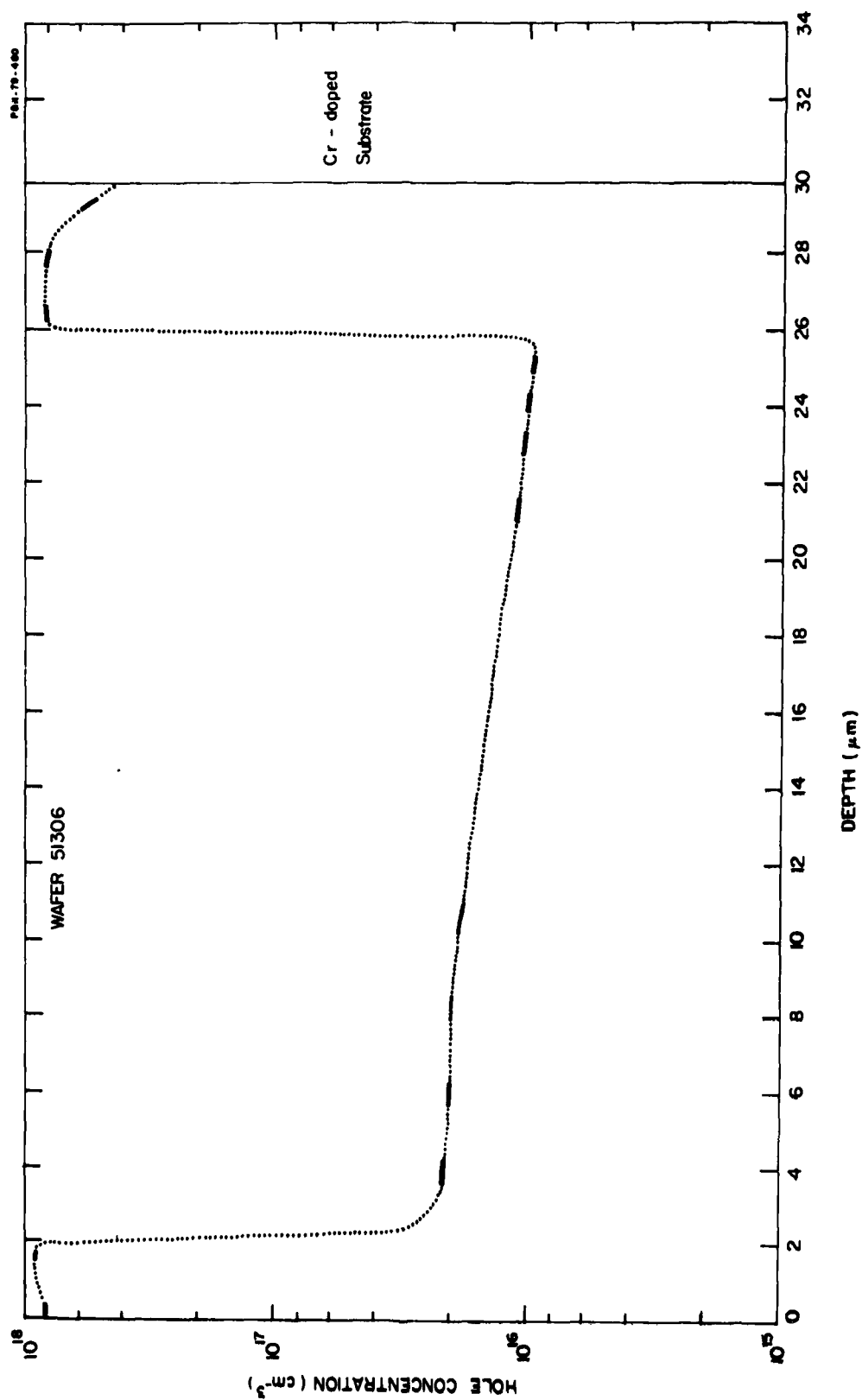


Figure 11. Doping Profile of Wafer 51306. Solid lines represent actual C-V measurements taken on a step-etched sample.

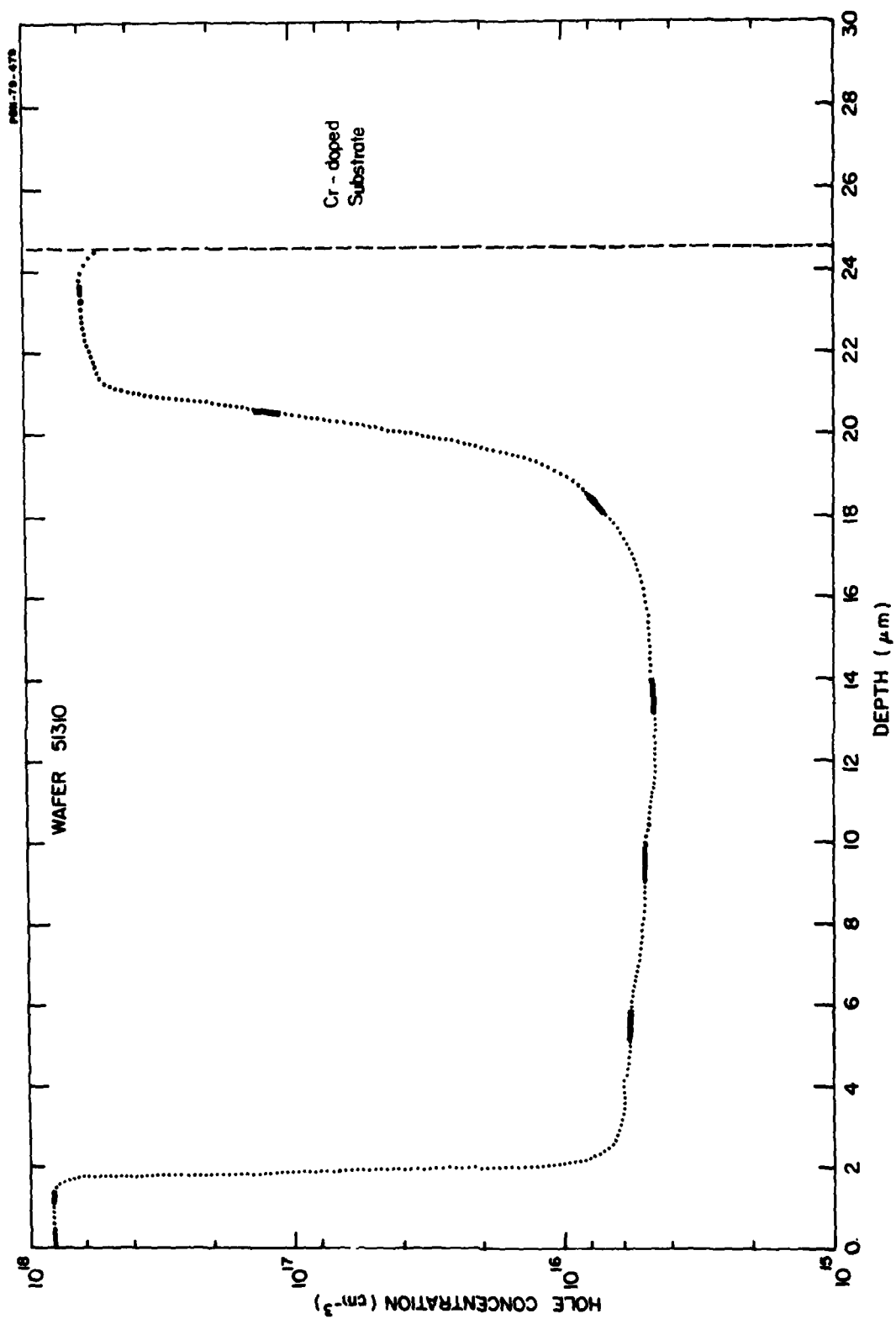


Figure 12. Doping Profile of Wafer 51310. Solid lines represent actual C-V Measurements taken on a step-etched sample.

## 2.7 $n^{++}p$ Junction Growth

One of the goals of this work was to develop growth techniques for the reliable production of p-n junctions of high durability. In addition, since the n-type side of the p-n junction also functions as a contact layer to which an ohmic contact must be made it was important that a technique be developed such that a highly doped  $n^{++}$  layer could be grown directly adjacent to the p-type epitaxial layer. During the third quarter of the contract period, such a technique was developed. We now routinely grow  $n^{++}$  contact layers with surface capacitance values in excess of 2000 pf, on 16 mil diameter diodes on top of our p-epi layers. This zero bias capacitance corresponds to carrier concentrations greater than  $10^{19} \text{ cm}^{-3}$ . Moreover, the doping density remains greater than  $10^{18} \text{ cm}^{-3}$  throughout the  $n^{++}$  contact layer.

The growth sequence which we have developed for the production of p-Read wafers with  $n^{++}$  contacts is discussed fully in Sec. 2.8 (and shown in Table V in that section). Of interest here are steps 16 to 20 which constitute the  $n^{++}$  contact layer portion of the growth program. They are:

<u>Step</u>	<u>Step Name</u>	<u>Duration (min.)</u>	<u>Event</u>
16	Pause-purge	2.5	Purge reactor of p-type dopant
17	Pause-condition	1	Condition reactor with low silane
18	Junction	1	Form p-n junction with low silane
19	Contact	2	Form $n^{++}$ contact with high silane
20	Terminate	1	Establish surface doping with high silane

We have found that when doping transitions are made, it is frequently necessary to insert a growth pause, which allows excess dopant to be swept out of the reactor. In addition, when changing over from p-type to n-type doping, or the reverse, it is necessary to condition the reactor by allowing doping gases (silane in the case of n-type doping) to flow through the reactor while growth of the epitaxial layer is temporarily halted. These two types of pause steps are referred to respectively as purge and condition. Having



established an equilibrium concentration of n-type dopant in the reactor (via the pause-condition step), growth of the epitaxial layer is resumed without changing the concentration of the dopant which enters the reactor. This results in the formation of an abrupt p-n junction (step 18). In order to form the highly doped  $n^{++}$  contact layer, the concentration of the dopant flowing into the reactor is increased for the final two minutes of growth (step 19). The concentration of silane in the reactor during these two steps is approximately 1.3 ppm (low silane) for the junction and 3.7 ppm (high silane) for the contact. We have also tried forming the junction and contact in a single growth step using 3.7 ppm silane, but we have detected no difference in structure or breakdown characteristic between the two techniques. Both of the p-type Read growth runs (X-band and Ka-band) were carried out using the two-step technique.

In order to form a good ohmic contact to the diode, it is desirable that the surface layer be highly doped. We found that when both growth and doping were discontinued simultaneously, the carrier concentration fell off in the surface layer. To avoid this problem, we allow the high silane flow to continue for one minute after growth has been discontinued. This procedure results in a surface layer which shows no fall off in doping and allows us to make ohmic contact to the wafer easily.

Unfortunately, despite the success we have had growing highly doped  $n^{++}$  layers on p-type epitaxy, the durability of our junctions has not been as great as we had hoped for. We consistently measure low reverse breakdown voltages (6 to 15 volts at 1 mA) on our mesa samples. In addition, the breakdown does not occur sharply but rather occurs over an extended voltage range giving rise to "soft shoulders" in the mesa I-V curves. We believe that the low breakdown voltages and soft I-V curves are symptoms of junction non-uniformity or tunneling. Several attempts have been made to identify the cause(s) of these symptoms (discussion of this point is contained in Sec. 3.0) but as yet we have not been able to explain the results.

## 2.8 p-Read Growth

A primary goal of the growth experiments described in preceding sections

of this report was to develop a growth program capable of producing p-Read structures to specifications with both high reliability and good reproducibility. The growth program must provide for the production of controlled doping levels, sharp doping transitions, and controlled layer thicknesses in order to produce the desired doping profiles. The sequence of steps which comprises the growth program will naturally reflect both the order of layer growth and the requirements of doping and layer thickness control just mentioned.

The low-high-low p-Read structure consists of four distinct layers which are, respectively,  $p^{++}$  contact, p active (or drift), p spike, and  $n^{++}$  contact. The layers may be grown either in the order listed or in the reverse order, depending upon the type of substrate used (i.e., p-doped, n-doped, or semi-insulating). We chose to use chromium doped semi-insulating substrates for the final production runs of p-Read wafers and to grow our p-Read structures starting with the  $p^{++}$  contact (buffer layer) and growing successively the p-active, p-spike, and  $n^{++}$  contact layers. Although we were successfully able to grow Read like structures on zinc doped substrates, a limited supply of high quality Zn-doped substrates and the contribution of Zn-doped substrates to p-type background in the VPE reactor led us to use Cr-doped substrates for the final growth runs.

Table 5 lists the sequence of steps which comprise our p-Read growth program. In addition to the actual growth steps, there are a number of steps (called pauses) in which no epitaxial layer growth occurs. Each of these pauses is inserted into the growth program for a specific purpose (e.g., to purge the reactor of residual dopant gases, condition the reactor for subsequent doping, etc.) and we have found that such steps are essential to the growth of well defined, uniformly doped layers.

Following the preheat and etch/presaturate steps (Sec. 2.5), the buffer layer is grown to a thickness of about 7  $\mu\text{m}$  using a concentration of about 3.1 ppm  $\text{I}_2$  in the gas stream. Growth of the buffer is followed by a short etch back in which  $\text{AsCl}_3$  is introduced through the etch line in order to remove 1-2  $\mu\text{m}$  of the buffer layer. This procedure helps to insure uniform doping up to

TABLE 5  
SEQUENCE OF STEPS USED TO GROW P-READ WAFERS

<u>Step</u>	<u>Event</u>	<u>Duration (min.)</u>	<u>Purpose</u>
1	Preheat	5	Equilibrate substrate at growth temperature
2	Etch/Presaturate	20	Saturate Ga source; etch substrate
3	Buffer	25	Grow $p^{++}$ buffer
4	Pause-etchback	5	Etchback buffer
5	Pause-purge	15	Purge reactor of residual p-type dopant
6	Pause-condition	20	Equilibrate reactor at doping level of active
7	Active	8	Grow p active layer
8	Pause	1	Allow for active layer aftergrowth
9	Pause-condition	1	Condition reactor for p spike
10	Pause	1	Establish reservoir concentration
11	Reservoir seal	.33	Seal reservoir
12	Spike inject	.17	Inject p spike
13	Spike aftergrowth	.17	Allow for spike aftergrowth
14	Pause-purge	5	Purge reactor of residual p-type dopant
15	Spacer	.5	Grow spacer
16	Pause-purge	2.5	Purge reactor
17	Pause-condition	1	Condition reactor for n-type doping
18	Junction	1	Grow p-n junction and $n^{+}$ contact layer
19	Contact	2	Grow $n^{++}$ contact layer
20	Terminate	1	Establish high $n^{++}$ surface doping
21	Cooldown	45	Cool wafer prior to removal from reactor

the buffer/active interface. The procedure also acts to simulate the condition which exists in the reactor following the etch/presaturate step when a zinc substrate is used. Thus the remaining steps in the program are carried out intact regardless of whether a zinc or chromium doped substrate is used. Following the etchback, a pause is introduced during which time pure  $H_2$  and He flow through the reactor; purging residual p-type dopant in preparation for growth of the low-doped active layer. This purge is essential to the creation of an abrupt doping transition between buffer and active layers.

A second pause is used to condition the reactor for doping of the active layer. We have found that having once removed residual p-type dopant from the reactor, several minutes of conditioning with a low concentration of  $I_2$  are needed to establish an equilibrium doping level. Without this second pause, several microns of growth may occur before the desired doping level is attained. The concentration of  $I_2$  used to grow the active layer varies depending upon the desired doping level ( $5.0 \times 10^{15} \text{ cm}^{-3}$  for X-band wafers;  $2.0 \times 10^{16} \text{ cm}^{-3}$  for Ka-band wafers). When a highly doped buffer layer is grown prior to the active, we find that our retort oven and heated line become contaminated with residual p-type dopant (zinc or zinc iodide) which is not cleaned out during the pause-purge step (step 5). Subsequently, the amount of p-type dopant generated during the growth of the active layer depends not only on the concentration of  $I_2$  in the p-doping network, but also on the flow of He through the retort and heated line. We thus found it necessary to grow X-band wafers using "half flow" ( $\sim 27 \text{ sccm}$ ) of He during the active to attain the required doping level. Normal retort flow ( $\sim 56 \text{ sccm}$ ) was used for doping the active layer in Ka-band wafers.

Three pauses follow the active. During the first pause,  $I_2$  continues to flow through the retort and into the reactor at the same concentration which is used to dope the active layer. We have long known that epitaxial growth may continue for up to 30 seconds after the  $AsCl_3$  grow bubbler has been turned off, simply due to the finite travel time of the saturated gas stream down the grow line and into the reactor tube. By allowing  $I_2$  to flow into the reactor during step 8, we insure that any additional growth during that time will constitute

simply an extension of the active layer. During step 9, the reactor is conditioned with approximately 0.5 ppm  $I_2$  in preparation for injection of the spike. We use a reservoir technique for spike growth in which a predetermined concentration of  $I_2$  is established in our fixed volume reservoir (step 10). The reservoir is sealed (step 11) and the gas then injected through the heated retort into the reactor (step 12). A short aftergrowth period is included (step 13) so that any discrepancy between arrival times (at the substrate) of the grow and doping clouds will not affect the height or shape of the p spike. Following a purge step, 30 seconds of additional growth (the spacer) occurs. The purpose of the spacer is to establish the spike to junction distance. The spacer is nominally doped at the same level as the active layer, although we have found that bleed-off from the spike is sufficient to dope the spacer and thus it is unnecessary to inject  $I_2$  into the reactor during this step. Following growth of the spacer, a short pause is inserted to allow excess p-type dopant to sweep out of the reactor. The junction and  $n^{++}$  contact are then grown as outlined in Sec. 2.7. Wafers are allowed to cool down to about 50°C before being removed from the reactor and cleaved for characterization samples.

Figures 13 and 14 show doping profiles obtained from C-V data on step etched samples for typical X-band and Ka-band wafers respectively. The profiles clearly demonstrate our ability to make abrupt doping transitions and to grow uniformly doped layers. They also demonstrate that we have obtained good control of doping over the range  $10^{15}$ - $10^{18}$  cm<sup>-3</sup>.

Table 6 lists the important characterization data for the X-band growth series wafers (note: run No. 51650 was aborted before growth began due to equipment failure and thus runs 51646 through 51656 represent ten consecutive growth attempts). The data show good reproducibility from run to run and throughout the series. Table 7 presents similar data for the Ka-band growth series. Again good reproducibility is evident. It should be noted that the change from X-band to Ka-band runs took place without the need for intermediate calibration runs, an indication of the degree of control attained in our VPE reactor.

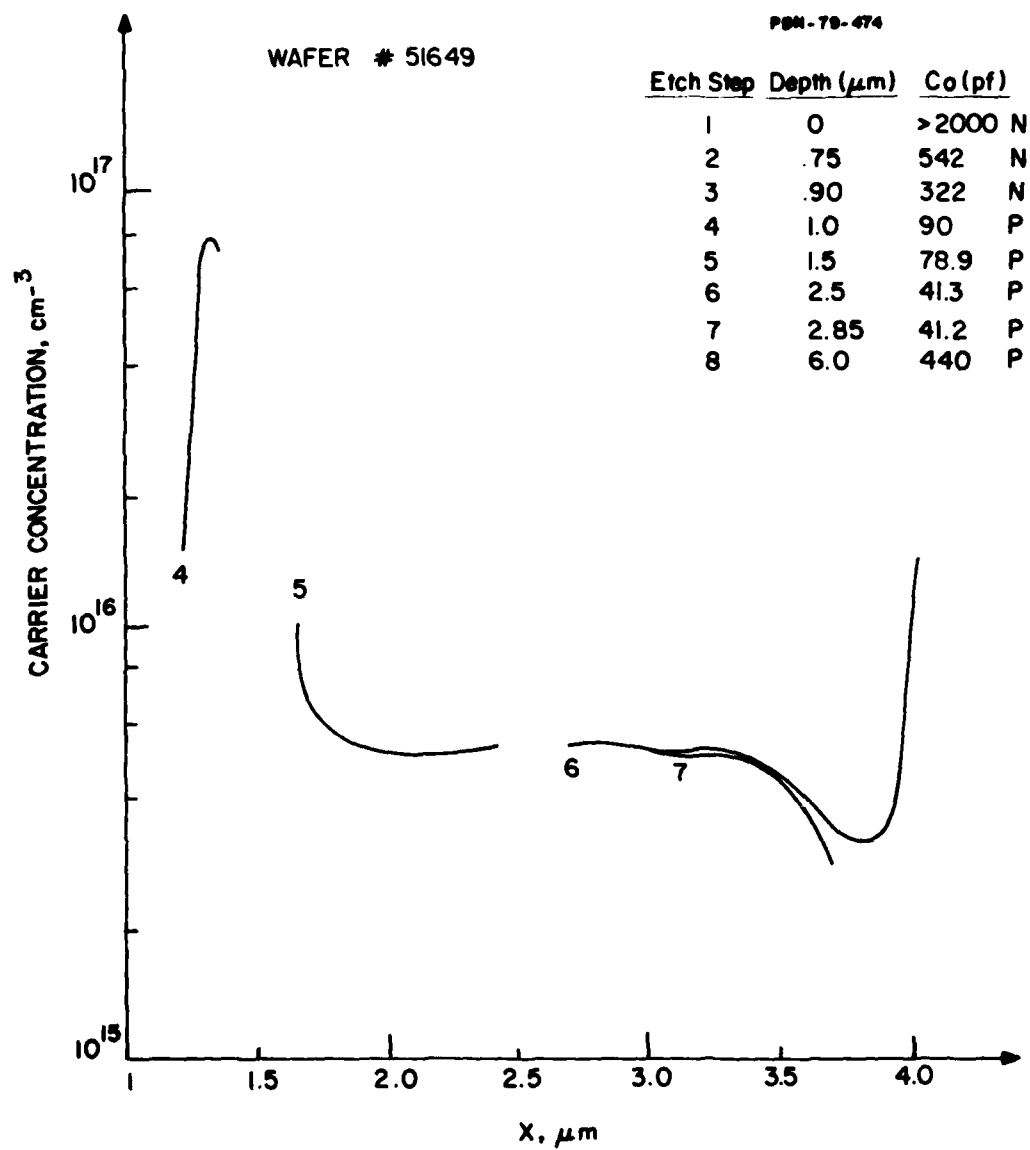


Figure 13 X-Band P-Type Wafer Profile.

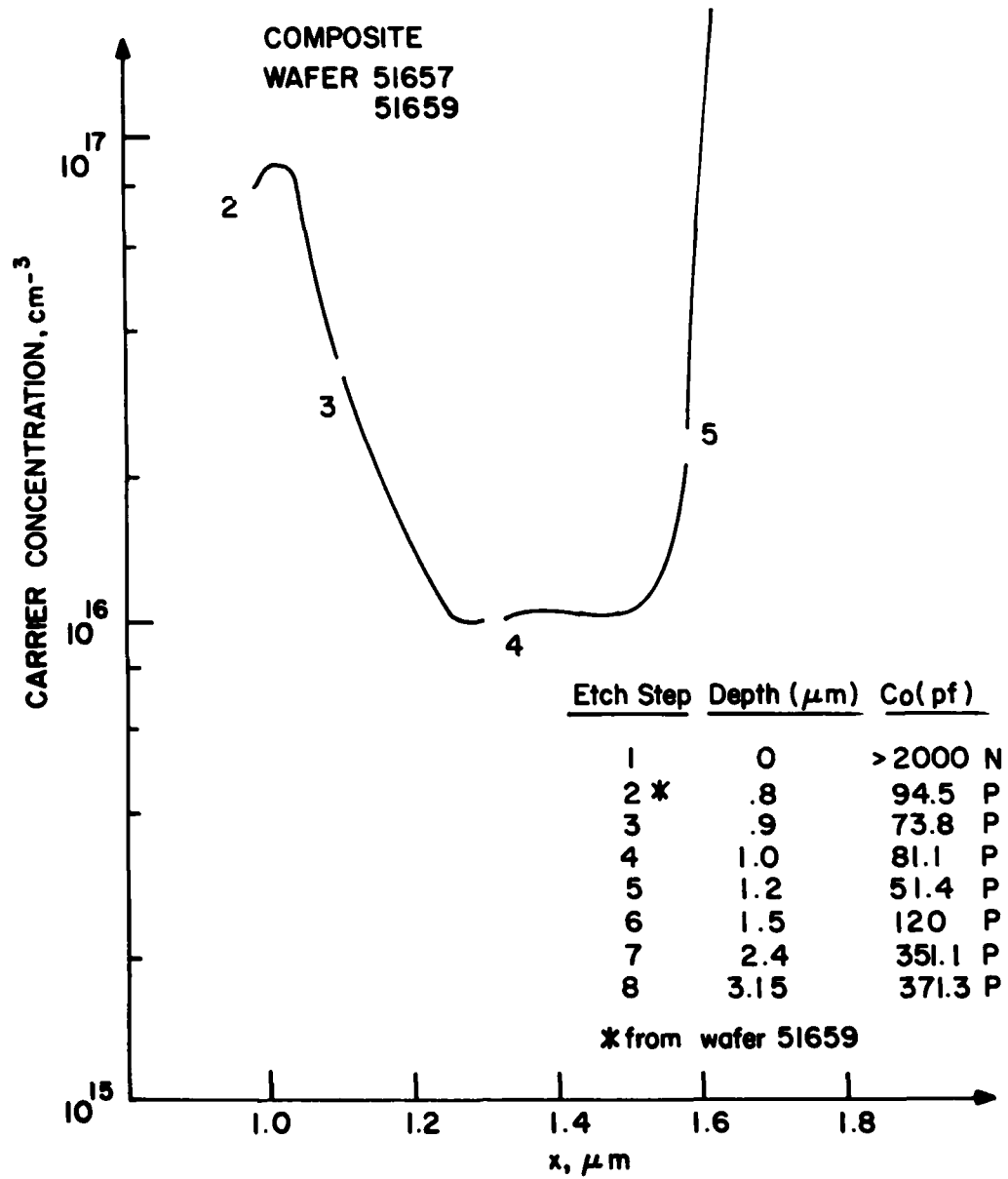


Figure 14. Ka-Band P-Type Wafer Profile.

TABLE 6  
X-BAND P-READ WAFERS

<u>Run Number</u>	<u>Active Doping</u> <u>(<math>\times 10^{15} \text{ cm}^{-3}</math>)</u>	<u>Spike Height</u> <u>(<math>\times 10^{16} \text{ cm}^{-3}</math>)</u>	<u>Spike Q</u> <u>(<math>\times 10^{12} \text{ cm}^{-2}</math>)</u>
51646	4.0	8.0	1.4
51647	6.5	7.6	1.3
51648	7.0	8.6	1.2
51649	5.2	7.8	1.4
51651	5.5	8.2	1.2
51652	~ 4.0	~ 7.6	1.3
51653	4.0	8.7	1.3
51654	3.0	NA	NA
51655	6.0	9.0	NA
51656	7.0	NA	NA

*Results of X-band growth series. In some cases the spike Q is not available (NA) due to a lack of C-V data over portions of the spike.*



TABLE 7  
Ka-BAND P-READ WAFERS

<u>Run Number</u>	<u>Active Doping</u> <u>(<math>\times 10^{16} \text{ cm}^{-3}</math>)</u>	<u>Spike Height</u> <u>(<math>\times 10^{16} \text{ cm}^{-3}</math>)</u>	<u>Spike Q</u> <u>(<math>\times 10^{12} \text{ cm}^{-2}</math>)</u>
51657	1.0	NA	NA
51658	2.7	6.6	.28
51659	1.2	9.0	1.0
51660	2.5	5.8	.3
51661	2.5	8.0	.7
51662	4.0	11.0	.7
51663	3.0	9.0	.65
51665	2.8	10.5	1.0
51666	2.5	9.6	1.0
51667	2.8	10.0	.98

*Results of Ka-Band Growth Series.*

*Data labeled not available (NA) is a result of incomplete C-V profiling.*

## SECTION III

### WAFER CHARACTERIZATION

#### 3.1 Introduction

A critical component of semiconducting material development is the ability to characterize the epitaxial wafers as fully as possible immediately after growth. This serves a twofold purpose: a) prompt feedback of growth results on a run-to-run basis, b) a wafer qualification process to select candidates for device fabrication.

In characterizing the semiconductor material, it is most important to measure the majority carrier concentration as a function of distance normal to the surface. This measurement is most commonly done by a differential capacitance method. The technique is discussed in Sec. 3.2. Description of the measurement system is given in Sec. 3.3. Sections 3.4 and 3.5 evaluate the inherent limitations of the method with particular emphasis on p-type GaAs, wafer uniformity, and problems associated with p-n junctions.

#### 3.2 Measurement Technique

The doping density as a function of depth is measured by means of the differential capacitance (C-V) technique (Hilibrand and Gold, 1960; Kernedy et al., 1968; Decker, 1968; van Opdorp, 1968). The capacitance resulting from a p-n junction or from the depletion zone of a Schottky barrier diode formed on the surface of the semiconductor is measured as a function of applied voltage. Then the doping density is given by

$$N = \frac{1}{q\epsilon} \frac{C^3}{A^2} \left( \frac{dC}{dV} \right)^{-1} \quad (1)$$

and the depth

$$x = \frac{\epsilon A}{C} \quad (2)$$

where  $C \equiv$  depletion layer capacitance  
 $A \equiv$  the area of the diode  
 $\epsilon \equiv$  the dielectric constant of the material  
 $q \equiv$  electronic charge.

Thus we must measure the capacitance of the depleted layer under the diode as a function of applied reverse bias and calculate  $N$  and  $x$  using Eqs. 1 and 2.

The avalanche mechanism limits the maximum voltage which can be applied to the junction and consequently the maximum depth to which a given junction can be used to establish the free carrier density distribution. Since the avalanche breakdown is a strong function of  $N$ , the maximum depth at which the semiconductor can be measured will vary rapidly with doping level.

The epitaxial semiconductor materials grown in our laboratory are complicated structures, where several layers of different doping levels, different thicknesses, and different types ( $n$  or  $p$ ) are grown sequentially in a vapor phase epitaxy reactor. It is usually necessary to measure the layers to a greater depth than that allowed by the breakdown voltage, which can be done by removing some material by etching from the surface of the sample to a predetermined depth,  $x_0$  and making a new diode on the etched surface. If  $x_0$  is known and added to the depth calculated from the diode data, then the profile at the total depth is obtained.

By piecing together the results of different diodes, made at different depths on the same sample, the profile through a whole semiconductor wafer can be reconstructed. We have found that for most materials we grow, eight diodes are sufficient to give an adequate knowledge of the doping profile. The wafer sample obtained from the growth laboratory is processed so that, by photolithographic techniques, eight diodes of a given area and located in a rigid pattern with respect to each other are formed at predetermined depths. A photograph of a finished characterization sample is shown in Fig. 15.



Figure 15. Characterization Sample Showing the 8 Diodes at Different Depth.

If the Schottky barrier diode is made too close to the p-n junction, the measurement of capacitance is no longer valid and as a consequence the data output is erroneous. To improve the knowledge of the doping profile near the junction, the capacitance versus voltage is measured on a mesa structure. In this case, ohmic contacts are evaporated and the depletion layer is measured solely at the junction. Here the measured effective capacitance, when entered in Eqs. 1 and 2, gives an effective carrier concentration,  $N_{eff}$  and  $x_{total}$

$$\frac{1}{N_{eff}} = \frac{1}{N} + \frac{1}{P} \quad (3)$$

$$x_{total} = x_n + x_p \quad (4)$$

By comparing the data from Schottky barrier diodes and mesa diodes, one can obtain a good reconstruction of the complete material profile.

### 3.3 System Description

A block diagram of the digital profiler constructed at Raytheon is shown in Fig. 16. The heart of the system is an Intel 8080 microprocessor-based digital computer. It operates with about 10K bytes of program memory (PROM) and about 6K bytes of random-access memory for data storage. Both digital and analog input/output channels are provided. The operator can converse with the machine via a teletypewriter which also serves as a paper tape punch, should a permanent record of data be desired. A standard laboratory X-Y recorder provides graphical output. Capacitances are measured with a digital-output bridge (Boonton 76A) to a precision of 0.01 pF. The bias voltage is provided by a D/A converter capable of an output of  $\pm 100$  V maximum with a minimum voltage increment of 1/32 volt and a current capacity of 100 mA. A depth sensitive instrument employing a linear variable differential transformer (LVDT) permits

PBN-78-481

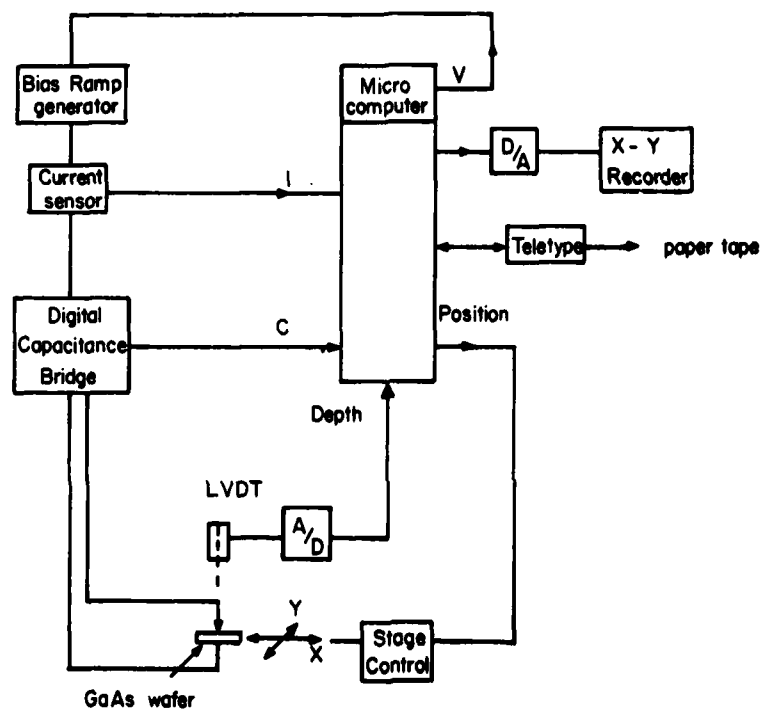


Figure 16. Block Diagram of the Digital Profiler.

the computer to measure etch pit depth to a precision of  $0.01\text{ }\mu\text{m}$ . The contact to the specimen is made by a probe which simultaneously provides coupling to the depth meter and allows electrical connection of the capacitance bridge and bias voltage source. A current sensing amplifier, mounted in series with the bias power supply, permits measurement of I-V characteristics of the diodes and monitoring of the leakage current when a reverse bias is applied. Finally, the sample is mounted on a table which can be positioned in two axes by the computer. The total excursion in each of the orthogonal directions is of the order of one inch.

### 3.4 Limitations of p-GaAs Material Characterization

The ability to accurately characterize the doping profile of p-type GaAs is perhaps the most important stepping-stone to the development and successful conclusion of this contract. In recent months we have made substantial improvements in our ability to profile p-type GaAs, particularly highly doped p-spike regions.

The doping profiles of p-spikes have been reconstructed by obtaining C-V profiles from conventional Schottky barrier diodes, in conjunction with the depth measurement of each etch step. The established criterion for the validity of the C-V method has been a leakage current of approximately  $100\text{ }\mu\text{A}$ . For n-type material, this criterion gives quite reliable results. However, for p-GaAs, the barrier height is quite low; consequently, at excessive leakage currents, large resistive effects will dominate the measured rf signal, limiting the range and accuracy of the measurement. This will manifest itself as a spike-like structure, i.e., a rapidly increasing doping profile. In order to prevent this misleading effect, the leakage current has been limited to 25 to  $40\text{ }\mu\text{A}$  in all of the measurements of the p-spikes as well as the drift regions.

Figure 17 shows that in spite of the low Schottky barrier height for p-GaAs it is possible to obtain reliable doping profiles using the conventional

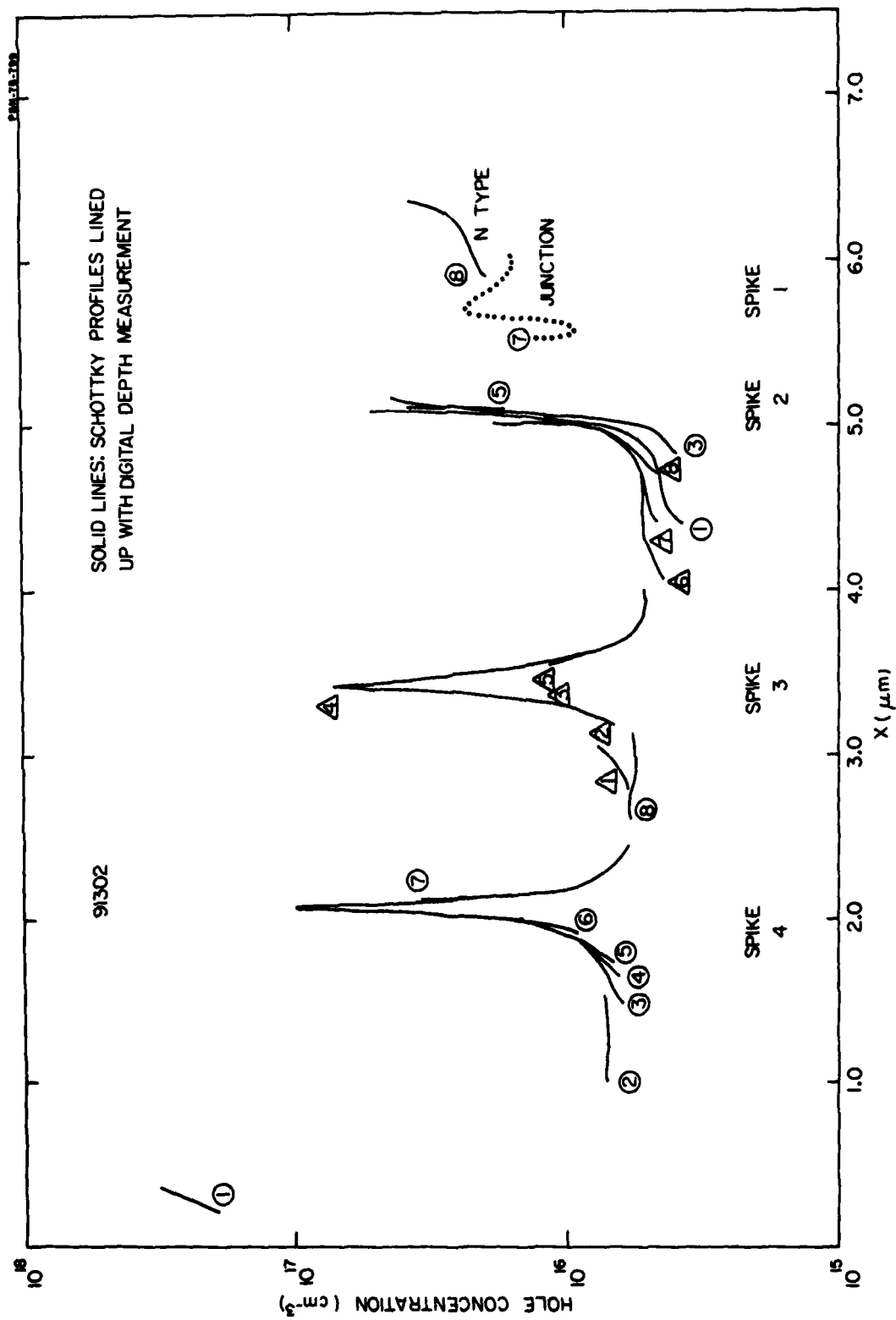


Figure 17. Doping Profile for Wafer 91302 Reconstructed from C-V Data Taken from Several Step-Etched Schottky Barrier Diodes. Solid lines are profiles positioned based on digital profiler depth measurements.



C-V method, provided the measured profile is sufficiently distant from the p-n junction. We were able to completely profile p-spikes approximately  $0.4 \mu\text{m}$  away from the p-n junction. However, the method fails to profile the p-spike at the junction, where accurate information is most needed. At best we were able to measure part of the spike as one is approaching from the drift region. At this point in time, it is necessary to measure mesa profiles in order to determine the necessary parameters on p-spikes.

Another artifact which can affect the accuracy of the doping profile obtained from C-V data is the series resistance ( $R_s$ ) from the undepleted region. Coupled with the low mobility of p-GaAs, this resistive effect can seriously distort the observed profile and also limit the accurate range of the measurement. In the absence of  $R_s$  in the equivalent circuit of the diode, the imaginary component of the rf signal is directly proportional to the depletion layer capacitance. However, for significant values of  $R_s$  the phase angle,  $\phi$ , between the real (R) and imaginary (C) parts of the signal deviates from  $90^\circ$ . The net effect is a lower measured capacitance, hence a larger depth  $x$  and a slightly lower value of doping density.

The effects of this phenomenon have been investigated by monitoring the phase angle during C-V profiling and correcting the measured capacitance. Wafer 91301-1 was chosen for this purpose, since etch step number 4 completely profiles the p-spike and the effects of  $R_s$  should be more pronounced. Figure 18 shows the results of the doping profile obtained from the conventional C-V data and the corrected profile obtained by monitoring  $\phi$ . Clearly, the two profiles are in excellent agreement and there are no distortions due to  $R_s$ .

In summary, it has been demonstrated that the conventional C-V technique gives accurate doping profiles on Schottky diodes for p-type material and that there are no serious distortions due to the series resistance, provided that the measured profile is sufficiently far away from the p-n junction. Mesa profiles are needed to obtain information on the spikes at the junction.

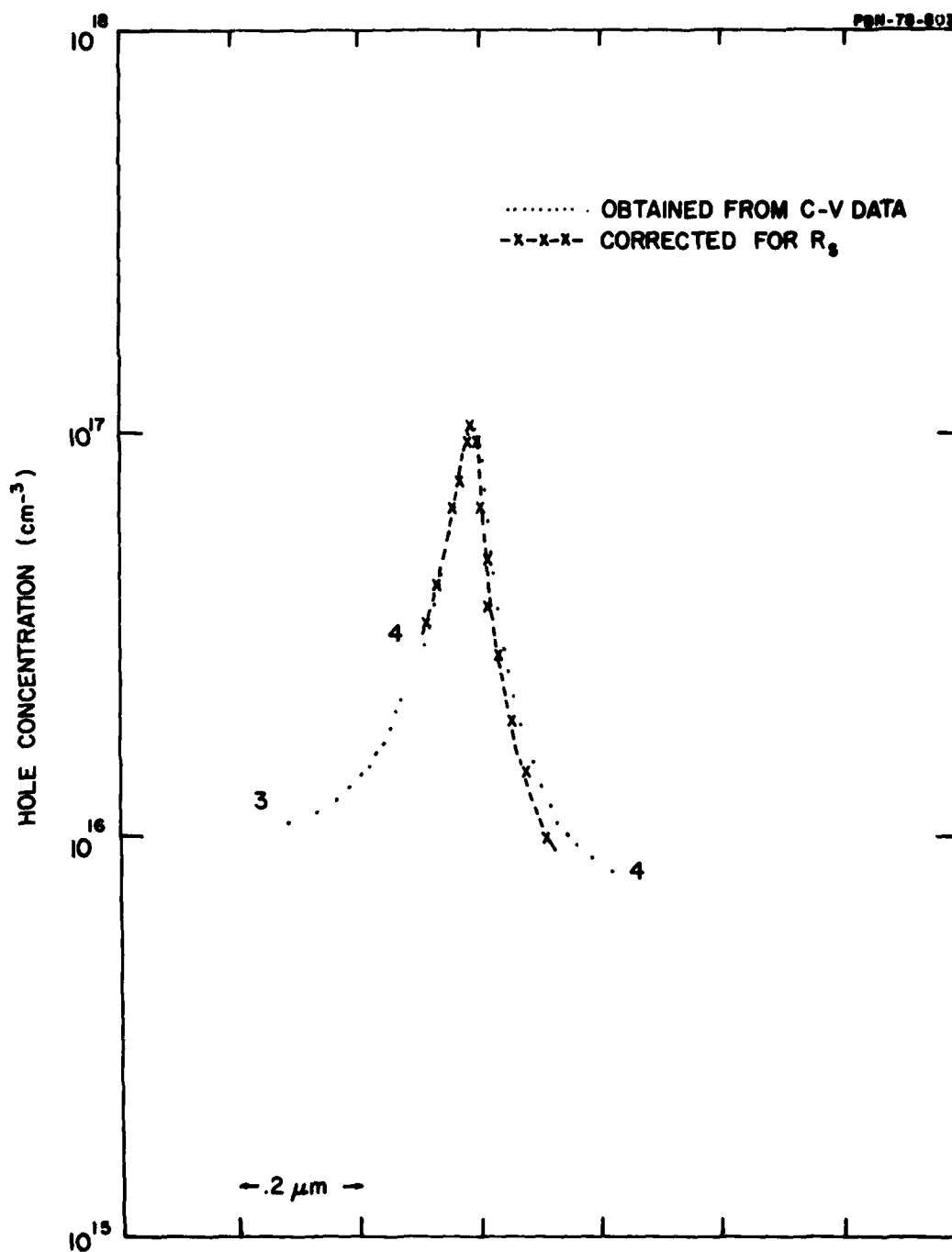


Figure 18. Doping Profile for Wafer 91301-1 Reconstructed from Third and Fourth Etch-Step of Schottky Barrier Diodes. The dotted line represents the data obtained from conventional C-V method. The dashed curve is the doping profile obtained after series resistance ( $R_s$ ) corrections have been applied.

### 3.5 Evaluation of p-n Junctions

As discussed above, mesa structures contain important information regarding the charge content of the spikes. We have recently conducted a series of measurements using mesa structures on highly doped  $n^{++}$ -p wafers grown in Reactor 5. Although we have made successful measurements on p-n junctions grown in other reactors, we encountered poor reverse breakdown on these  $n^{++}$ -p mesas. Hence we have undertaken an intensive study to investigate this phenomenon.

Possible sources for the observed problem are:

1. Defects in the substrate which propagate into the grown epi layer
2. Non-uniform junction formation
3. Poor ohmic contacts on mesas.

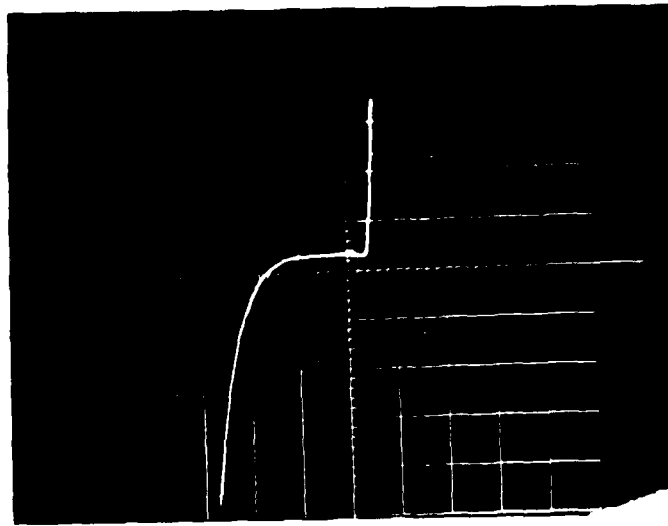
Defects in the substrate will cause a non-uniform doping across the wafer. To investigate this, we ran identical programs in the reactor except for the  $n^{++}$  contact layer. A surface capacitance map of this run (Fig. 19) indicates that the growth is quite uniform.

Next we addressed the question of non-uniform junction formation. We processed the entire wafer for mesa structure and measured junction capacitance which was extremely uniform (Fig. 20). We have repeated this experiment with Zn-doped substrates from a second boule (Fig. 21) and also with Cr-doped by growing a  $p^{++}$  buffer. All these experiments yielded identical results, indicating that 1) and 2) are not probable sources of the problem.

Our standard procedure on mesa structures is to evaporate Ag-Mn (which is also a p-type dopant) for ohmic contacts. Hence, it is possible that we inadvertently formed a double p-n junction. To investigate this, we have

154		157		157	
	158		160		158
161		162		159	
	164		164		158
164		159		161	
	161		155		159

*Figure 19. Surface Capacitance Map of Wafer 51636.*



Scale: 5V  $\leftarrow$ ; 2V  $\rightarrow$ ; .1 mA  $\uparrow\uparrow$

46.7	47.8	47.8	47.7	46.0	42.6
46.2	47.0	47.3	47.2	45.6	36.4

Figure 20. Junction Capacitance Map of Wafer 51618.  
Substrate: Zn-doped.



Scale: 5V  $\leftarrow$  ; 2V  $\rightarrow$  ; .1 mA  $\uparrow\downarrow$

48.5	42.8	
	43.8	41.7
44.4	41.1	
	42.4	40.4
42.8	39.5	
	41.6	39.3
44.0	39.0	

Figure 21. Junction Capacitance Map of Wafer 51631.  
Substrate: Zn-doped (different boule).

sputtered Au-Ge contacts. Figure 22 shows that there is virtually no difference in the ohmic contacts whether evaporated Ag-Mn, or sputtered Au-Ge.

Microplasma and soft I-V breakdowns can also occur if there are small non-uniformities in the material (of the order of a few hundred angstroms); such minute non-uniformities cannot be detected with our measurement capability. In order to improve the I-V characteristics and possibly to extend the measurement range, we decided to use a smaller-diameter mesa. We have processed a number of 3-mil mesas (standard size is 16 mils) and obtained improved reverse breakdown characteristics (Fig. 23). However, we were unable to extend the range of the measurement.

At this point, profiling these  $n^{++}$ -p mesa structures remains the only characterization problem to be solved. It is conceivable that the depletion zone is pinned to  $n^{++}$  on one side and to a highly doped p-spike on the other, so that the avalanche mechanism takes over and limits the extent of the applied reverse bias voltage.

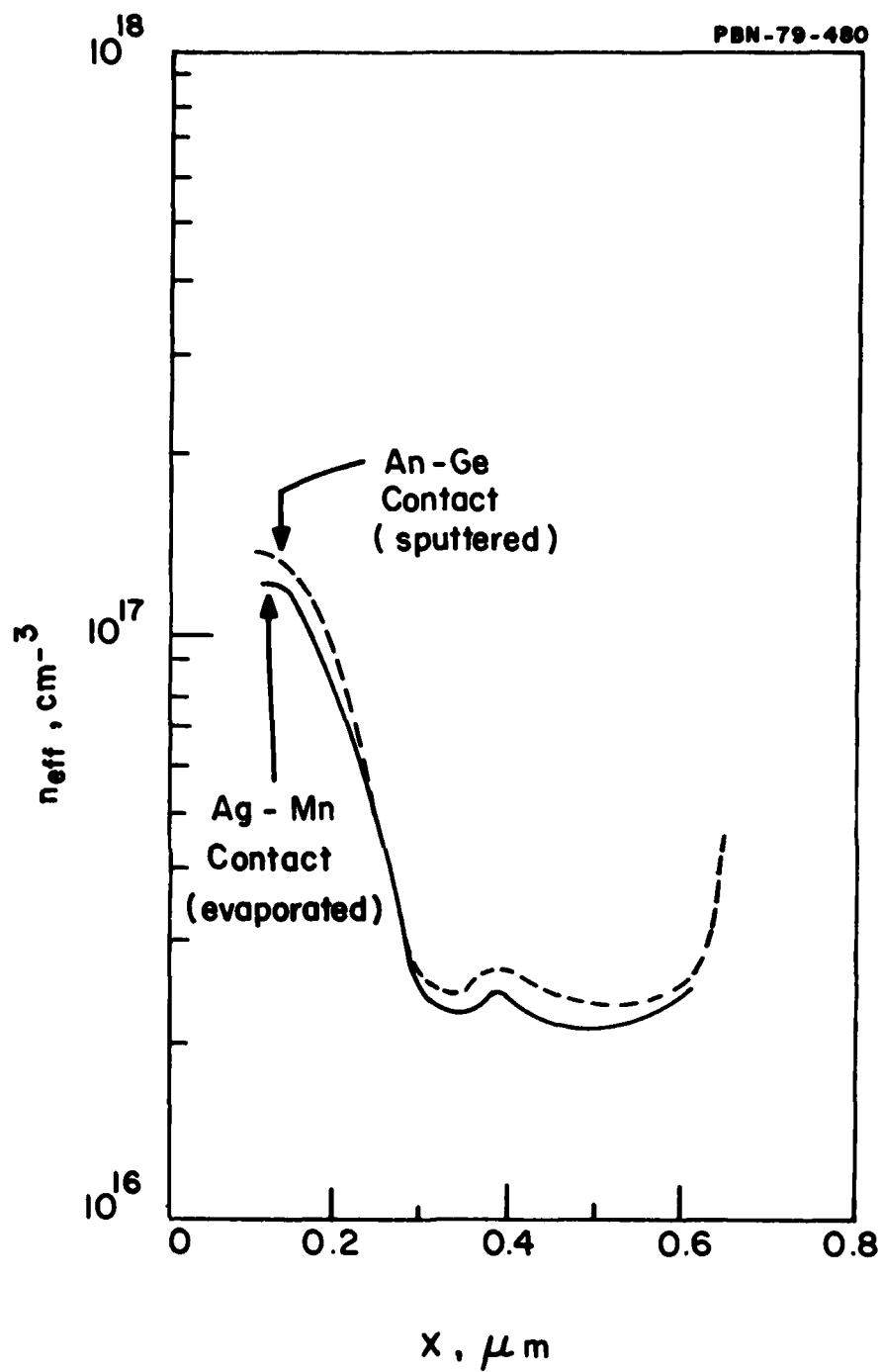
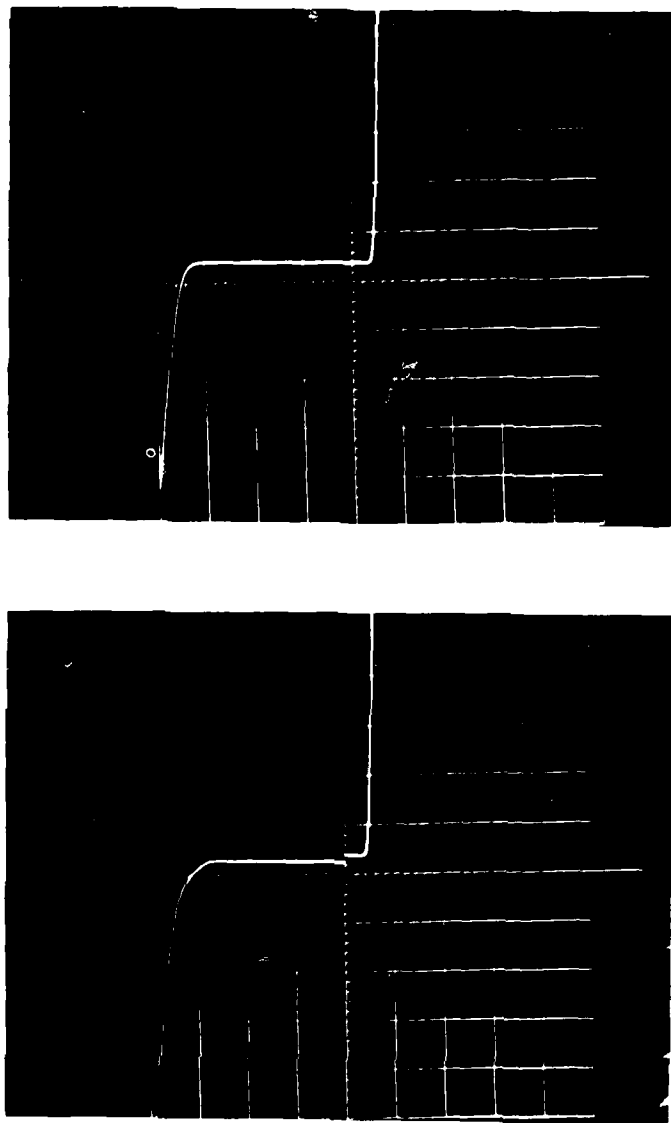


Figure 22 Mesa Structures Using Two Different Ohmic Contacts.





{ Scale:  
 5V ←  
 2V →  
 .1 mA ↑↓

Figure 23. Improved I-V Characteristics of 3 Mil Mesas.

## SECTION IV

### HOLE VELOCITY MEASUREMENTS

#### 4.1 Introduction

One of the principal goals of this contract was to provide accurate measurements of hole drift velocity on p-type gallium arsenide. The measurements were to be made over a range of electric field and temperatures, in order to provide useful data for device design and fabrication. In this section, we describe velocity measurements on GaAs samples whose active layers had acceptor doping levels of  $5 \times 10^{15} \text{ cm}^{-3}$  and  $2 \times 10^{16} \text{ cm}^{-3}$ .

The experiment required measuring the  $I(V)$  characteristics of samples using voltage pulses of sufficiently short duration and repetition rate to avoid significant heating. The geometries of the samples were measured accurately by means of SEM photographs with magnifications of 440 to 2200 $\times$ .

Our measurements have indicated saturated hole velocities which are close to the saturated electron velocities measured in n-GaAs by Houston and Evans (1977) but slower than earlier measurements of hole velocity in GaAs.

The earlier measurements of hole velocity in GaAs were reported in two papers by Dalal (1970 and 1971). His measurements indicated that the hole velocity, which was a linear function of field in the mobility range below  $10^4 \text{ V/cm}$ , increased more slowly with a further increase in field until it reached a saturated velocity. Dalal's first paper (1970) used a sample with a doping level of  $6 \times 10^{16} \text{ cm}^{-3}$ ; in this work, the electric field was not quite large enough to reach velocity saturation although a velocity  $v_p = 7.8 \times 10^6 \text{ cm/sec}$  was measured at room temperature when  $E = 6 \times 10^4 \text{ V/cm}$ . In the second paper, a saturated velocity of  $1 \times 10^7 \text{ cm/sec}$  was measured at room temperature in a sample with a doping level of  $1.1 \times 10^{16} \text{ cm}^{-3}$ .

The experiment which determines the hole velocity  $v_p(E)$  from  $I(V)$  measurements is described by Seidel and Scharfetter (1967). In the samples used by Dalal (1970, 1971), the sample length was taken long enough and the doping density was high enough so that space charge could be neglected. In

this case the determination of  $v_p(E)$  is simple and direct, as indicated by Fig. 24. Under these conditions, the field is uniform, except for a narrow space charge region next to the  $p^+$  ohmic contact, and has the magnitude  $V/\ell$  where  $V$  is the applied voltage. In the absence of space charge, the hole density  $p$  equals  $N_A$ , the acceptor density, so that the current is  $I = qAN_A v_p(E)$ . In this case the measured  $I(V)$  characteristic is a direct plot of  $v_p(E)$  provided the current is plotted as  $I/qN_A A = v_p(E)$  and the voltage is plotted as  $V/\ell = E$ .

The experimental geometry is illustrated by the schematic diagram in Fig. 25. Since the slope of the mesa walls is not large, the current density  $\vec{j}$  is approximately in the  $x$ -direction with the magnitude  $I/A(x)$ . Then Poisson's equation becomes

$$\frac{dE}{dx} = \frac{1}{\epsilon} \left( \frac{I}{A(x) v_p(E)} - q N_A(x) \right) \quad (1)$$

where the acceptor density  $N_A(x)$  and the area  $A(x)$  are known functions of  $x$ , which are measured by C-V profiling and SEM measurements respectively. Values of these functions are entered into the computer program by means of a spline routine. The hole velocity  $v_p(E)$  is considered known and also entered into the program as a spline function of  $E$ , as described in Sec. 4.3.

Our experimental samples were designed to have active thicknesses restricted to 25  $\mu\text{m}$  or less. These thicknesses were considerably shorter than Dalal's, which varied between 70 and 320  $\mu\text{m}$ , but had the advantage of shorter growth time for the samples and lower amplitude for the voltage pulses. This approach will make it easier to adapt our experiment to other electronic materials, although it has the disadvantage of requiring us to calculate a space-charge correction. For our samples this correction is generally small, on the order of 10-20 percent.

The second geometrical difference between our samples and Dalal's samples is that ours are in the shape of mesas. This has advantages in ease of fabrication and of heat sinking.

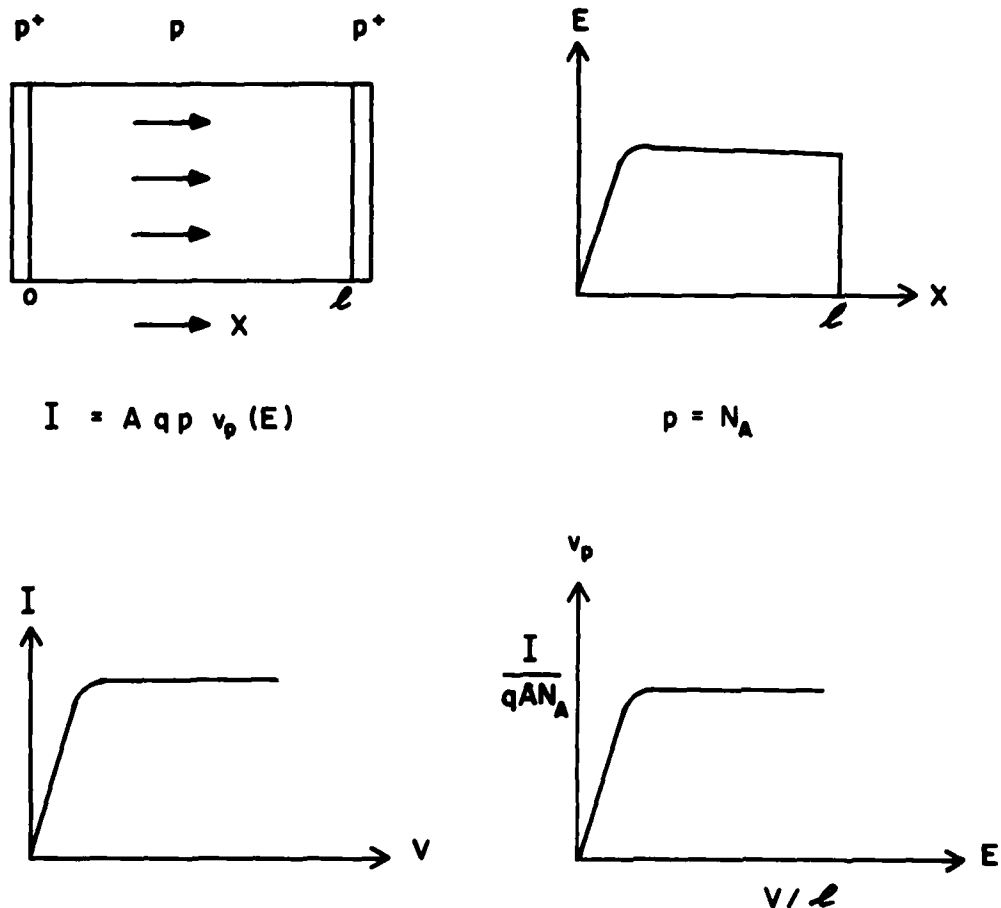


Figure 24 Schematic Diagram of Simplest Hole Velocity Experiment.  
 (a) Uniform cross section for p<sup>+</sup>-p-p<sup>+</sup> sandwich of length  $\ell$ .  
 (b) Electric field increases rapidly over a thin space charge region next to the p<sup>+</sup> ohmic contact and is uniform over most of the length, providing doping density and length are both large.  
 (c) Measured  $I(V)$  characteristic.  
 (d) Velocity versus field characteristic is identical to the  $I(V)$  measurement except for scale changes.

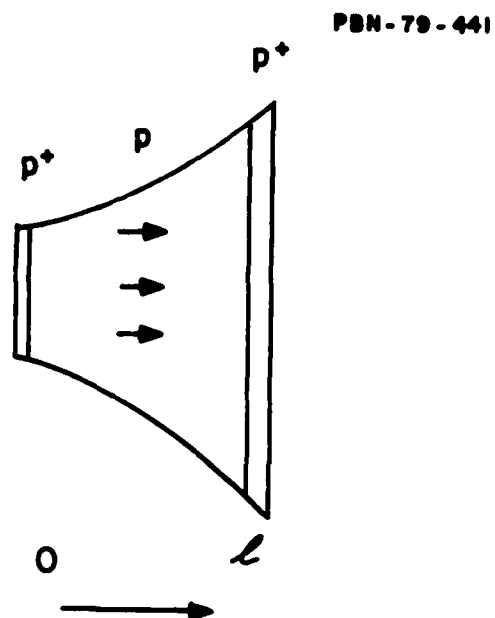


Figure 25 Sample Geometry for Experiment. Poisson's equation is solved with spatially varying cross section  $A(x)$  and acceptor doping  $N_A(x)$ , as well as field-dependent velocity characteristic,  $v_p(E)$ .

The characteristics of the velocity measurement samples are summarized in Table 8. Successful measurements were made with the first two lots, but burnout problems prevented sufficient voltage to Lot No. VMS-279.

#### 4.2 Measurement Technique

##### 4.2.1 Determination of area and doping densities

The acceptor doping levels of the  $p^+-p-p^+$  sandwiches are measured as a function of depth, by C-V measurements using either the analog or digital profilometers as described in Sec. 3.0. The area of the Schottky contact used in the profile characterization is an important parameter, since the measured carrier density is proportional to  $1/A^2$ . The density as a function of depth is determined by a series of etches, as described in Sec. 2.6. The doping profiles are generally flat but the computer program has been designed so that variations in doping profile can be handled when they occur.

The area of the mesa cross sections are nominally 8 mils in diameter. However, the active mesa cross section as a function of depth is determined by taking SEM microphotographs of each mesa used in the actual velocity measurement. For example, Fig. 26 shows SEM photographs of Device No. 7, from Lot No. VMS-278 which was used in the temperature dependent measurements of velocity. The upper photograph shows a magnification of 440 $\times$  which is used to obtain the top diameter of the mesa. The bottom photograph, with a 2200 $\times$  magnification, is used to measure the taper of the mesa wall. In practice, the radius is measured at five points separated by 1/4 of the mesa height. For calculation purposes, these points are then treated as the "knots" of a spline routine, which then determines the entire function  $A(x)$  by connecting every two "knots" with a cubic polynomial.

##### 4.2.2 Experimental setup

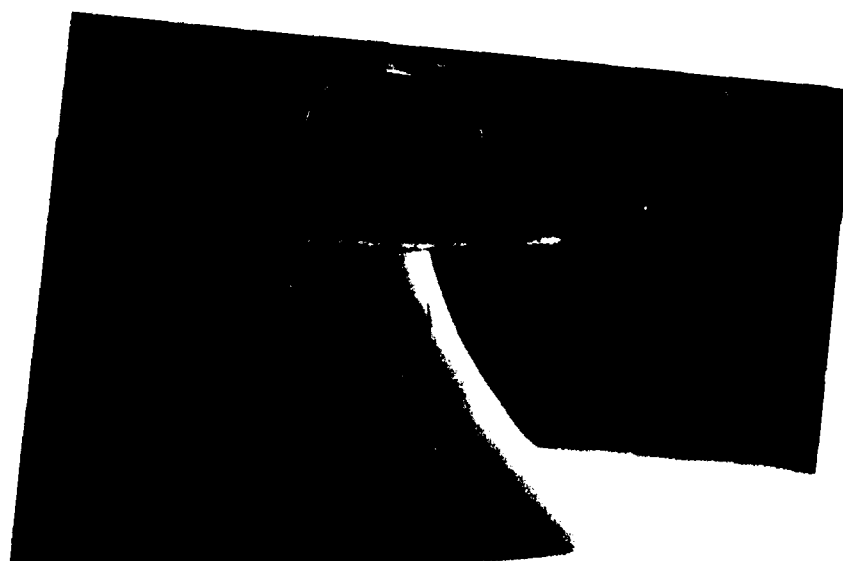
The pulse generator and electronic network are arranged as shown in Fig. 27. For the device under test (DUT) the I-V characteristic is obtained from

TABLE 8  
CHARACTERISTICS OF p<sup>+</sup>-p-p<sup>+</sup> VELOCITY MEASUREMENT SAMPLES

VMS Lot No.	Wafer No.	Buffer Contact		p Active Layer			Surface Contact	
		Thickness ( $\mu\text{m}$ )	Doping ( $\times 10^{18} \text{ cm}^{-3}$ )	Near Buffer ( $\times 10^{15} \text{ cm}^{-3}$ )	Near Center ( $\times 10^{15} \text{ cm}^{-3}$ )	Near Contact ( $\times 10^{15} \text{ cm}^{-3}$ )	Thickness ( $\mu\text{m}$ )	Doping ( $\times 10^{18} \text{ cm}^{-3}$ )
270	51306	4.0	0.9	10	15	20	23.9	0.9
278	51310	3.8	0.8	7	4.8	5.5	17.3	0.9
279	51311	3.8	0.15	14	7.3	8.6	18.8	0.35



(a)



(b)

Figure 26 Microphotograph of Mesa Device. a. The 440 $\times$  enlargement allows the diameter of Device No. 7, VMS-278 to be measured. This device has been etched to 90 percent of its nominal area. b. The 2200 $\times$  enlargement is used in determining the slope of the mesa walls.



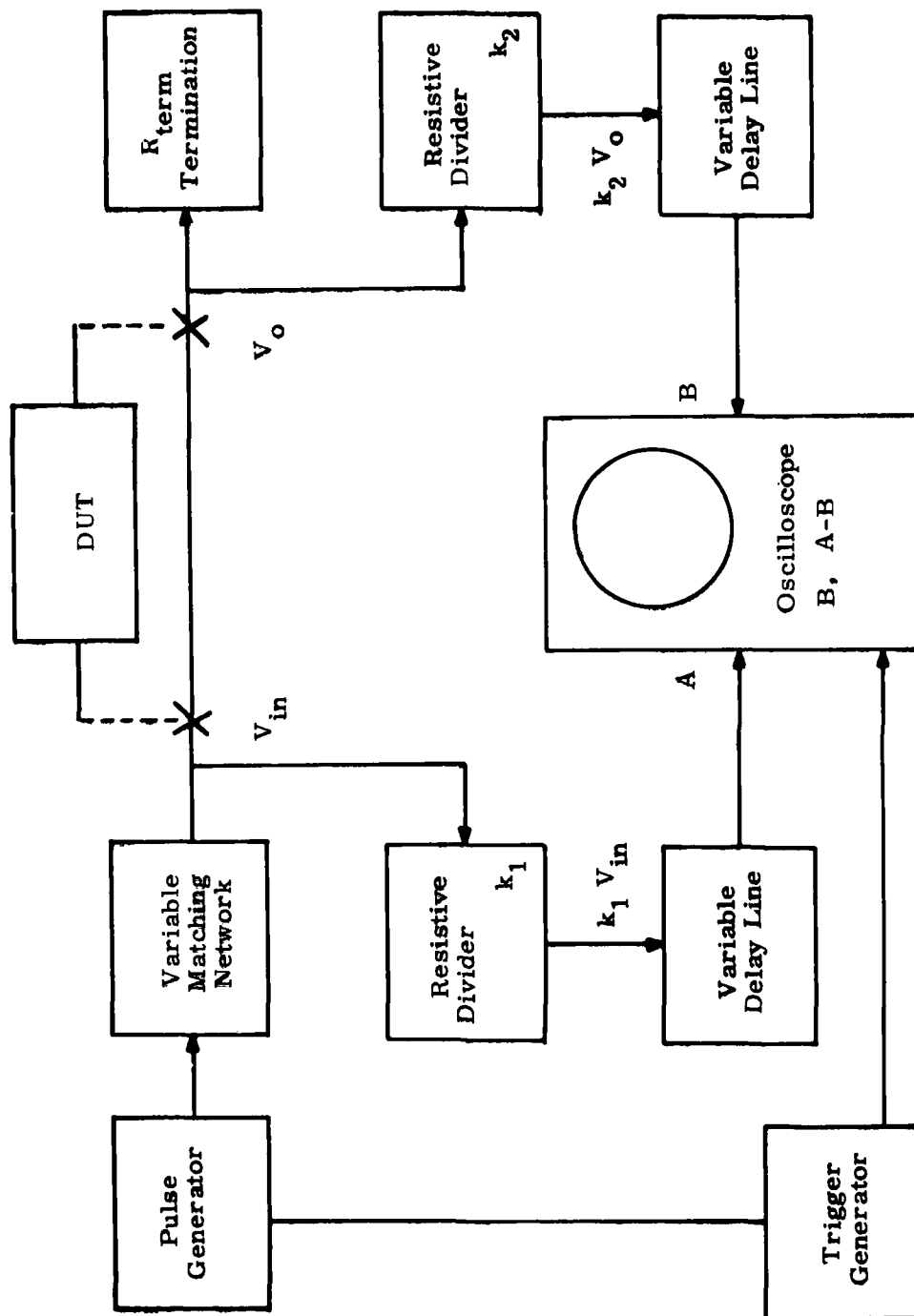


Figure 27 Diagram of the Equipment for Hole-Velocity Measurements.

$$V = V_{in} - V_o$$

$$I = V_o / R_{term}$$

The results are directly displayed on two channels of the oscilloscope and manually plotted. The error in reading this display under pulsed conditions was less than ten percent, as was determined by replacing the device with a standard carbon resistor of comparable resistance. For the usual range of interest,  $k_1$ ,  $k_2$ , and  $R_{term}$  are selected so that  $k_1 = k_2$  and  $V_{in} - V_o \approx V_o$ . This choice yields equal accuracy and resolution in the two oscilloscope channels.

#### 4.2.3 Thermal effects

The pulse generator produces pulse lengths of the order of 50 ns, which are designed to be short enough to prevent significant heating of the active layer. The heating occurs so rapidly that no heat is conducted away from its generation point and

$$\Delta T = \frac{j \cdot E}{\rho C_V} \Delta t \quad (2)$$

Taking the peak field to be  $1 \times 10^5$  V/cm and  $j = I/A$  where the peak value of  $I$  is 3 amps and  $A = 3.2 \times 10^{-4}$  cm<sup>2</sup>, the maximum heating when the measurement is taken at  $t = 20$  ns, appears to be less than 10°C. However, both  $j$  and  $E$  have their maximum values at the narrow cross section at the top of the mesa. For example, the maximum field for a current of 3 amps in VMS-270 has been calculated as  $1.1 \times 10^5$  V/cm while the spatially averaged field is only  $5.6 \times 10^4$  V/cm. Therefore an experimental check was considered necessary and is shown in Fig. 28. Normally, both  $I$  and  $V$  are measured at the leading edge of the voltage pulse after 20 ns. For comparison a second measurement was taken at the trailing edge of the pulse after 70 ns. If there was significant heating of the sample, the hole velocity would drop because of the increased temperature and the measured current would be significantly lower after 70 ns. Since there is very little change, we are confident that

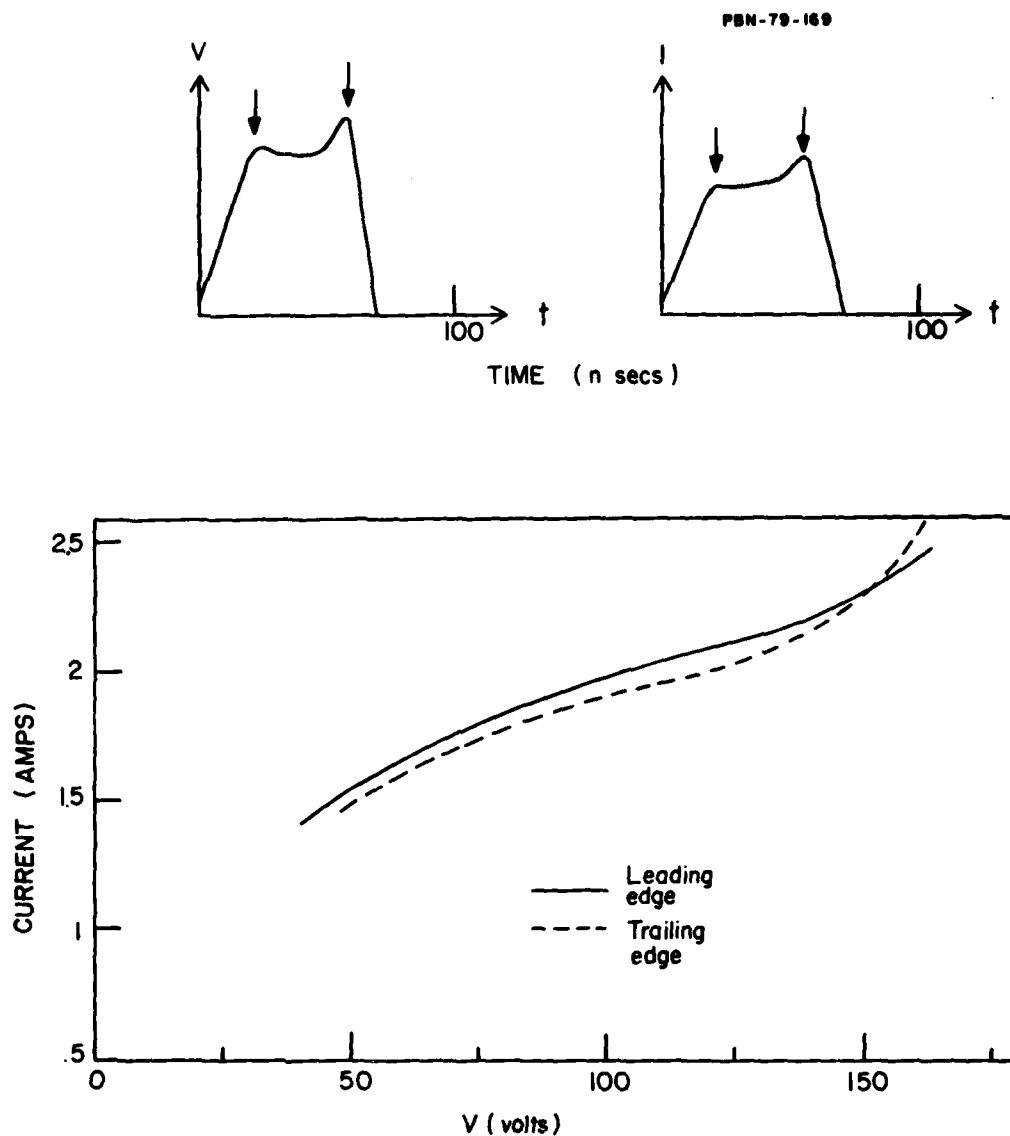


Figure 28 a. Schematic Plots of Voltage and Current. b. I-V plots from VMS-270, device No. 8. Solid curve is taken at the leading edge after 20 ns. Dashed curve is taken at the trailing edge after 70 ns.

the heating effect during the first 20 ns is small. The effect remained qualitatively the same from device to device and with normal changes in the pulse envelope as shown by Fig. 29.

#### 4.2.4 Data validation

We measured the I-V characteristics from a number of devices which are ostensibly identical to ensure that the data was reproducible and not peculiar to a particular device. For example, Fig. 30 shows I-V measurements for five devices from Wafer No. 51306. (To avoid confusion, the complete curve is shown only for device 5; the X's mark the highest voltage and current on the measured I-V curve for the other devices.)

There are several points to comment upon. First, the maximum voltage which can be applied before burnout varies significantly with each device. (Most of these devices were not actually burned out, because the approach to burnout usually causes abnormalities in the oscilloscope trace, which allows us to stop increasing the voltage before the device actually burns out.) Second, we see that five devices had essentially the same curve except for some variation in burnout voltage.

The validity of our experimental measurement was checked by electrolytically etching the finished device to reduce its area. This provides a test of current uniformity and also improves our ability to measure the area accurately with the aid of SEM photomicrographs. The electrolytic etch acts on p-type GaAs in a manner which turns the mesas into right circular cylinders. In this way we were able to make measurements on devices with constant cross sections.

This effect is dramatically indicated by SEM photographs. Figure 31 shows device No. 3, which is etched to a nominal 50 percent of its original area, producing a nearly perfect right circular cylinder.

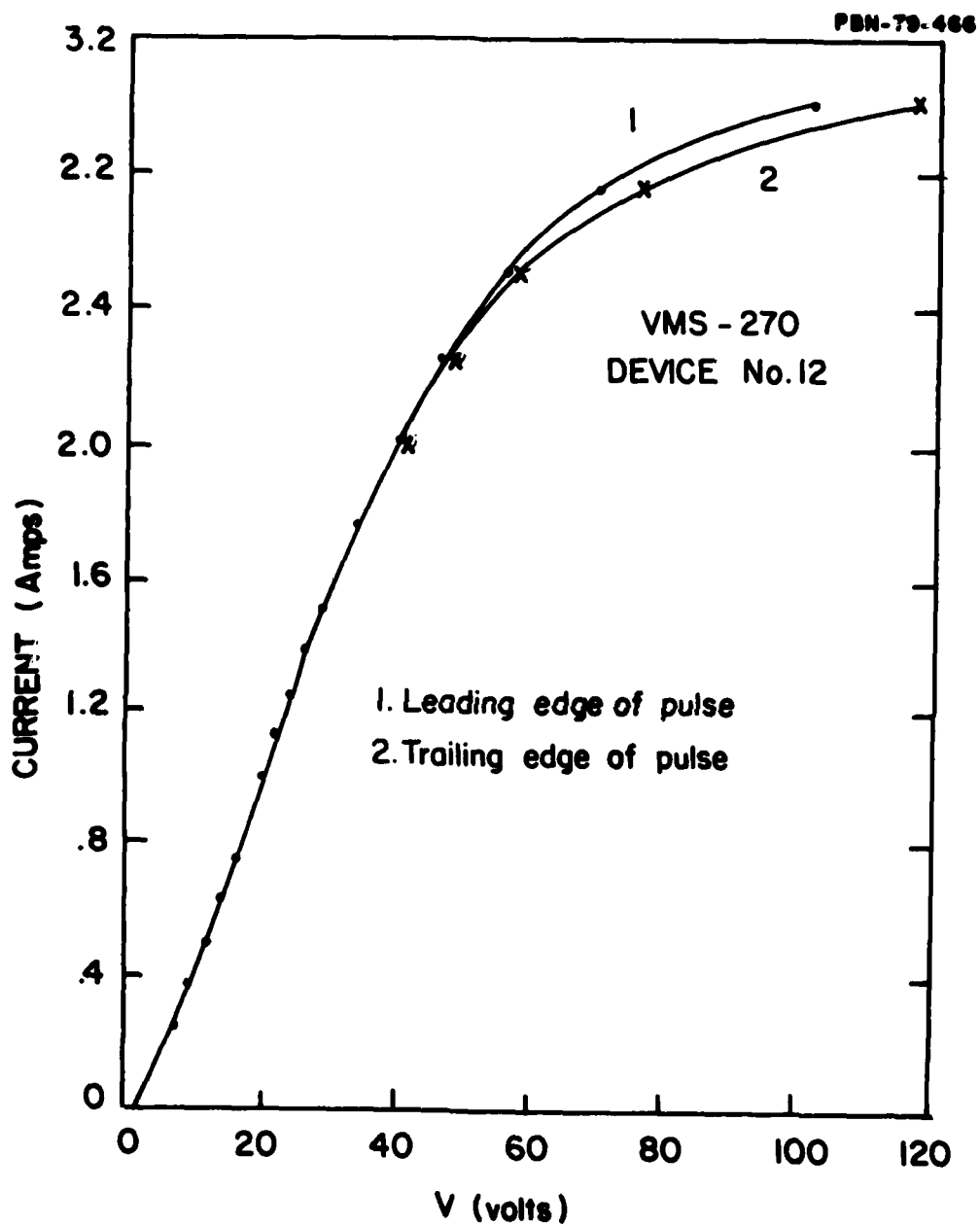


Figure 29. Variation of I-V Plots from Leading Edge to Trailing Edge of Pulse in VMS-270, Device No. 12.

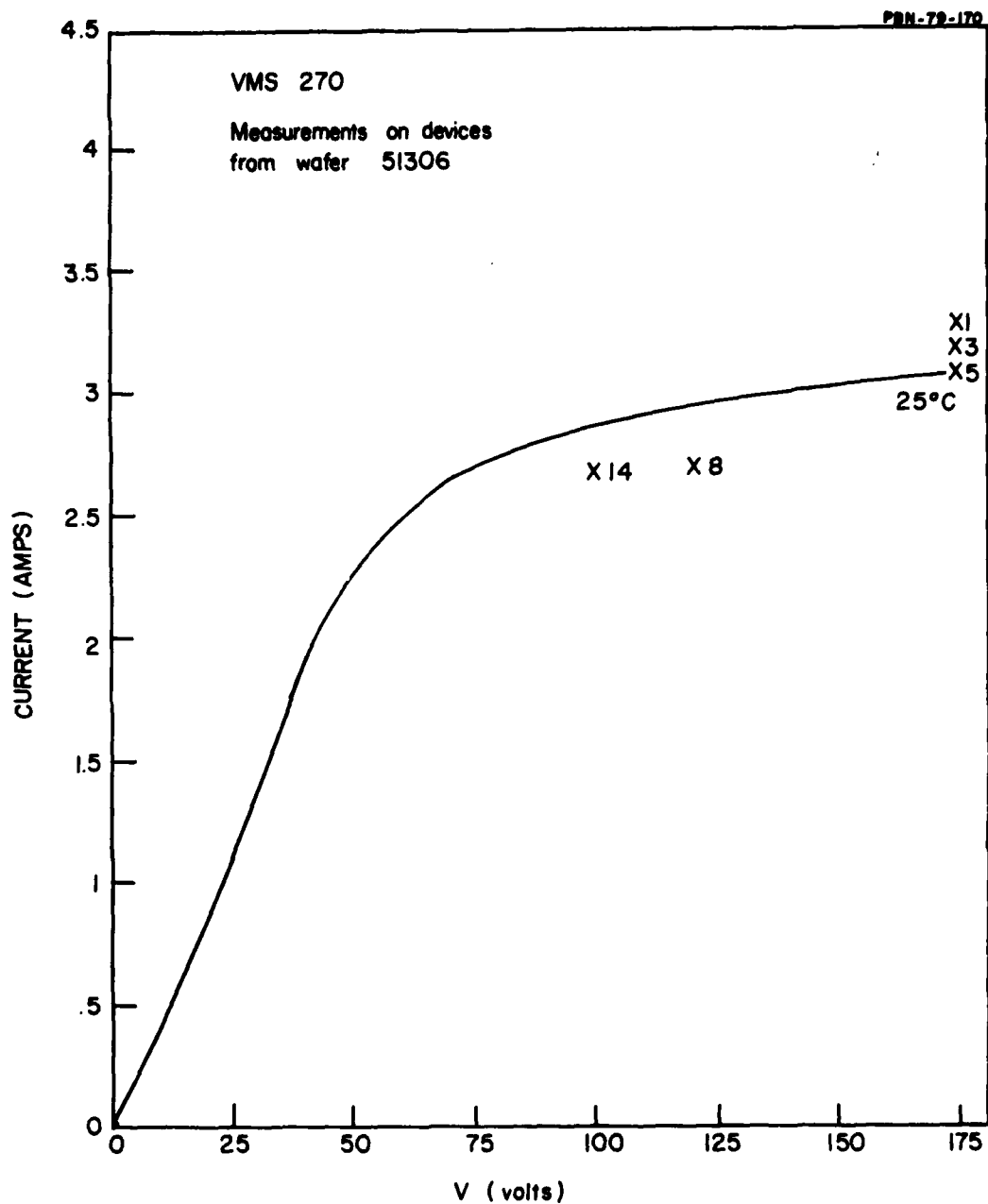


Figure 30 I-V Measurements on Five Devices from Wafer No. 51306. The solid curve was measured on the standard device No. 5. The "X's" mark the highest voltage measurement on each of the five devices.

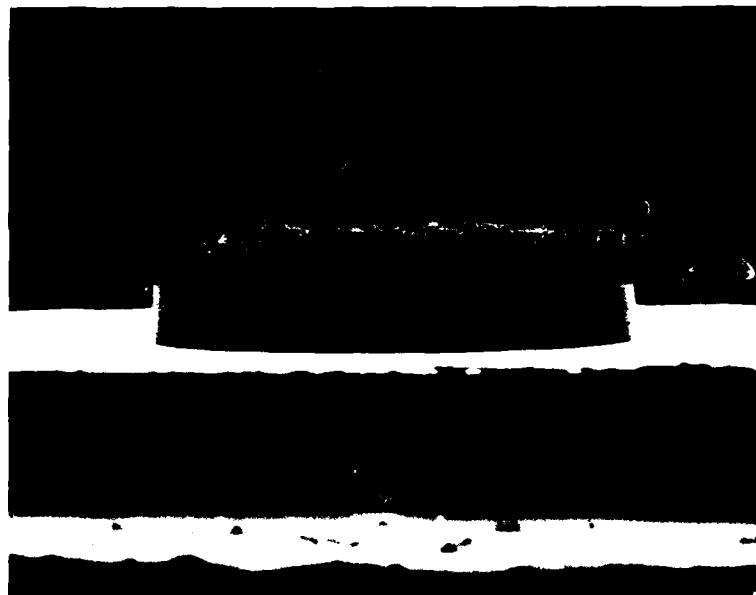


Figure 31a Sample No. 3 at 440X Magnification. The etching process reduced the area to  $2.07 \times 10^{-4} \text{cm}^2$ .

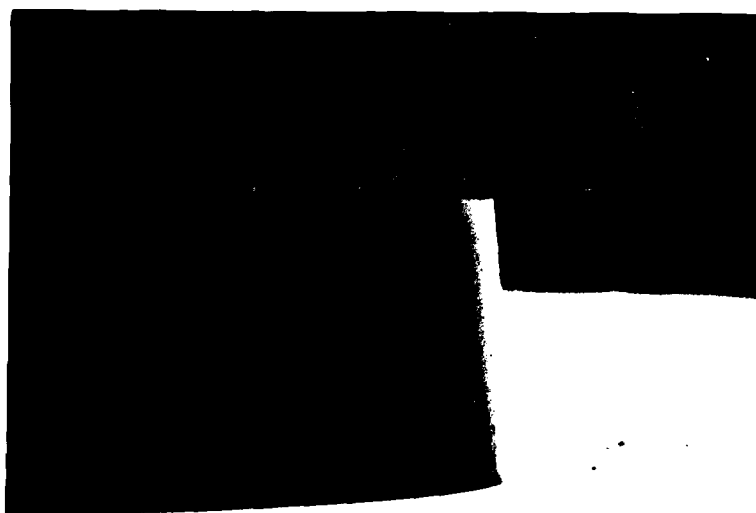


Figure 31b Sample No. 3 at 2200X Magnification. Further magnification shows that this sample is a smooth and nearly perfect right circular cylinder.

### 4.3 Data Reduction Methods

Figure 32 shows the measured I-V curves from a typical device. It is convenient to replot the curve in units of velocity and electric field. This is done by renormalizing I to  $v_{app}(\bar{E}) = I/N_A qA$ , where A is the cross section at the midpoint and  $N_A$  is the nominal doping, and renormalizing V to  $\bar{E} = V/\ell$ . For the 26°C curve in Fig. 32, this results in the solid curve in Fig. 33. The area was measured from the SEM photograph in Fig. 26 as

TABLE 9  
AREA OF DEVICE

<u>Depth, x</u> <u>(<math>\mu\text{m}</math>)</u>	<u>Diameter</u> <u>(mils)</u>	<u>Area, A(x)</u> <u><math>\text{cm}^2</math></u>
-5.3	7.70	$3.00 \times 10^{-4}$
.8	7.87	$3.15 \times 10^{-4}$
7.0	8.04	$3.28 \times 10^{-4}$
13.0	8.35	$3.54 \times 10^{-4}$
19.2	8.55	$3.71 \times 10^{-4}$

where the active layer begins at  $x = 0$ .

The values for  $A(x)$  at the selected points are entered as tabular data in our computer program and interpreted by a spline routine. The acceptor doping  $N_A(x)$  is determined as described in Sec. 2.5 and also entered into a spline routine if it is not constant.

In order to run the computer program written to analyze this data, it is necessary to assume a velocity-field characteristic. This is the tedious part of the data analysis since we do not know this function beforehand. Tabular values for  $v_p(E)$  are assumed, entered into a spline routine and an I-V curve is calculated. The calculated curve is compared with the measured curve and new values of  $v_p(E)$  are assumed. After several iterations, a  $v_p(E)$  is found for which the calculated I-V curve is virtually identical with the measured I(V).



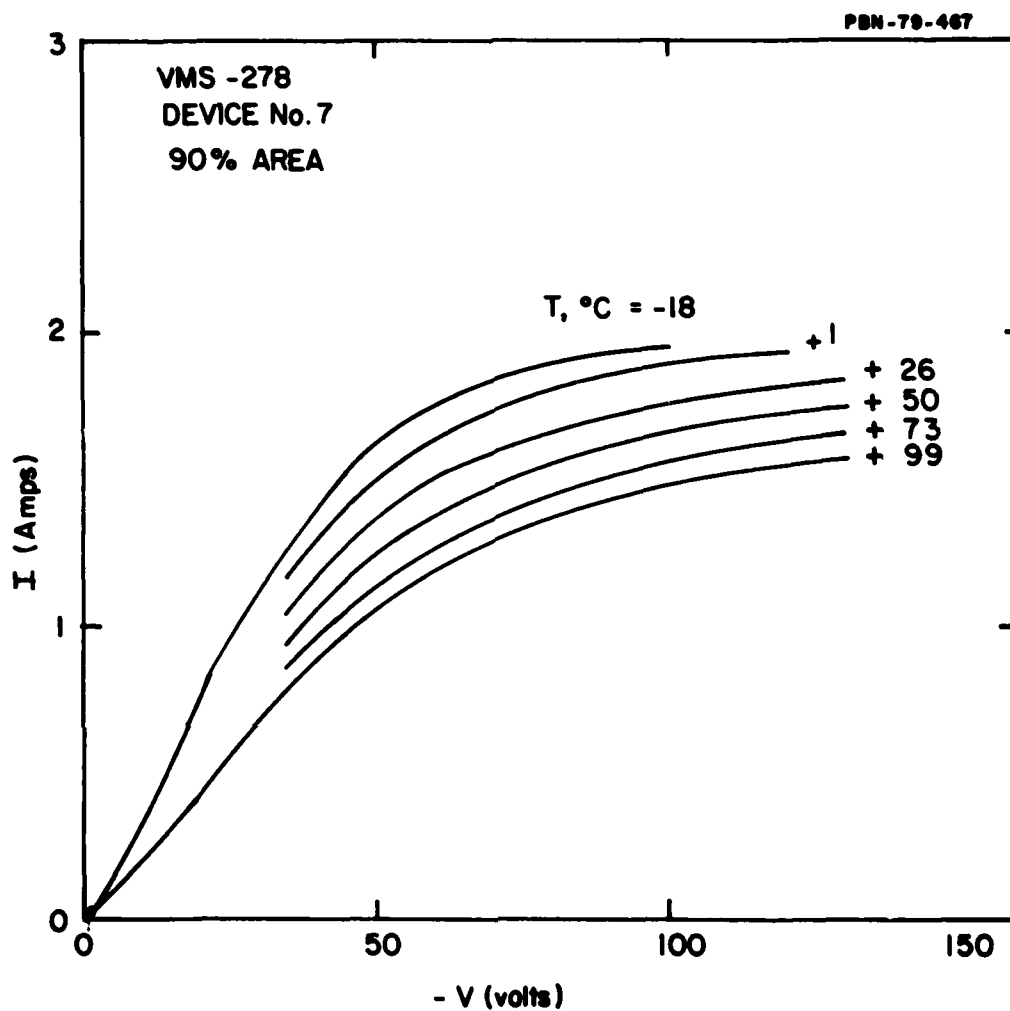


Figure 32. *I-V* Curves. This experimental data was measured on Device No. 7 at the indicated temperatures.

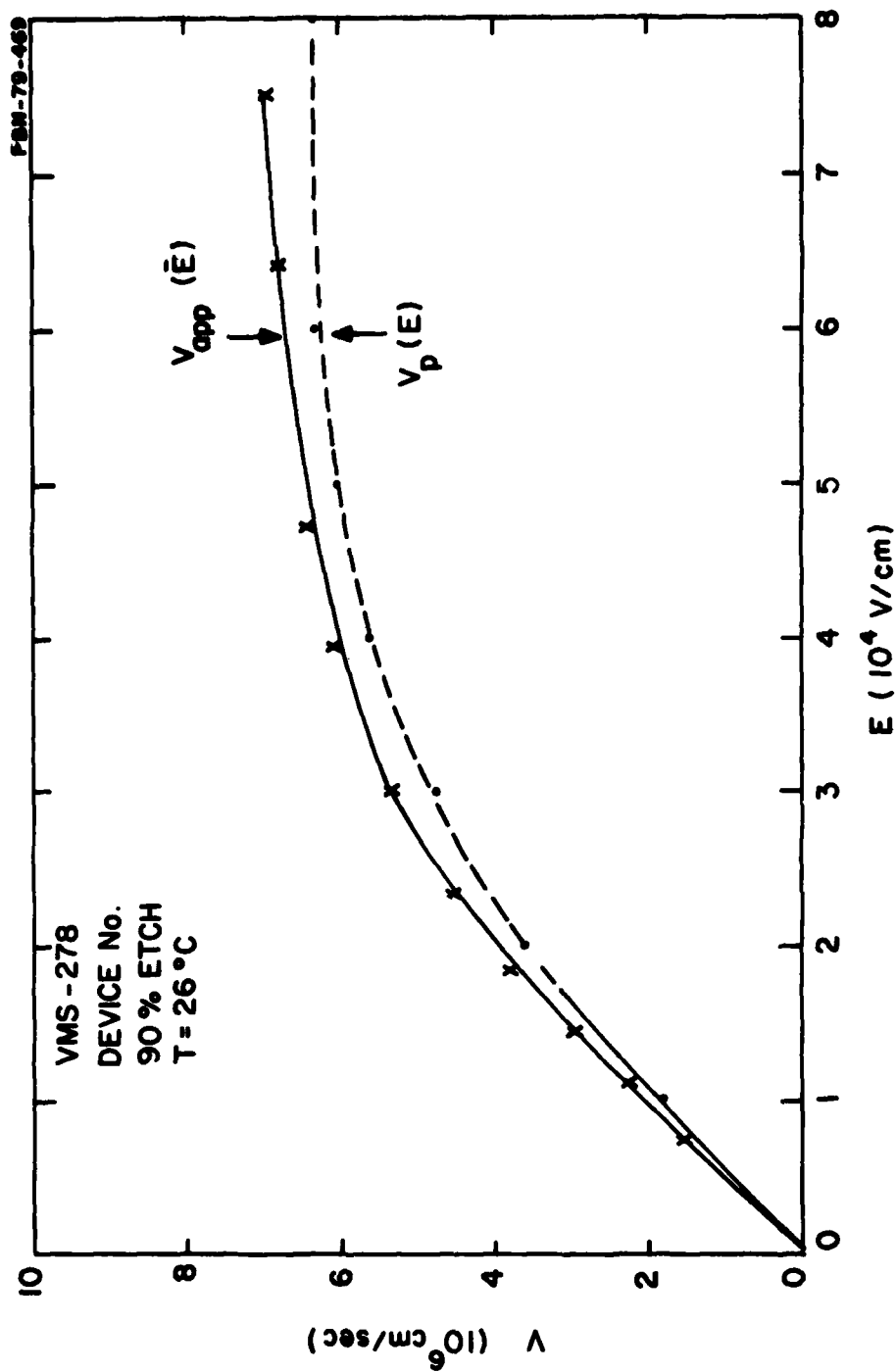


Figure 33. The Solid Curve is the Measured I-V Curve Renormalized to  $V_{app}$  and  $\bar{E}$ .  
The dashed curve is the  $V_p(E)$  curve which gives the calculated values  
of I-V indicated by the crosses.

For this example, Fig. 33 shows that the true  $v_p(E)$  is not radically different from the  $v_{app}(\bar{E})$ , that is, from the renormalized  $I(V)$  curve. However, a detailed inspection of the computer solution for the electric field shows that the field is not constant, as it is in the case illustrated by Fig. 24, but it varies due to the increase in the acceptor doping near the semi-insulating substrate, as shown in Fig. 34.

Similar techniques were used to reduce the measured data for other velocity measurement devices. For example, Fig. 35 shows the hole velocity characteristic (solid curve) which can be used to calculate the dotted curve which is coincident with the dashed curve measured on the unetched device No. 6 from wafer 51310.

#### 4.4 Results

The saturated hole velocity measured in these experiments has been consistently below the values by Dalal (1970, 1971). For a series of four devices from wafer 51310, described in Table X, the saturated hole velocity fell within a range of  $6.0$  to  $8.1 \times 10^6$  cm/sec. The saturated velocity is therefore taken as

$$v_{psat} = 7 \pm 1 \times 10^6 \text{ cm/sec} \quad (3)$$

The velocity versus field characteristic is plotted for three different temperatures in Fig. 36. These curves were obtained from device 7 of wafer 51310, using the experimental  $I-V$  curves in Fig. 32. This wafer had an active layer with a nominal doping of  $5 \times 10^{15}$ . The mobility in the linear range of the velocity field characteristic was  $190 \text{ cm}^2/\text{volt-sec}$  at room temperature and dropped to  $165 \text{ cm}^2/\text{volt-sec}$  at  $99^\circ\text{C}$ .

The velocity versus field characteristic measured on Device 3 from Wafer 51306 was slightly lower than the velocity measured on Device 7 from Wafer 51310, with a saturated velocity at room temperature of  $5.6 \times 10^6$  cm/sec. This wafer had a nominal doping of  $2 \times 10^{16}$  cm<sup>-3</sup> which dropped to  $1 \times 10^{16}$  cm<sup>-3</sup> at the narrow end. The low doping at the narrow end acts to sharply reduce the current under saturated velocity conditions. The mobility at room temperature was 176 cm<sup>2</sup>/volt-sec.

The saturated velocities as a function of temperature as measured on the two wafers are shown in Fig. 37. The variations in the measured saturation velocities between the two wafers is consistent with the estimated experimental error and not necessarily due to the higher doping level in Wafer 51306.

On the basis of the four measurements described in Table 10 for reduced area samples from Wafer 51310, and the single measurement from Wafer 51306, the average saturated hole velocity and rms error are  $(6.6 \pm .9) \times 10^6$  cm/sec.

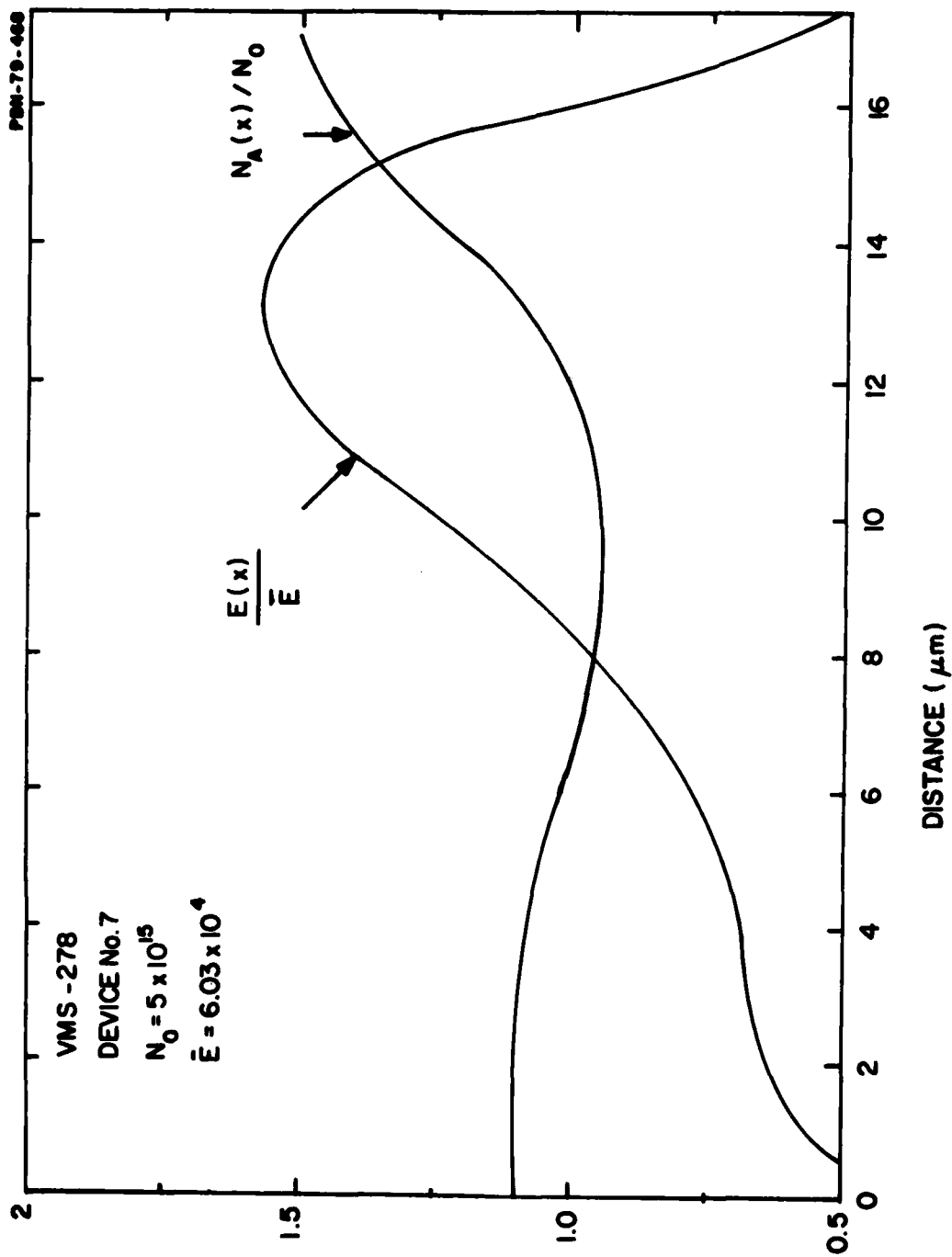


Figure 34. Change of Electric Field Due to the Changing Cross Section and Doping Nonuniformity in Device No. 7.

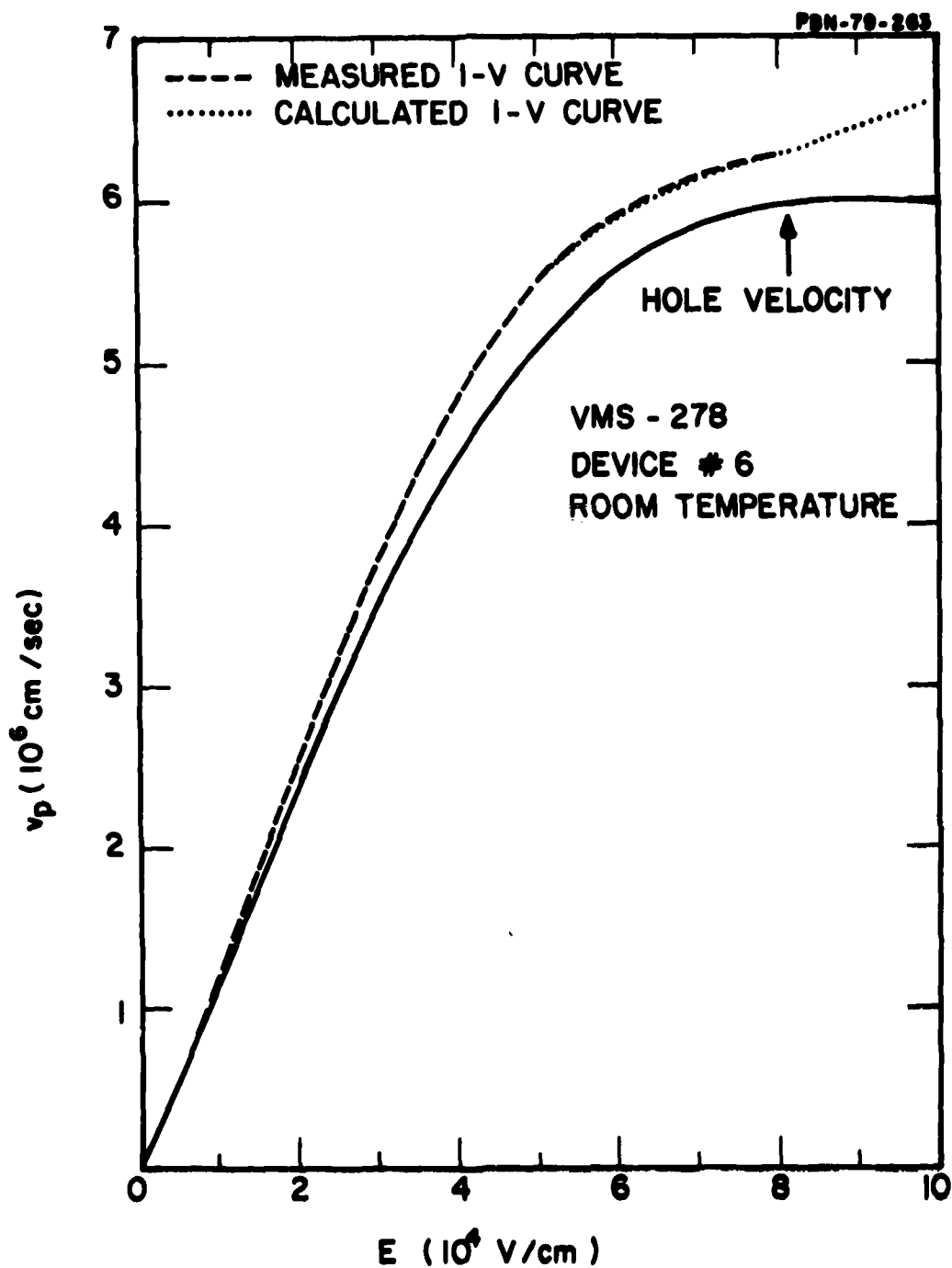


Figure 35 The Solid Curve is the  $v(E)$  Curve, which has been used to Calculate the Dotted Curve, which is Normalized Version of the Expected I-V Curve. This curve is essentially coincident with the dashed curve, which is the renormalized form of the I-V curve.

TABLE 10

PARAMETERS FOR ETCHED VMS 278

Device No.	Nominal Area <sup>‡</sup>	Active Area cm <sup>2</sup>	I <sub>sat</sub> * A	$\frac{I_{sat}}{N_D q A}$ ** cm/sec	v <sub>p</sub> † cm/sec
6	100	$3.15 \times 10^{-4}$	†† 1.9	$7.5 \times 10^6$	$6 \times 10^6$
7	90	$3.00 \times 10^{-4}$	†† 1.88	$7.8 \times 10^6$	$6.4 \times 10^6$
2	70	$2.36 \times 10^{-4}$	1.65	$8.7 \times 10^6$	$8.1 \times 10^6$
3	50	$2.07 \times 10^{-4}$	1.25	$7.6 \times 10^6$	$6.9 \times 10^6$
3†††	100	$3.23 \times 10^{-4}$	2.8	$2.7 \times 10^6$	$5.6 \times 10^6$

\* I<sub>sat</sub> is actually the current measured at 150 volts. Even with a completely saturated hole-velocity characteristic, the calculated I<sub>sat</sub> has a slight positive slope due to increasing space charge.

\*\* This value is a nominal value for v<sub>p</sub> neglecting space charge area variations and doping variations, and using a nominal doping level.

† Computer calculated results include area and doping variations as well as space charge effects.

†† Minimum area.

††† Wafer 51306. All other entries are from Wafer 51310. Nominal doping is taken as  $2 \times 10^{16}$  cm<sup>-3</sup> for Wafer 51306 and  $5 \times 10^{15}$  cm<sup>-3</sup> for Wafer 51310.

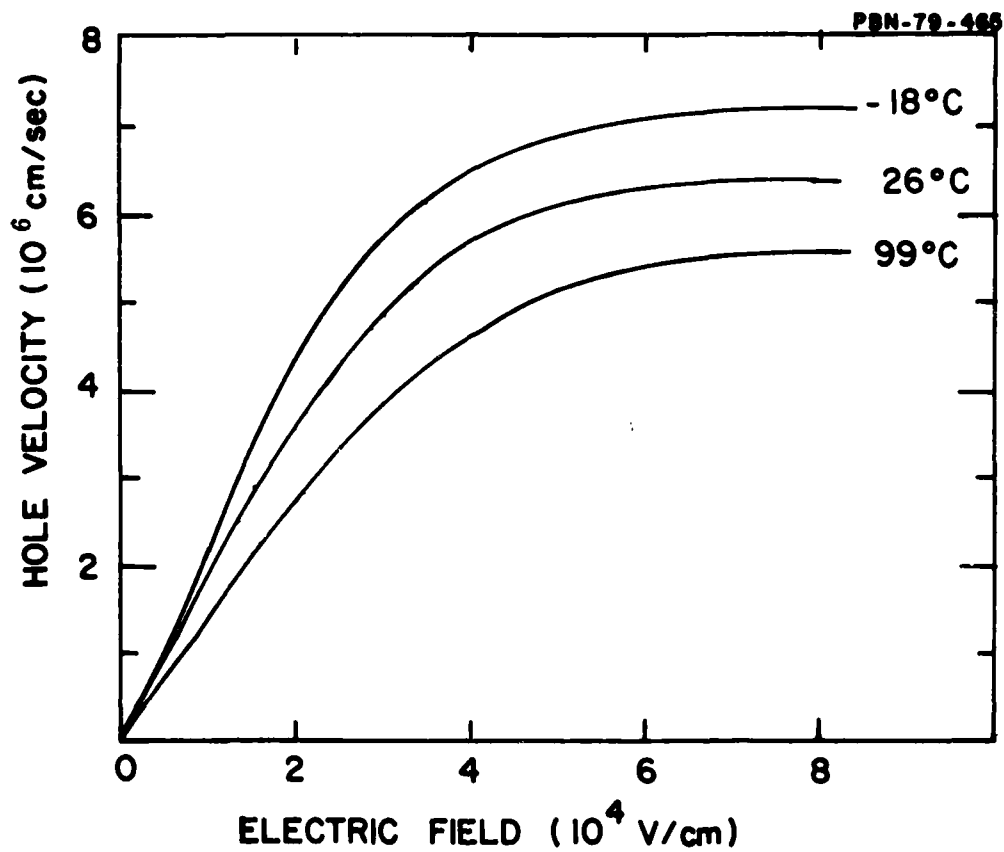


Figure 36. Velocity-Field Characteristics for  $T = -18^\circ\text{C}$ ,  $26^\circ\text{C}$  and  $99^\circ\text{C}$ . The data was taken on Device No. 7 which is pictured in Fig. 26.



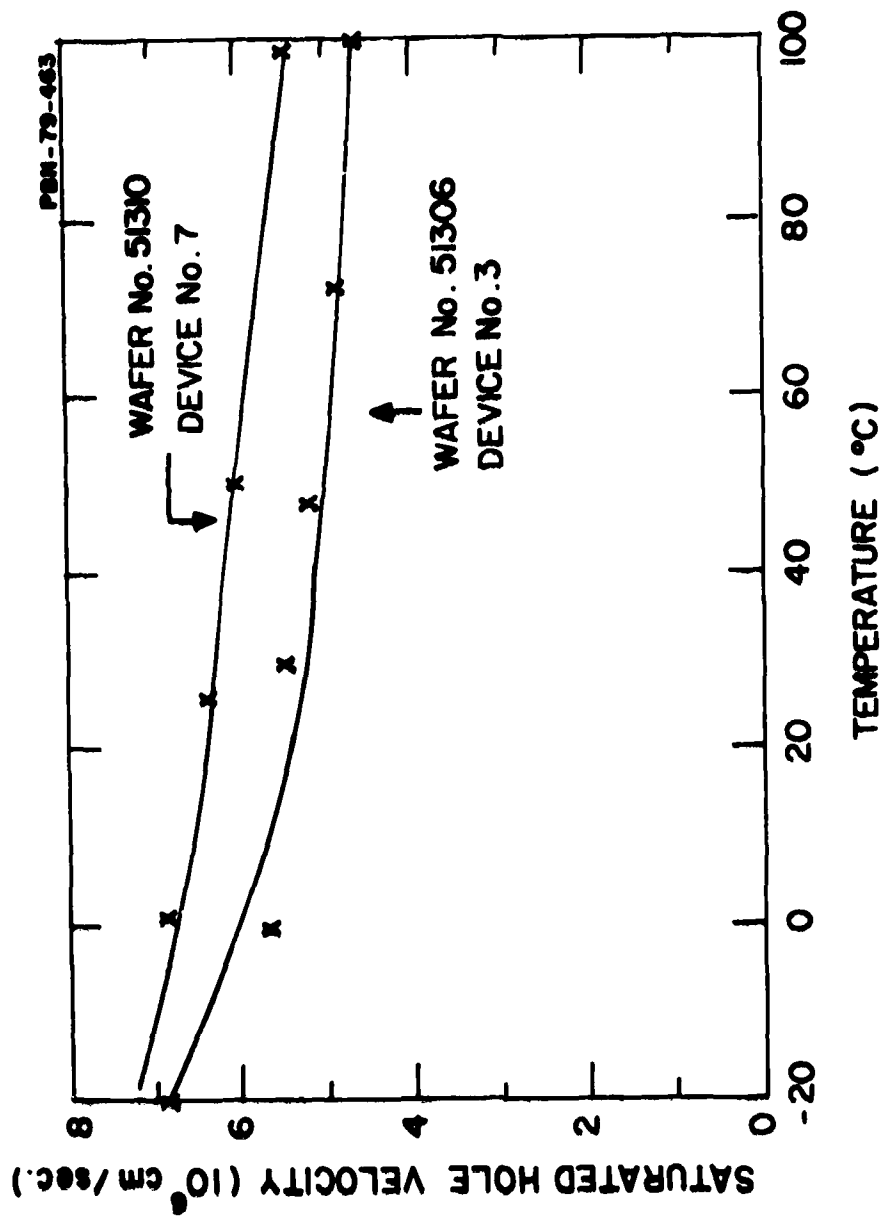


Figure 37. Saturated Hole Velocities as a Function of Temperature from Wafer No. 51306 and No. 51310.

AD-A079 980

RAYTHEON CO WALTHAM MASS RESEARCH DIV  
P-TYPE GALLIUM ARSENIDE EPITAXIAL GROWTH. (U)  
AUG 79 S R STEEL, K K JOHNSON

F/G 20/12

UNCLASSIFIED

S-2559

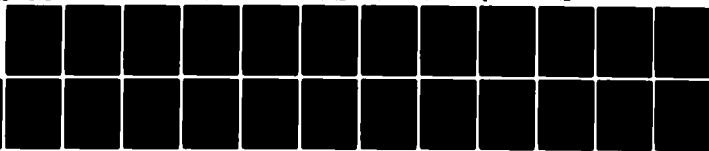
AFAL -TR-79-1144

F33615-78-C-1456

NL

2 of 2

AD  
NOV 79 1610



END  
DATE  
FILMED  
2-80

001

#### 4.5 Discussion of the Results

The measurement of hole velocity as a function of field agreed with the earlier measurements of Dalal (1970, 1971) by showing a linear mobility range for fields below  $2 \times 10^4$  V/cm, and a saturated velocity for fields above  $6 \times 10^4$  V/cm. However, the magnitude of the saturated hole velocity, as indicated by our measurements, was consistently below the magnitude reported by Dalal.

The cumulative experimental error in these measurements is estimated to be on the order of 20 percent. First, the scanning electron microscope measurements of the geometry are estimated to have a 5 percent error in linear dimensions, giving a 10 percent error in the cross sectional area. The acceptor doping densities are inversely proportional to the square of the area of the Schottky diode used in the C-V measurements. In our measurements, a standard diode area is laid down which has been carefully calibrated over many measurements, as discussed in the section on characterization. Nevertheless, the error in the doping density may be on the order of 10 percent. The experimental error in reading the current produced by the pulse generator is also estimated to be about 10 percent.

Devices on which successful measurements were made showed almost the same  $I(V)$  curves with both polarities. For example, Fig. 38 shows the results for the two polarities for device No. 6 from lot VMS-278.

The  $I(V)$  characteristics in the devices used in our measurements are nearly symmetric with respect to polarity, as shown by bias voltages on the order of 100 volts (Fig. 38) and low voltage measurements. These results indicate that any nonohmic effects at the  $p^+$  contacts produce voltages which are negligible compared to the 100-150 volts at which the saturated velocities are measured. From our measurements of the high levels of the doping density at the  $p^+$  contacts we would expect any series resistance to be negligible, but do not have an independent verification from the electrical measurements.

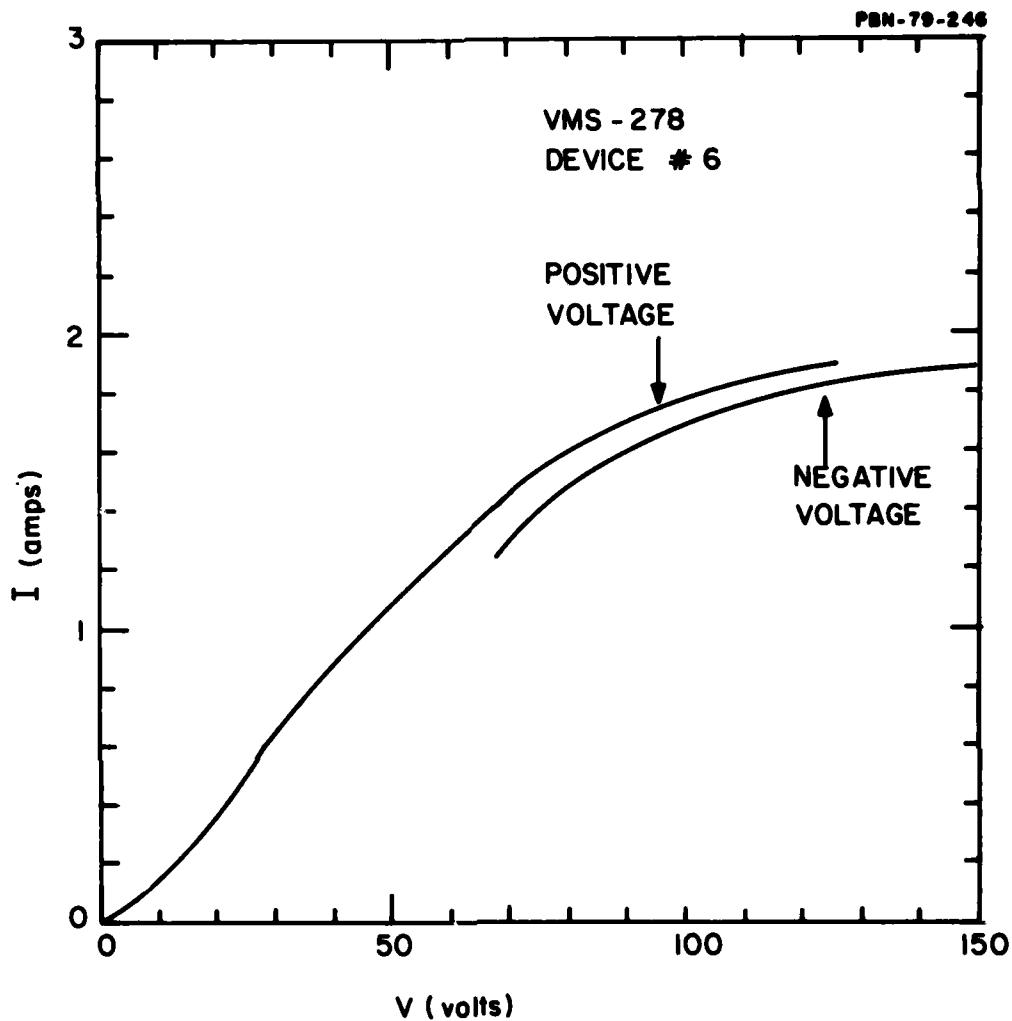


Figure 38 *I-V Curve from a Device with a Nominal Doping of  $5 \times 10^{15} \text{ cm}^{-3}$ . There is only a small difference between the current observed when the polarity is reversed, indicating that the saturated velocity can be measured consistently.*

However, it should be pointed out that such a series resistance would not affect the measured value of the saturated velocity, even though it might cause an erroneous lowering in the measured value of the mobility.

The measurements described in this section therefore indicate that the saturated hole velocity at room temperature in GaAs is approximately  $7 \times 10^6$  cm/sec. This is closer to the saturated electron velocity of  $7.3 \times 10^6$  cm/sec measured by Houston and Evans (1977) than it is to the saturated hole velocity measured by Dalal (1971).

As a check on the saturated hole velocity, the space charge resistance was measured on device No. 9 of VMS-419. This device was fabricated from wafer No. 51165, whose profile is shown in Fig. 39. The diameter of the device was found to be 0.00729 inches by matching the density found on a C-V measurement on the device with the profile in Fig. 39, which had been determined from C-V data taken on the original wafer. In this device, the depletion region is confined at  $x = 0$  by a large n-spike while the depletion region extends across a p-drift region with doping levels on the order of  $3 \times 10^{15}$  cm<sup>-3</sup>. The approximate thickness of the avalanche region is  $W_A = 0.42$   $\mu$ m and the total depletion region thickness is approximately  $W = 3.05$   $\mu$ m, as shown in Fig. 39. The measured value of  $R = 15$  ohms should be approximately equal to

$$R = \frac{1}{2} \frac{(W - W_A)^2}{\epsilon A v_{psat}} \quad (4)$$

This gives a value  $v_{psat} = 7.7 \times 10^6$  cm/sec, where the measurement was made at a diode temperature of approximately 95°C. A comparison with Fig. 37 shows that this value is higher than our earlier measurement on device No. 7 by about  $2 \times 10^6$  cm/sec. The experimental error in this measurement, which involves the area of the device, the area of the mesa used to determine the doping density, the estimate of the avalanche zone thickness and the space charge resistance measurement is on the order of 20 percent.

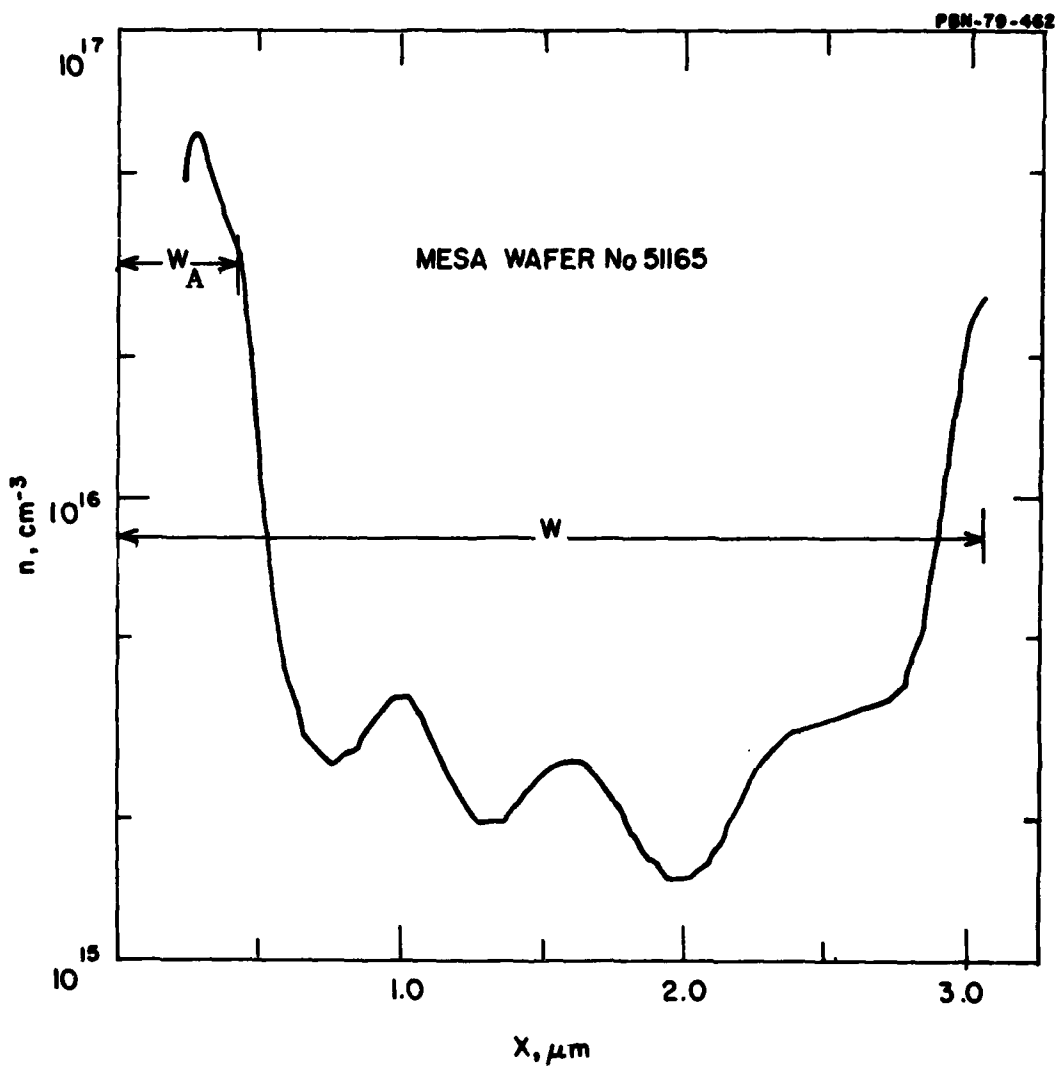


Figure 39. Profile of Doping Density vs. Distance for Wafer No. 51165.  $W_A$  is the approximate extent of the avalanche zone and  $W$  the distance from the n-spike to the end of the drift region.

## SECTION V

### IONIZATION COEFFICIENTS IN GaAs

#### 5.1 Introduction

The avalanche zones of high efficiency IMPATT diodes frequently have dc breakdown fields in the neighborhood of  $6 \times 10^5$  V/cm and can reach considerably higher fields during their oscillations. With the exception of recent measurements by Ito et al (1978), previous measurements were all below  $5 \times 10^5$  V/cm. For example, the well known experiments by Stillman et al., (1974) were carried out below about  $3 \times 10^5$  V/cm. Measurements were taken in this contract with breakdown fields in excess of  $6 \times 10^5$  V/cm, and over a range of temperatures.

The results described in this section were all derived from breakdown voltages of diodes made from wafers grown in our laboratory. The breakdown voltage measurements have an advantage over photomultiplication experiments in that they cannot be contaminated by an admixture of electron and hole current (Stillman, 1977) nor are the measurements dependent upon obtaining a very accurate value of the injected current. Moreover, a breakdown voltage is a discrete value and can be measured more accurately than multiplication factors which are continuous functions of the applied voltage. The breakdown voltage method has a disadvantage in that only one point is obtained from a given wafer at a given temperature, in contrast to the photomultiplication experiments in which a wafer yields a range of values as the photomultiplication is measured over a range of applied voltages.

The most important disadvantage of the breakdown voltage method is that our measurements give only an effective  $\alpha$ , whereas the photomultiplication experiments provide individual values of  $\alpha$  and  $\beta$ . The effective  $\alpha$  can be broken down into separate values for  $\alpha$  and  $\beta$  if we have independent knowledge of the ratio of the hole ionization coefficient to the electron ionization coefficient. We denote this ratio by  $k(E) = \beta(E)/\alpha(E)$ .

The condition for breakdown, when  $\alpha \neq \beta$ , can be written approximately as

$$\int_{-\infty}^{\infty} \alpha dx = \ln k / (k-1). \quad (1)$$

The approximation given by Eq. (1) is discussed in Holway (1976). This approximate equation is exact under two circumstances: (1) when  $k$  is a constant independent of  $E$ , and (2) for a Read diode or a PIN diode in which the field is constant over the ionization region. Because our measurements are made with Read profiles, the second condition holds to a good approximation. Therefore we define the effective  $\alpha$  as

$$\alpha_{\text{eff}} = \frac{k(E)-1}{\ln k(E)} \alpha(E), \quad (2)$$

which means that, at breakdown,  $\alpha_{\text{eff}}$  satisfies the equation

$$\int_{-\infty}^{\infty} \alpha_{\text{eff}} dx = 1. \quad (3)$$

In the approximation of Eq. (3), we would miss the well known result that a  $p^+n$  diode and its complementary  $n^+p$  diode have different breakdown voltages (Urgell, 1969; Schroeder and Haddad, 1971). However, even in the case of silicon where  $\alpha$  exceeds  $\beta$  by about an order of magnitude and for flat profiles, the breakdown voltage only differed by 5 percent and the breakdown field by half that amount (Schroeder and Haddad, 1971). Therefore, in GaAs where  $\alpha$  and  $\beta$  are more nearly equal, there will be little error in assuming Eqs. (2) and (3), especially when the doping profiles approximate Read diodes.

In the limiting condition where  $k(E) \rightarrow 1$ ,  $\alpha_{\text{eff}}$  approaches  $\alpha = \beta$ . As a consequence, the results given by those experimenters who assumes  $\alpha = \beta$ , such as Hall and Leck (1968) or Salmer et al. (1973) were, in fact, measurements of  $\alpha_{\text{eff}}$ . When  $\alpha$  and  $\beta$  are given separately (Ito, et al., 1978; Stillman, 1977; Law and Lee, 1978),  $\alpha_{\text{eff}}(E)$  can be calculated from Eq. (3), which gives a convenient way of comparing results from different experiments.

One can see that this definition of  $\alpha_{\text{eff}}$  in Eq. (2) is convenient for several reasons. First, once  $\alpha_{\text{eff}}$  is known, the breakdown voltage can then be



calculated for an arbitrary doping profile by making use of Eq. (3). Secondly, by measuring the breakdown voltage and the doping profile of a wafer,  $\alpha_{\text{eff}}$  can be determined by inverting Eq. (3) using the analytical technique described in Sec. 5.3. Finally, once  $\alpha_{\text{eff}}$  is determined, one can calculate  $\alpha$  and  $\beta$  separately from Eq. (2) if their ratio  $k(E)$  is known from some independent source.

Previous experiments to measure ionization coefficients (Ito et al., 1978; Stillman, 1977; Stillman et al., 1974; Schroeder and Haddad, 1971; Law and Lee, 1978; Hall and Leck, 1968; Salmer et al., 1973) have used flat profile n-GaAs for the active layer terminated by either a  $p^+$  junction or by a Schottky barrier. In our experiments we have used Read profiles of three types: 1) double-drift structures (wafer no. 33205 and 91216); 2)  $p^+n$  structures (wafer no. 32506); and 3) an active p structure (wafer no. 51165). In order to carry out these experiments, it is necessary to determine the electric field accurately. This information is derived from mesa C-V measurements using a digital profilometer as shown in Sec. 5.3. Although this technique does not provide a doping profile within the zero bias depletion width of the junction, we will show that the uncertainty in  $\alpha$  due to this effect is no more than a few percent.

## 5.2 Measurements

The key to obtaining high field measurements of  $\alpha$  is to grow a Read-like profile in which the avalanche zone is confined to a thickness of less than 1200 angstroms. Then C-V data are obtained from a mesa-etched diode using the digital profilometer. A numerical analysis of this digital data is carried out to obtain the electric field as a function of the depletion layer width as shown in Fig. 40 for the wafers mentioned above. Outside the zero bias depletion layer, these profiles are obtained from the function  $C(V)$ , stored in the digital profilometer tape, by making use of the parametric equations.

$$E(V) = \frac{1}{\epsilon A} \left[ \int_0^{V_B} C dV - \int_0^V C dV \right], \quad (4)$$

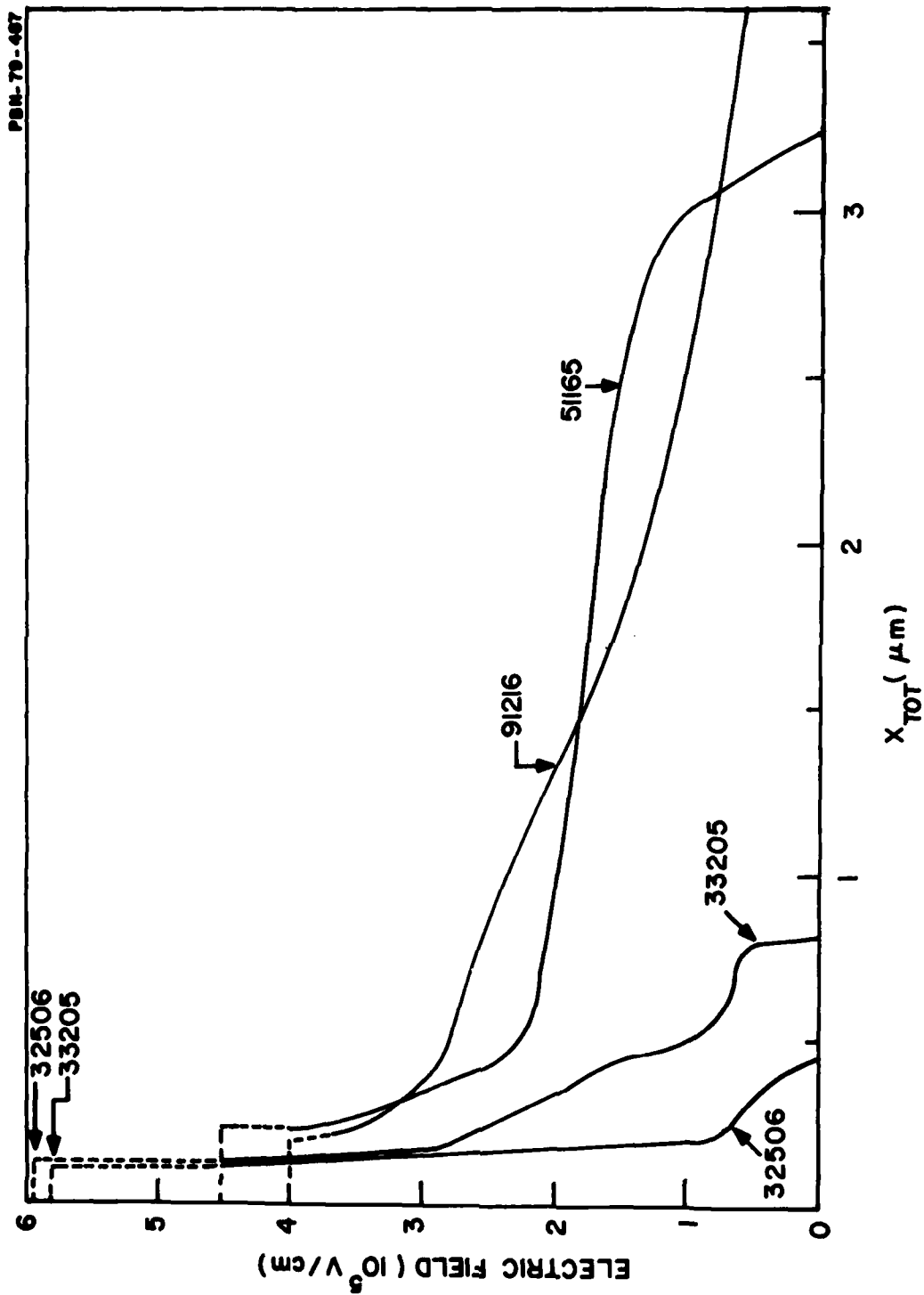


Figure 40. Electric Field vs.  $x_{tot} = x_n + x_p$  for Wafers 32506, 33205, 91216, and 51165.

and

$$x_{\text{tot}}(V) = \epsilon A / C(V). \quad (5)$$

The  $E$  vs.  $x_{\text{tot}}$  fields in Fig. 40 are plotted for breakdown fields at room temperature. The area  $A$  is the area of a standard mesa junction as laid down in preparing the sample for the digital profilometer.

The four wafers illustrated in Fig. 40 have widely differing properties. Wafer 32506 is a  $p^+n$  junction diode in which large  $n$ -spike confines the avalanche zone within  $1400 \text{ \AA}$ . Wafer 33205 is a double-drift diode with the avalanche zone confined between a  $p$ -spike and an  $n$ -spike. Wafer 91216 is a double-drift X-band wafer with the avalanche zone partially confined between two spikes. Wafer 51165 is essentially an  $n^+p$  diode where the  $n^+$  side is actually a doping spike sufficiently large to confine the depletion layer to the  $p$ -drift region.

The breakdown voltage  $V_B$  is measured independently. Figure 41 shows the measured current in mA vs. the reverse bias voltage at temperature steps of  $25^\circ\text{C}$ . The breakdown voltage is given by the nearly vertical asymptote of these curves.

### 5.3 Data Reduction

#### 5.3.1 Wafer 33205

The method used to reduce the measured data (shown in Fig. 40 and 41) to an effective coefficient will be illustrated by considering Wafer No. 33205 in detail. This wafer was grown as an experimental EHF IMPATT diode under Air Force Contract No. F33615-77-C-1186. Its reconstructed profile is shown in Fig. 42.

For a given reverse bias, one edge of the depletion layer around the junction extends a distance  $x_n$  into the  $n$ -GaAs and the other edge a distance  $x_p$  into the  $p$ -GaAs. The mesa C-V data, described in the previous section,

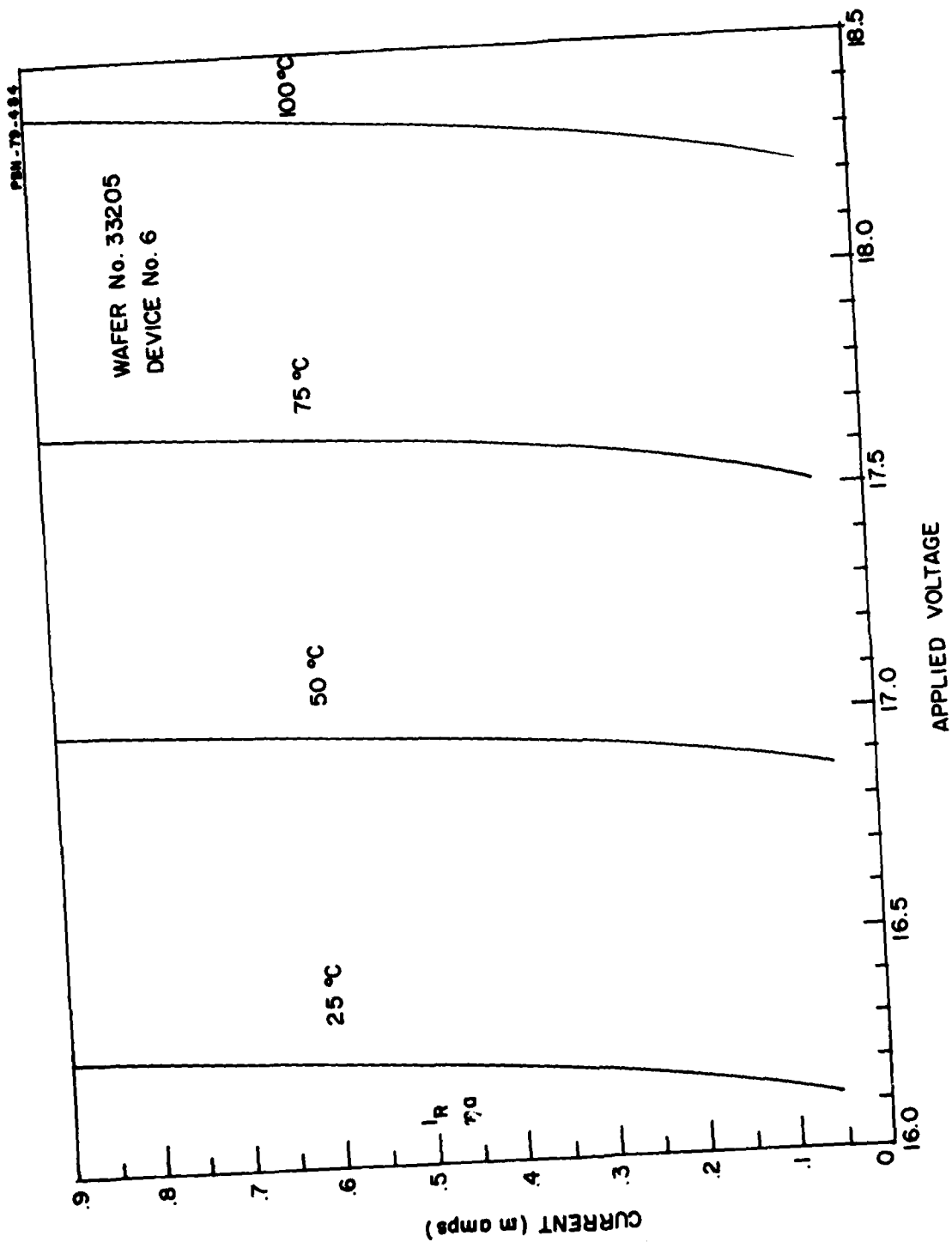


Figure 41. ' Current as a Function of Reverse Bias. The experimental results in the vicinity of breakdown are shown in steps of 25°C.

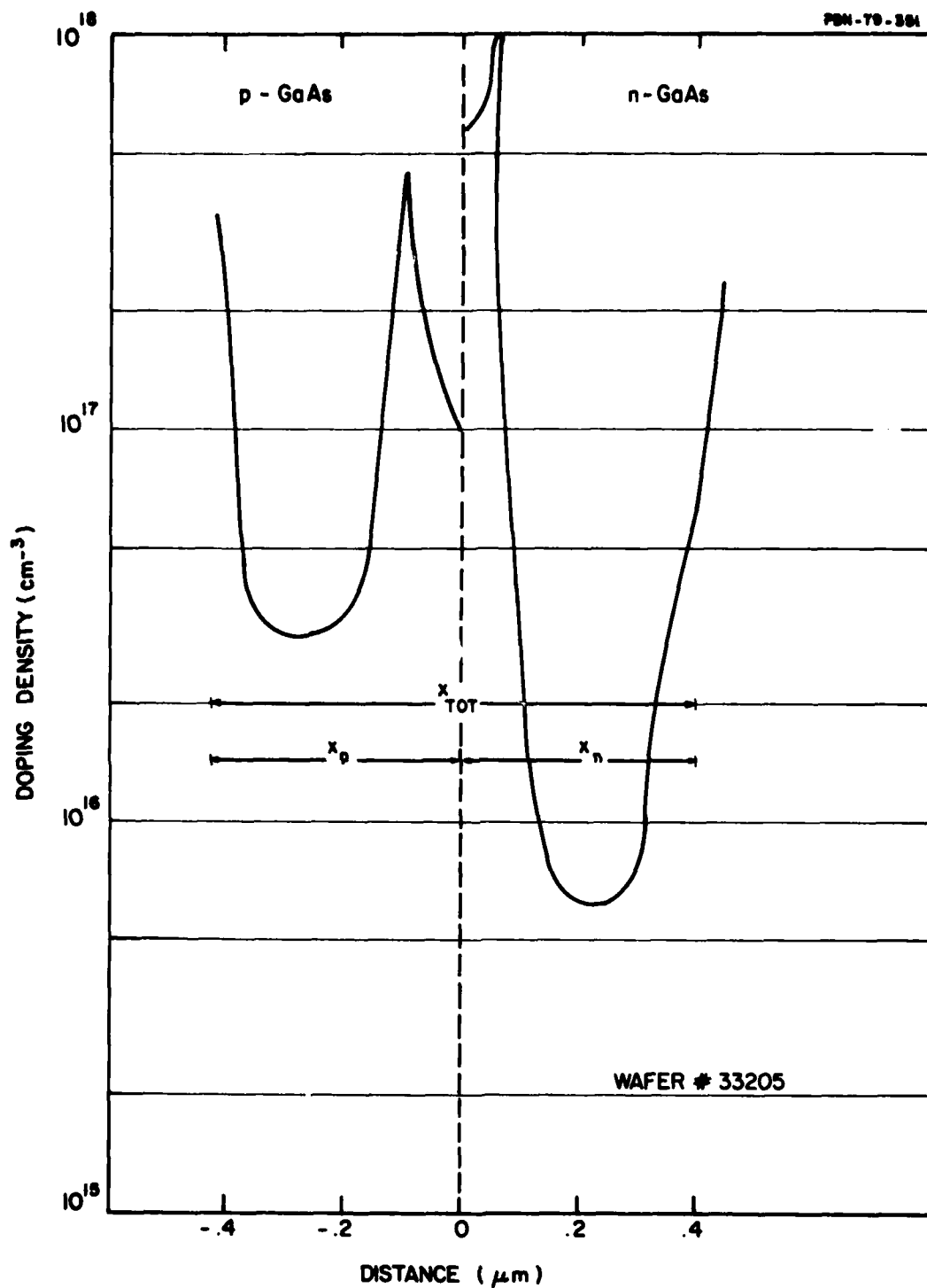


Figure 42. Plot of the Doping Profile of the Double Drift Read Wafer No. 33205, which is Used for a Determination of the Ionization Coefficient.

can measure only  $x_{\text{tot}} = x_n + x_p$ . In order to reconstruct an entire profile, it is necessary to etch away the p-GaAs and produce a Schottky barrier C-V for the n-profile close to the junction. This has been accomplished in completing the reconstruction shown in Fig. 42.

For convenience, we will use the unsubscripted notation  $w$ ,  $x$  and  $y$  in place of  $x_{\text{tot}}$ ,  $x_n$  and  $x_p$ . By integrating the doping densities in Fig. 42 and using Poisson's equation, the electric field can be plotted on each side of the junction as a function of  $x$  and  $y$ , as shown in Fig. 43. The electric field as a function of  $w = x + y$  can be obtained simply by adding  $x + y$  as shown in the figure where  $w$  is the same as  $x_{\text{tot}}$ ,  $x$  is the same as  $x_n$ , and  $y$  is the same as  $x_p$ . However,  $E(w)$  is also precisely defined by integrating the C-V data from the zero bias depletion edge at  $V = 0$  (where  $w = w_0$ ) to the breakdown voltage, as shown by the parametric equations (4) and (5).

By the relationship in Eq. (3), the breakdown field must satisfy the condition

$$\int_0^{y_B} \alpha(E) dy + \int_0^{x_B} \alpha(E) dx = \int_0^{w_B} \alpha(E) dw = 1, \quad (6)$$

where for simplicity we have dropped the subscript "eff" from  $\alpha_{\text{eff}}$ . It follows from Eq. (6) that we can get all the information needed for the breakdown calculations from the curve of  $E$  vs.  $w$ , and that it is not necessary to obtain Schottky data independently by etching away the p layer.

However, it would appear that we have another problem, namely that the only information we have about the field within the zero bias layer is that

$$\int_0^{x_0} (E - E_0) dx + \int_0^{y_0} (E - E_0) dy = \int_0^{w_0} (E - E_0) dw = V_{BI} \text{ volts} \quad (7)$$

where  $V_{BI} = 1.4$  volts is bandgap energy at 25°C (decreased by the energy level difference of the acceptors and the donors from the bandgap edge).  $E_0$

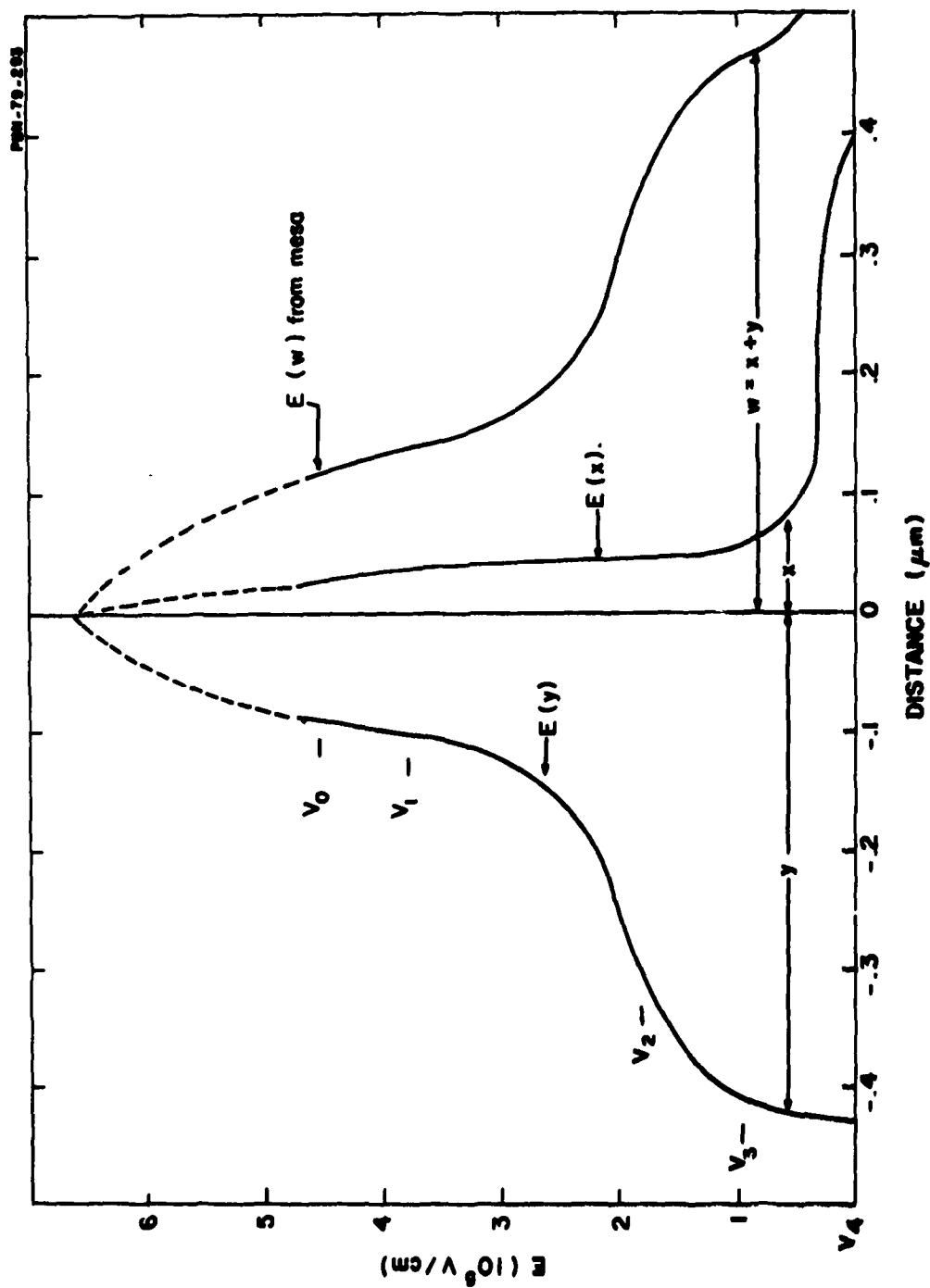


Figure 43. Breakdown Electric Field. The electric field is shown as a function of distance from the junction on both the n and the p sides, and also as a function of  $w = x_{tot}$ . Here  $V_0 = 0$  indicates the zero bias depletion layer and  $V_4$  is the room-temperature breakdown voltage.

is the field at the edge of the zero bias depletion layer. The dashed curve in Fig. 43 was obtained by assuming the  $E$  was a quadratic function of  $w$ , for  $w < w_0$  and satisfied Eq. (7). Equation (7) insures that, regardless of the functional form of  $E(w)$ , the average field, within the zero bias depletion layer will be  $E_B = E_0 + V_{BI}/w_0$ .

It is clear that the smallest possible value of  $E$  at the junction would be obtained if  $E$  were a constant for  $w < w_0$ . The field resulting from such an assumption is shown in Fig. 44. With this assumption, the junction field is lower than it was when we assumed that  $E$  was a quadratic function of  $w$ , even though the average field is still  $E_B$ .

It is convenient to picture the  $E(w)$  curve in Fig. 44 as an iceberg, that is, as a rigid curve that is lifted above the  $E = 0$  level, by applying reverse bias. If zero bias were applied, the field would sink back so that the  $E_0$  level lies at the water level (the  $E = 0$  line). The curve in Fig. 44 is pictured for an applied reverse bias of  $V_B = 16.29$  V, which according to Fig. 41 is the measured breakdown voltage at 25°C. The total voltage is the area under the curve, which equals  $V_B$  plus the built-in voltage,  $V_{BI}$ , which is the area between  $E_0$  and the curve  $E(w)$ . For breakdown at 100°C, the applied voltage must be increased to 18.44 volts and the iceberg is raised up so the line marked 100°C reaches the water level.

Although a constant value of  $E$  for  $w < w_0$  appears to be artificial, it should be a fairly good approximation for our Read diode wafers, which were grown to confine the avalanche zone between doping spikes. The field in this region would be  $E_B = E_0 + V_{BI}/w_0$ , where  $V_{BI}$  is the built-in voltage at the junction.

However, it is not necessary to rely upon the argument that the field is constant in the region near the junction. Assume for the moment that the region for  $w < w_0$  is uniformly doped on both sides of the junction. In this case, the field varies linearly for  $w < w_0$  as shown in Eq. (8) and Fig. 45(a).



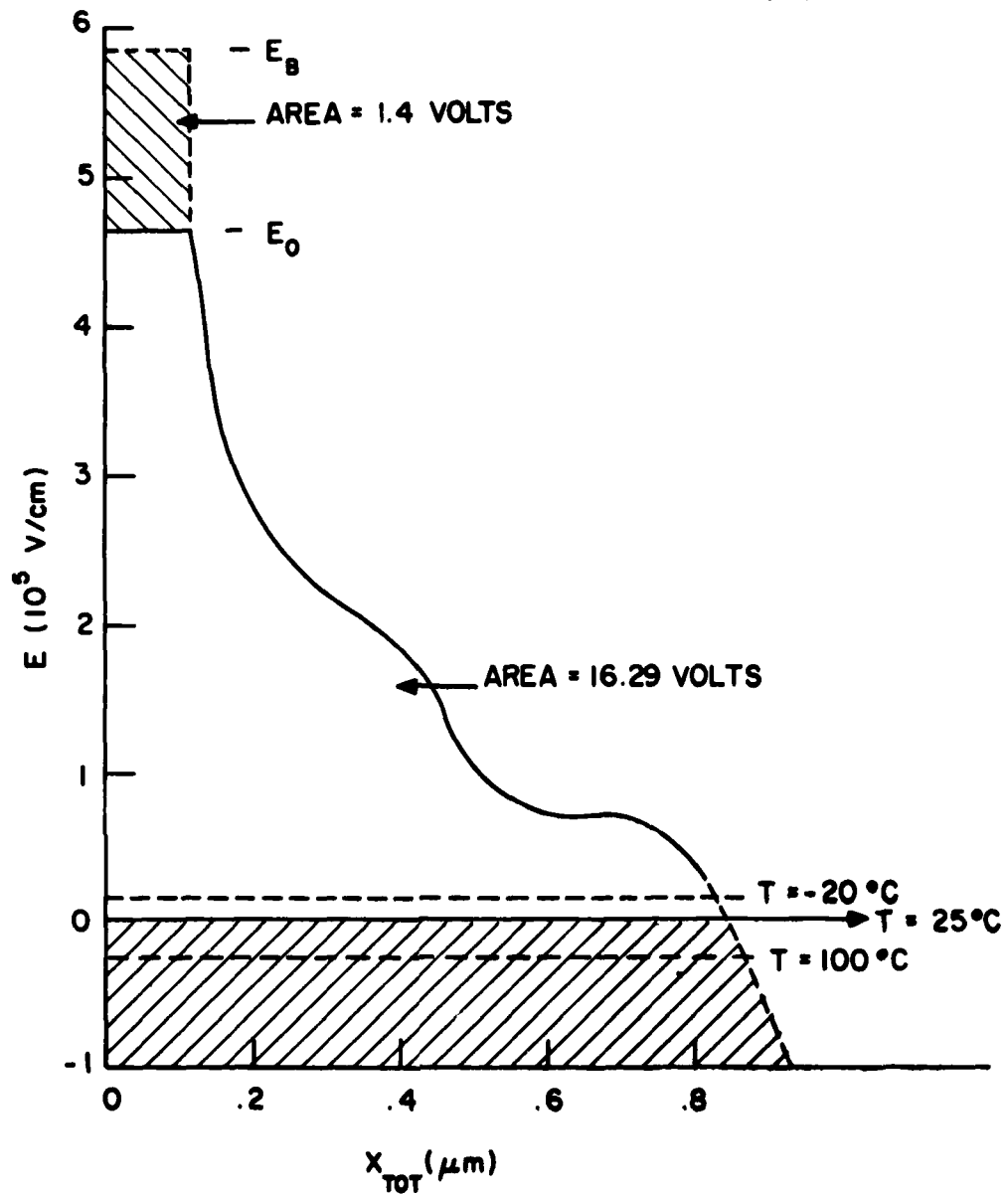


Figure 44. Plot of the Electric Field vs.  $x_{tot}$ . Here  $x_{tot}$  is the distance from the point on the n-side at which the field has the magnitude  $E$  to the point on the p-side which has the same field. The curve moves upward rigidly as the reverse bias increases, so that the area between  $E_0$  and the  $x_{tot}$  axis equals the applied voltage. The curve is drawn so that this area equals 16.29 volts, the breakdown voltage is  $25^\circ\text{C}$ .

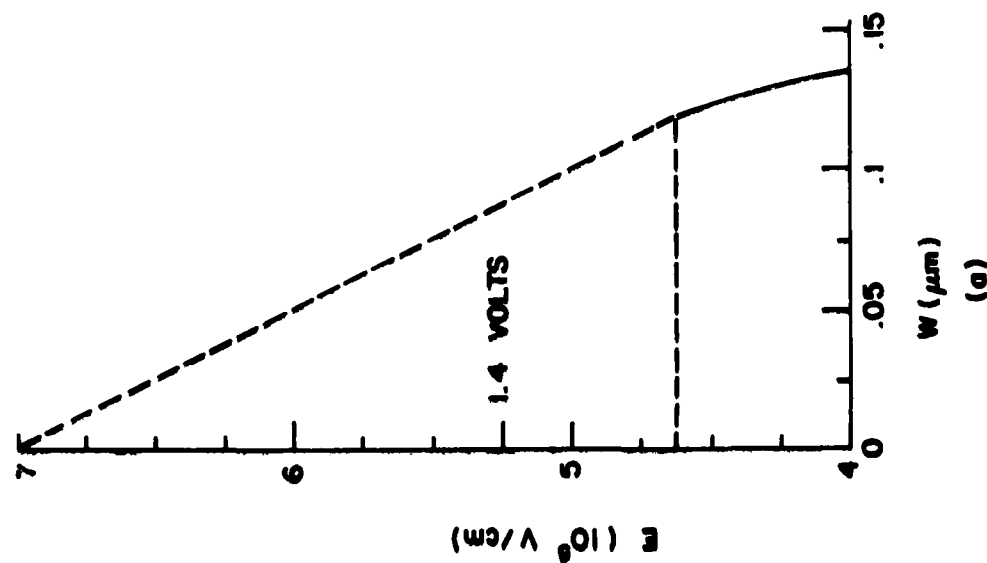


Figure 45(a). Triangular Field Within the Zero-Bias Depletion Zone. Since only the area,  $V_{BI} = 1.4$  volts, is known, this distribution is a possible alternative to the rectangular field in Fig. 44, and in Fig. 45(b).

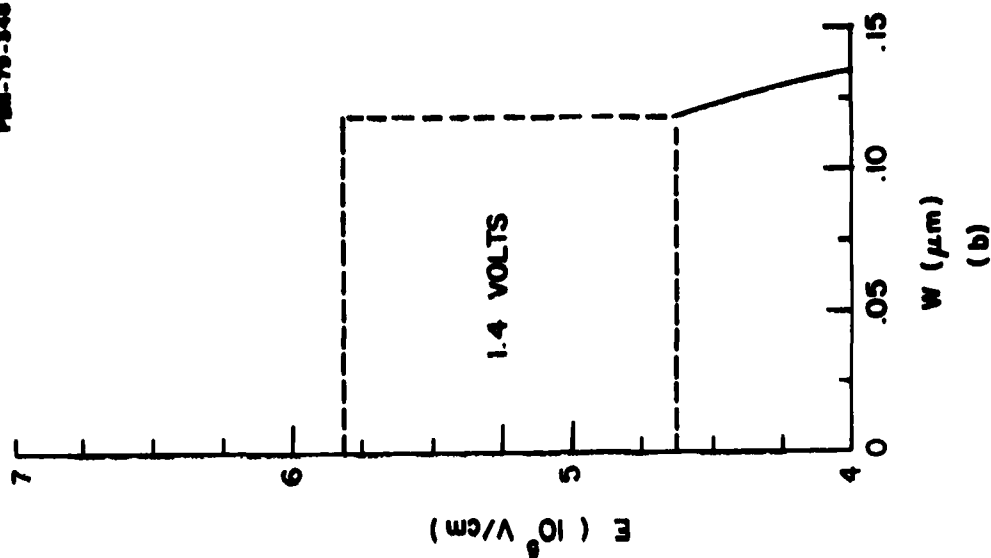


Figure 45(b). The Rectangular Field. Because of the process used in growth, this field is more likely than the triangular field. In any case, analysis shows that the area restriction implies a negligible difference in the calculated ionization coefficient at the field  $E_B$ .

$$E = E_0 + \left( \frac{2V_{BI}}{w_0} \right) \left( 1 - \frac{w}{w_0} \right) \quad (8)$$

At first sight, this would appear to be an extreme case, as can be seen by comparing Fig. 45(a), with Fig. 45(b), since the field at the junction in Fig. 45(a) exceeds its previous value by  $V_{BI}/w_0$ , which amounts to  $1.19 \times 10^5$  V/cm for this wafer. Of course, we would be prepared to argue that Fig. 45(b) is a much more accurate representation of wafer no. 33205 since it was intentionally grown to have most of the doping in spikes near the edge of the zero bias depletion layer and, in any case, compensation would tend to keep the doping levels low in the immediate vicinity of the junction. Fortunately it is not necessary to rely upon these arguments because we can show that, even if we take the extreme profile in Eq. (8), there is virtually no effect on our determination of  $\alpha(E_B)$ .

To show this, we expand  $\alpha$  in a Taylor series about  $E_B$ , i.e.,

$$\alpha(E) = \alpha(E_B) + (E-E_B) \alpha' + \frac{1}{2} (E-E_B)^2 \alpha'' + \dots \quad (9)$$

Since  $\alpha(E)$  is a function of  $E$ , its integral has the same property as Eq. (6), i.e.,

$$\int_0^{x_0} \alpha \, dx + \int_0^{y_0} \alpha \, dy = \int_0^{w_0} \alpha(E) \, dw \quad (10)$$

Therefore, regardless of the form for  $E$  when  $w < w_0$ , the integral of  $\alpha$  becomes

$$\int_0^{w_0} \alpha \, dw = \alpha(E_B) w_0 + (\alpha''/2) \int_0^{w_0} (E-E_B)^2 \, dw + \dots, \quad (11)$$

where we have substituted Eq. (9) into Eq. (10), and the term involving  $\alpha'$  has vanished since  $\int_0^{w_0} (E-E_B) \, dw = 0$  according to Eq. (7), regardless of the functional form of  $E(w)$ .

For the extreme profile described by Eq. (8) and shown in Fig. 45(a), Eq. (11) becomes

$$\int_0^{w_0} \alpha dw = \alpha(E_B) w_0 + \left(\frac{1}{6}\right) \alpha''(E_B) V_{BI}^2 / w_0 \quad (12)$$

In general, this correction is very small, as we can show by assuming this exponential form

$$\alpha = a \exp [-(b/E)^2] \quad (13)$$

for which

$$\alpha'' = 2(b^2/E^4) [2(b/E)^2 - 3] \alpha(E) \quad (14)$$

Evaluating this with Salmer's (1973) values ( $a = 1.18 \times 10^5$  and  $b = 5.55 \times 10^5$ ), and noting that at room temperature breakdown in wafer no. 33205,  $E_B = 5.82 \times 10^5$ , Eq. (12) becomes

$$\begin{aligned} \int_0^{w_0} \alpha(E) dw &= \alpha(E_B) w_0 [1 - (3 - 2(b/E_B)^2)(b^2/3E_B^4) \left(\frac{V_{BI}}{w_0}\right)^2] \\ &= 0.985 \alpha(E_B) w_0 \quad (15) \end{aligned}$$

so that the difference between using the square well and the triangular profile of Fig. 45 is only 1.5 percent.

The computer program used to analyze this data has been built with three options for the field for  $w < w_0$ : the constant field, the triangular approximation, and the quadratic approximation. The differences in the derived values of  $\alpha$  are negligible, as would be expected from the preceding argument.

The measured breakdown voltages are listed in Table 11. Since the total voltage at each temperature is the area under the curve in Fig. 44, we can find how far the "iceberg" must be lifted up, i.e., we can find the value of  $E_B$  as a function of temperature. This is done with a computer program which operates on the C-V data, and the results are listed in the last column of Table 11. Since  $E_B$  is the constant field and Fig. 44 shows that the field drops precipitously outside  $w_0$ , it would be a reasonable approximation to take

TABLE 11

TEMPERATURE DEPENDENCE OF DEVICE 6 FROM WAFER NO. 33205

T (°C)	V <sub>B</sub> Volts	V <sub>B</sub> +V <sub>BI</sub> Volts	E <sub>0</sub> 10 <sup>5</sup> V/cm	E <sub>B</sub> 10 <sup>5</sup> V/cm
-20	15.05	16.45	4.48	5.67
1	15.57	16.97	4.54	5.73
25	16.29	17.69	4.63	5.82
50	17.03	18.43	4.71	5.90
75	17.71	19.11	4.79	5.98
100	18.44	19.84	4.88	6.07

$\alpha_{\text{eff}}$  to be  $1/w_0$  at  $E = E_B$ , which would amount of  $\alpha_{\text{eff}} = 8.5 \times 10^4 \text{ cm}^{-1}$  for this wafer at the breakdown condition. Actually, the computer calculation shows that spillover accounts for 15 percent of the integral  $\int \alpha_{\text{eff}} dw$  so that at breakdown  $\alpha_{\text{eff}} = 7.2 \times 10^4$ .

From the first and last columns of Table 11, we find the field that is required at different temperatures to make  $\alpha_{\text{eff}}$  equal to  $7.2 \times 10^4$ . Over the limited range of field, this curve is approximately a straight line as shown in Fig. 46 for devices nos. 3 and 6. From this wafer, the relation  $\frac{\partial \alpha}{\partial T} = -330 \frac{\partial \alpha}{\partial E}$  is satisfied at these values of E and T.

The variation in the measured breakdown voltage between different devices from wafer no. 33205 appears to be about  $\pm 0.1$  volt, while the error in estimating the breakdown voltage from I-V curves is considered to be on the order of 0.04 volts. For some wafers, the device-to-device variation in breakdown voltage is much larger than it is for this particular wafer. It should be noted that, because of the dimensions of the drift zones in this wafer, an error of 0.1 V results in an error of only  $0.01 \times 10^5 \text{ V/cm}$  in  $E_B$ .

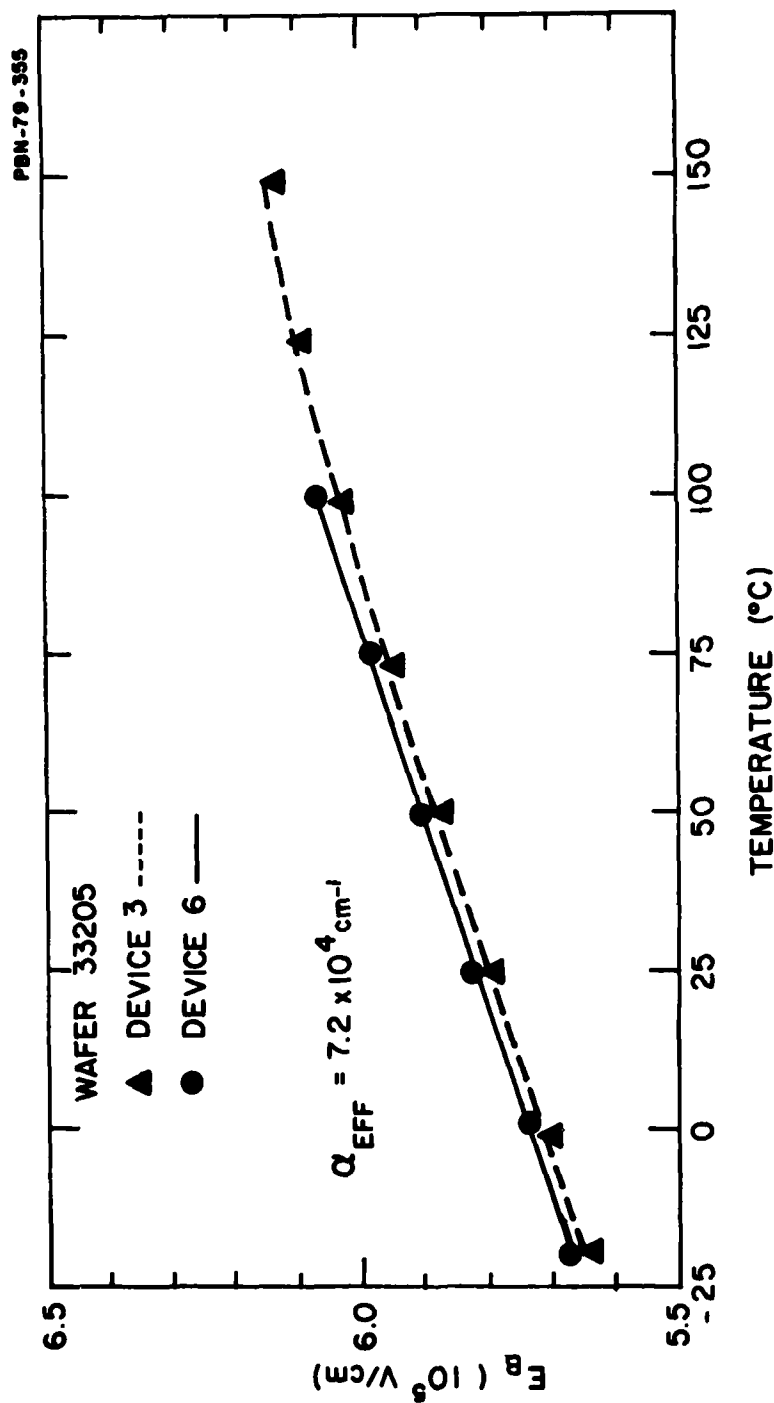


Figure 46. Plot of the Electric Field Producing an Electron Ionization Coefficient of  $7.2 \times 10^4 \text{ cm}^{-1}$  for Various Temperatures as Measured on Devices No. 3 and No. 6. The partial derivatives of  $\alpha(E, T)$  are related by  $\partial \alpha / \partial T = -330 \partial \alpha / \partial E$ .

### 5.3.2 Other wafers

The functional behavior of the ionization coefficient is traditionally written as

$$\alpha_{\text{eff}} = a \exp[-(b/E)^M] \quad (16)$$

where  $M$  is taken as either (1) or (2). Over the range of interest, the choice of  $M$  does not have a strong effect on the plot of  $\alpha$  provided that  $a$  and  $b$  are chosen appropriately in each case, but  $M = 2$  is more commonly chosen for GaAs.

For a given wafer, the breakdown condition does not determine both  $a$  and  $b$ , but instead a curve is determined which gives  $a$  as a function of  $b$ . Any point on this curve will satisfy the breakdown condition for that particular wafer. The four curves determined in this way by the four wafers in Fig. 40 are shown in Fig. 47, for  $M = 2$  and room temperature. If Eq. (16) were exact and there were no experimental error, the four curves would presumably intersect at a single point. Although neither of these conditions is precisely true, all four curves come close to the point indicated in Fig. 8, at  $a = 1.61 \times 10^5 \text{ cm}^{-1}$  and  $b = 5.41 \times 10^5 \text{ V/cm}$ .

The two steeper curves, for wafers nos. 91216 and 51165, had relatively low peak fields with  $E_B = 3.99$  and  $4.53 \times 10^5 \text{ V/cm}$ , respectively. The flatter curves, for wafer nos. 33205 and 32506 had high peak fields with  $E_B$  equal to  $5.84$  and  $5.92 \times 10^5 \text{ V/cm}$  respectively.

A similar series of plots can be made for the case  $M = 1$ , as shown in Fig. 48. For the case  $M = 1$ , the best fit to the four wafers in this case is  $a = 7.9 \times 10^5 \text{ cm}^{-1}$  and  $b = 1.42 \times 10^6 \text{ V/cm}$ .

The same methods were used to reduce the breakdown voltage data measured at other temperatures, which allows us to obtain values of  $a$  and  $b$  as functions of temperature.

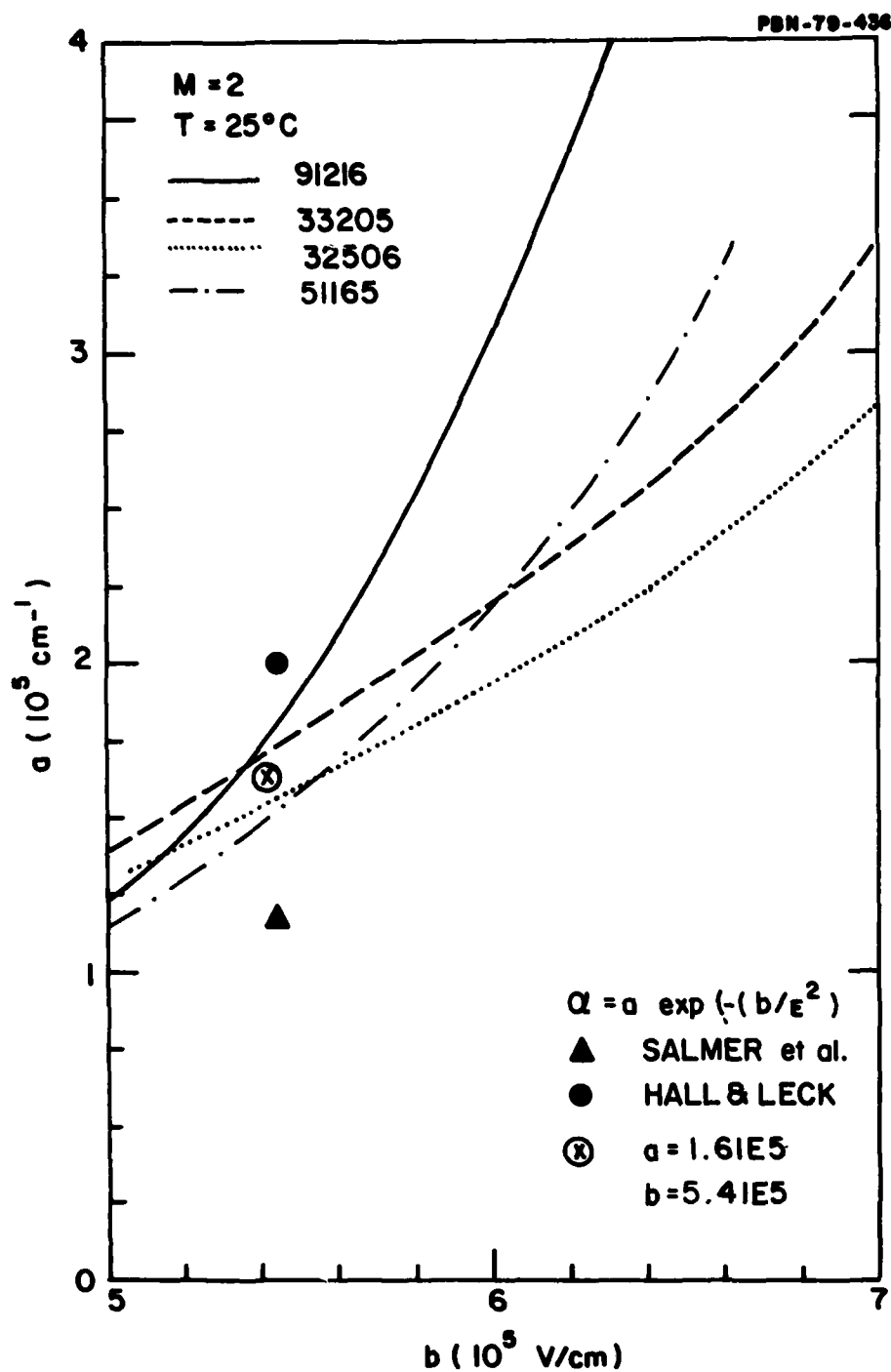


Figure 47. Curves of  $a$  vs.  $b$  for Specific Wafers, with  $M = 2$ . For a specified value of  $b$ , the value of  $a$  required to give the measured breakdown voltage is plotted.



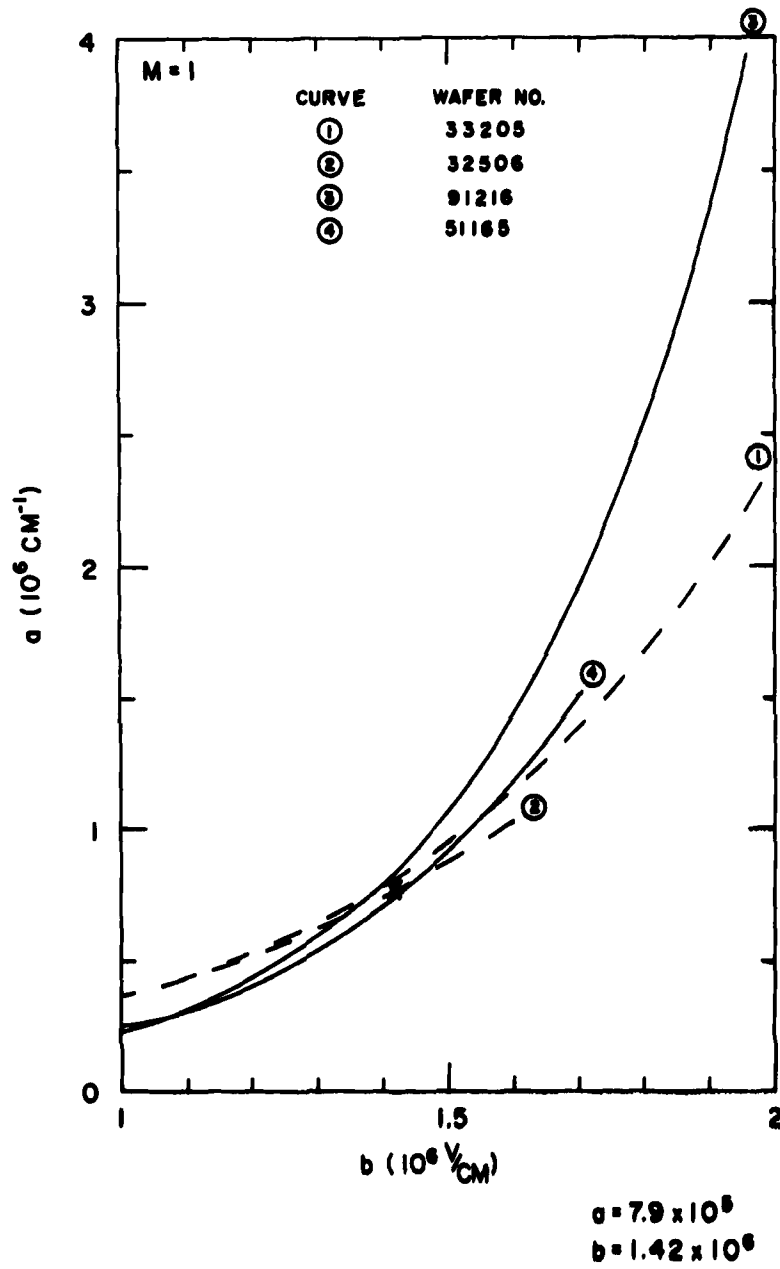


Figure 48. Curves of  $a$  vs.  $b$  for  $M = 1$ . The curves are for the same wafers as in Fig. 47.

#### 5.4 Results

The data reduction described in the previous section resulted in the constants

$$\begin{aligned} M &= 2 \\ a &= 1.61 \times 10^5 \text{ cm}^{-1} \\ b &= 5.41 \times 10^5 \text{ V/cm} \end{aligned} \tag{17}$$

which determine the ionization coefficient at room temperature.

The points from 3 of our wafers are shown as X's in Fig. 49, and compared with the functional form given by the parameters in Eq. (17), with Ito's values (1978) and with Salmer's values (1973). (Wafer 91216 fell outside the range of this figure). Ito et al. (1978) were the only other experimenters who reported  $\alpha$  at fields above  $5 \times 10^5$  V/cm. Ito gave his experimental results by fitting them to the exponential with  $M = 1$ , but it is interesting to note from Fig. 49 that his results are close to a straight line such as would be obtained if  $M = 2$ . Salmer's results for these fields are only an extrapolation from measurements at lower fields, but they are shown because they have often been used in IMPATT diode design. The unpublished results by Holway (1977) were obtained from Schottky-barrier Read-type IMPATT diodes at fields near  $6 \times 10^5$  V/cm.

A convenient way to express the temperature dependence of the effective ionization coefficients is to write

$$\begin{aligned} a &= a_0 [1 + c_a (T - 25)] \\ b &= b_0 [1 + c_b (T - 25)] \end{aligned} \tag{18}$$

where  $a_0$  and  $b_0$  are the coefficients at 25°C given by Eq. (17) and  $T$  is the temperature in °C. By matching our experimental results as a function of temperature with the coefficients in Eq. (18) we obtain

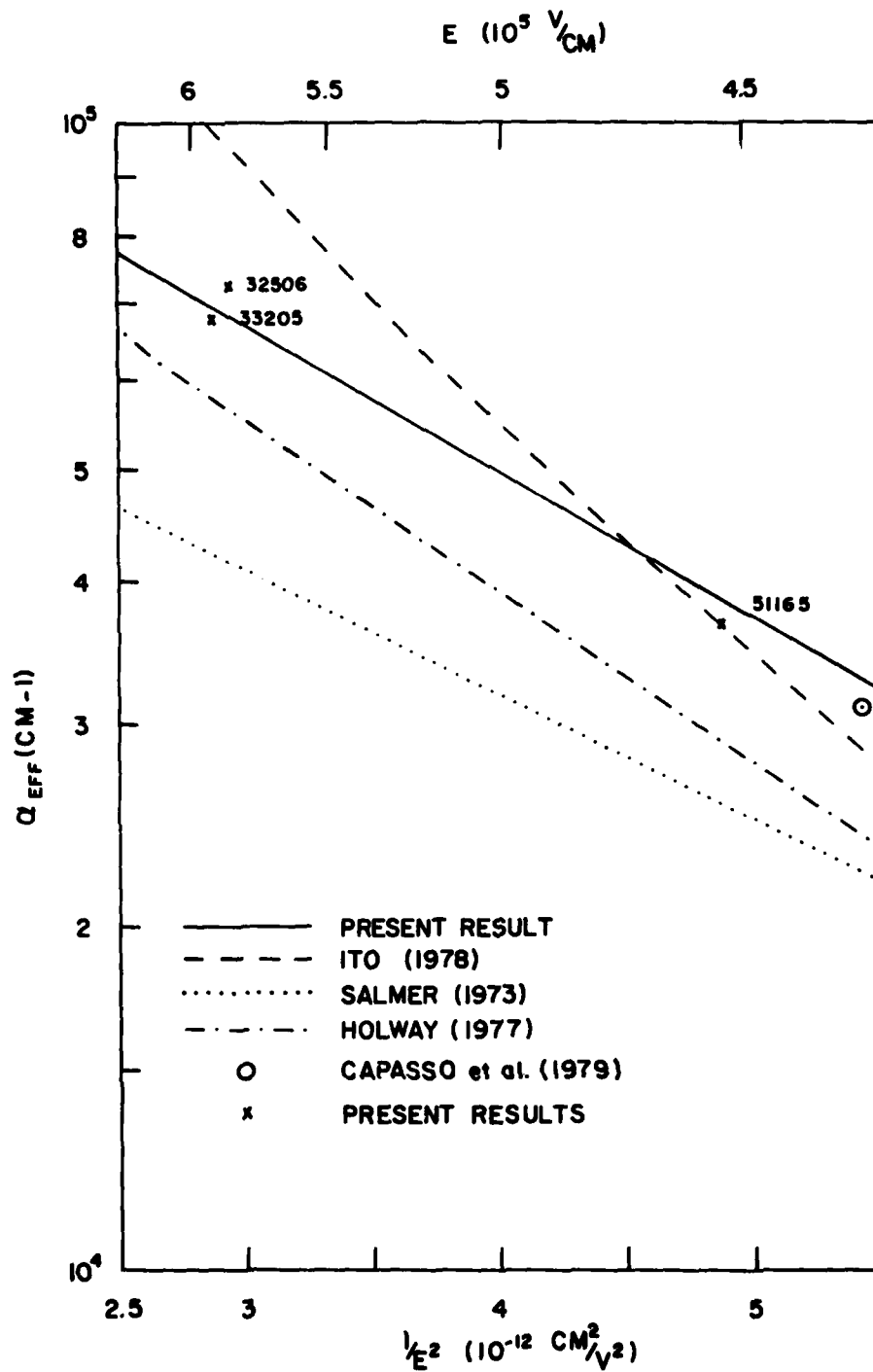


Figure 49. Comparison of Ionization Coefficients from the Present Experiment with the Results of Earlier Investigators.

$$\begin{aligned} c_a &= .00070 \\ c_b &= .00097 \end{aligned} \tag{20}$$

The form of Eq. (18) appears to have originated with Hall and Leck (1968).

### 5.5 Discussion of Results

The effective ionization coefficient has been measured at fields close to  $6 \times 10^5$  V/cm. The results are considerably higher than the values given by Salmer et al. This is consistent with our earlier observations (Holway, 1977) with Schottky-barrier Read IMPATT diodes where the breakdown voltages calculated using the Salmer coefficients were considerably above the measured breakdown voltages.

The ionization coefficients were measured in  $n^+p$  and  $p^+n$  diodes, as well as with double-drift diodes. The results were consistent with the expectation that the ionization coefficients were independent of the dopant.

The measurements were made with Read profiles. A new technique was developed to determine the electric field profile from the mesa C-V data. These profiles allow us to have large and nearly constant fields in the avalanche region. It would be useful to carry out photomultiplication experiments with such profiles to measure  $\alpha$  and  $\beta$  separately at high fields. The C-V technique would eliminate errors which could occur in flat profiles when these are distorted due to impurity diffusion. This diffusion might be a problem, for example, near  $p^+n$  junctions where it could distort a flat profile.

Our high field measurements are in good agreement with the values of  $\alpha$  measured by Ito et al. (1978), although our results are slightly below their values. If we accept the value of  $k(E) = \beta/\alpha$  given by Ito et al. and the present value of  $\alpha_{eff}$ , we can calculate the values of  $\alpha$  and  $\beta$  using Eq. (2). The results are compared with those of Ito et al. in Fig. 50.

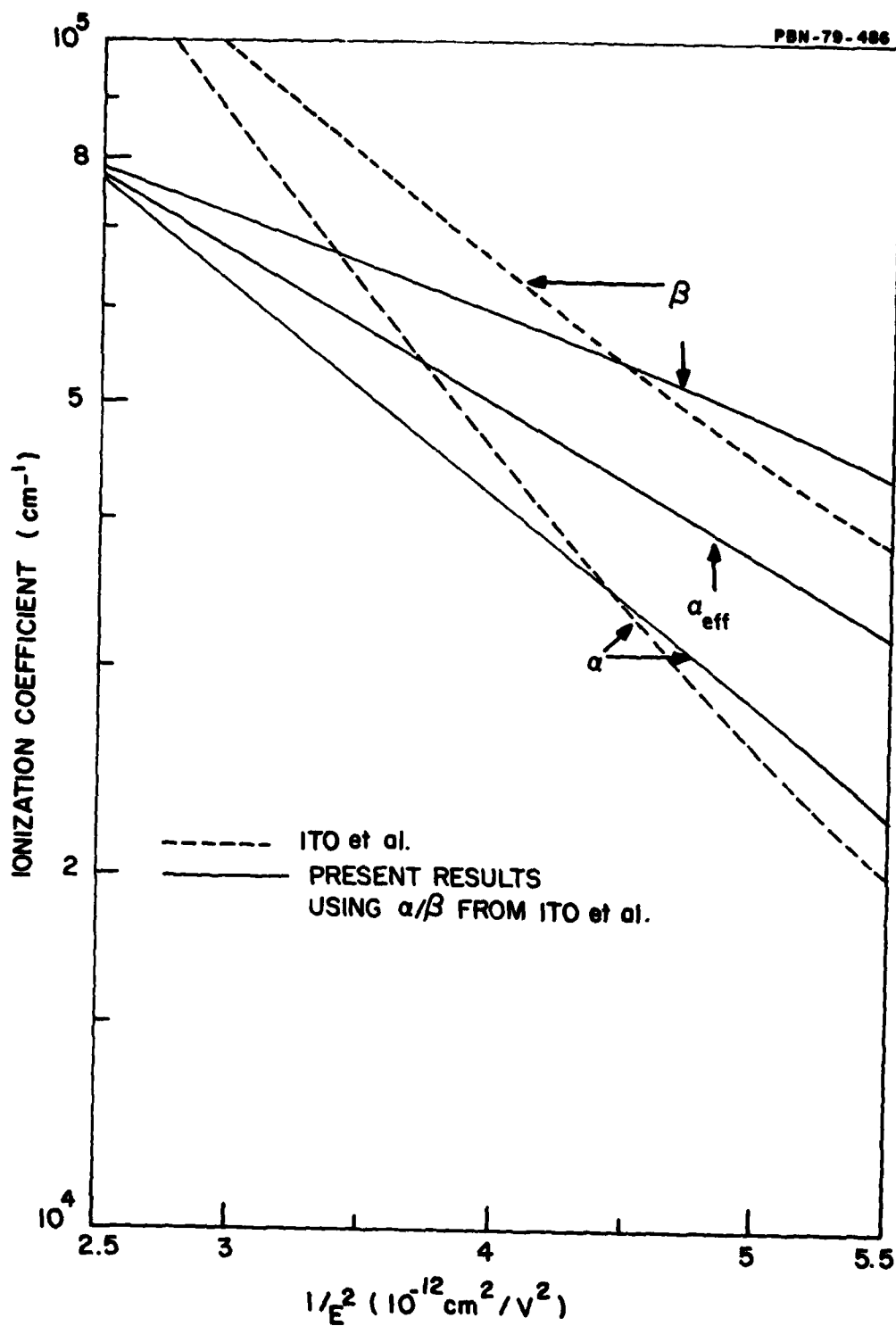


Figure 50. Values of  $\alpha$  and  $\beta$ . These were obtained by using our values of  $\alpha_{\text{eff}}$  and Ito's values for  $k$ . The dashed curve is from Ito's paper.

## SECTION VI

### PROGRAM ACHIEVEMENTS AND RECOMMENDATIONS

#### 6.1 Introduction

At the beginning of this program, the rapid development of double-drift GaAs IMPATT diodes at X-band was being retarded by limited knowledge of the optimum growth conditions and the basic physical properties of p-type GaAs. Although p-type material with doping levels suitable for X-band double-drift devices was grown before this program began, profile control was sometimes erratic and wafer yield was poor. There was also a serious need for further data on hole velocities and ionization coefficients at the temperatures and electric fields existing in double-drift devices. This program set out to address these problems.

#### 6.2 Overall Results

In the first task of this program, we explored three p-type doping techniques, one involving zinc alkyl, and two involving zinc iodide formed as needed by chemical reaction. The zinc alkyl process was found to be chiefly useful for  $p^{++}$  contacts; the two zinc iodide processes gave useful p-doping at levels suitable for devices from X- to Ka-band.

In the second task of this program, we measured hole velocities as a function of electric field and temperature. Our velocities averaged about 70 percent of those reported previously. We also determined ionization coefficients at very high fields ( $6 \times 10^5$  V/cm) typical of high power Ka-band devices. These are in rough agreement with values reported by Ito et al. (1978).

In the third task, we grew X-band and Ka-band p-type low-high-low Read wafers with good reproducibility using the zinc iodide formed as needed by chemical reaction.

### 6.2.1 Epitaxial growth

Prior to this program we had explored p-type doping using prepared mixtures of zinc alkyls in hydrogen. In experiments over a two-year period we found that doping at levels greater than  $10^{17}$  holes  $\text{cm}^{-3}$  could be achieved with good reproducibility, but that doping at lower levels was erratic — the more so at the lowest levels. These results were verified in the early stages of this contract.

Much more reproducible results were achieved using zinc iodide formed as needed by reacting dilute hydrogen iodide with heated zinc arsenide. When this system was operating properly, abrupt changes in doping were feasible, and reasonable reproducibility was achieved. Unfortunately, the concentration of the hydrogen iodide mixture procured from the vendor was frequently uncertain, sometimes varying by as much as a hundredfold from the specified level in low-concentration mixtures. This was a source of great trouble in achieving adequate process control. We also found it difficult to obtain reliable analyses of the hydrogen iodide concentration in the gas cylinders, so that we often had to use a cylinder for some time to determine its true concentration. This was an inefficient and costly procedure.

To minimize this difficulty we set up a system that uses iodine vapors as the reagent to react with the heated zinc arsenide. This process yielded better control because the iodine concentration was a function of the iodine vaporizer temperature. The process itself, however, behaved differently, and the reaction dynamics were greatly altered. The p-doping per iodine atom was increased manyfold and the turn-on and turn-off behavior were altered. In the limited time available on this contract we were unable to optimize all of the parameters affecting this system. However, we were able to obtain sufficient understanding of the system that we were able to demonstrate the reproducible growth of p-type Read wafers with  $n^{++}$  contacts. In addition,  $p^{++}$ - $p$ - $p^{++}$  layers were readily grown to specifications for hole velocity samples.

We developed procedures to grow abrupt junctions on p-type layers, using silane to grow the  $n^{++}$  contacts. By all measures, the junctions appeared to be abrupt, with little compensation at the interface between the p and the  $n^{++}$  layers. However when mesa diodes were formed from wafers containing these junctions, we invariably measured excessive leakage currents in reverse bias before avalanche. This phenomenon remains unexplained. On the other hand, we can consistently grow high quality p:n junctions if we grow the n-type layer before the p-type layer. Zinc diffusion does not appear to be a problem in the as-grown junctions.

We found it possible to grow on zinc doped substrates by introducing a suitable growth pause. Without the growth pause, autodoping from the substrate produced a p-type background in the low  $10^{16}$  holes  $\text{cm}^{-3}$  range.

At the end of the program we successfully grew X-band and p-Read structures, and Ka-band p-Read structures with good control of the doping profile. These were grown on semi-insulating substrates with a highly doped p-type layer adjacent to the substrate.

#### 6.2.2 Wafer characterization

We found it possible to characterize p-type wafers with only minor modifications of the procedures we routinely use to characterize n-type wafers. We used aluminum Schottky diodes of standard area upon step-etched samples to determine doping profiles. Since the Schottky barrier is smaller in the case of the p-type material, less depth could be measured on a diode before excessive leakage occurred; however, adequate information could be obtained upon multiple step-etched samples.

Mobilities were obtained in the usual way, using van der Pauw samples, with AgMn or indium alloyed contacts.

Etched mesa samples were used to measure the characteristics of p:n junctions.



### 6.2.3 Physical measurements

Hole velocities were measured as a function of temperature and electric field. The saturated hole velocities measured on the present program were found to be about 70 percent of those reported by Dalal (1970, 1971). A great deal of effort was expended to verify our measurements and to explain the discrepancy between our results and those of Dalal but no satisfactory explanation has been forthcoming. Our results appear to be of the right magnitude to correlate with double-drift device performance.

We derived ionization coefficients as a function of temperature. Our results are in good agreement with those published by Ito et al. (1978). These two sets of measurements are the only data available at the high fields existing in Ka-band Read devices.

### 6.3 Deliveries

Beginning with the second month of the program a representative wafer was delivered to the Air Force at the end of each monthly period.

The final delivery at the end of the contract consisted of two p-type Read wafers, one designed for X-band, and one designed for Ka-band, grown on semi-insulating substrates. These were provided with highly doped  $n^{++}$  contact layers forming a junction located a few tenths of a micron from the  $p^{++}$  spike of the low-high-low p-Read structure.

Characterization data accompanied each wafer delivered.

### 6.4 Recommendations for Future Work

Although a great deal has been accomplished recently in making p-type epitaxy more nearly equivalent to n-type epitaxy, further work is desirable. In particular, a better understanding of the mechanisms operative in iodine transport is needed to obtain better control of this system.

In physical measurements, more work ought to be carried out to explain the observed discrepancies between the present measurements of hole velocities and those of Dalal. Additional work in ionization coefficient measurements would also be fruitful, although the need is not confined to p-type material.

Additional p-type Read IMPATT structures ought to be grown with  $n^{++}$  contacts to resolve the problem of excessive leakage at the junction. Once low leakage structures are achieved, devices ought to be fabricated and tested in rf circuits to help optimize the p-side of double-drift diodes. This is probably the most important work which should be carried out in future programs.

## REFERENCES

- Adlerstein, M.G., R. N. Wallace, and S. R. Steele, Electron. Lett. 11, 1975, 430.
- Adlerstein, M.G., R. N. Wallace, and S. R. Steele, Trans. Elec. Dev. ED-25, 1978, 1151.
- Capasso, F., R. E. Mahory, and M. A. Pollack, Electron. Lett. 16, 1979, 126.
- Conrad, R. W., and R. W. Haisty, J. Electrochem. Soc. 113, 1966, 199.
- Dalal, V. L., Appl. Phys. Lett. 16, 1970, 489.
- Dalal, A. B. Dreeben, and A. Triano, J. Appl. Phys. 42, 1971, 2864.
- Decker, D. R., J. Electrochem. Soc., Solid State Science, 1968, 1085.
- Ettenburg, M., and C. J. Nuese, J. Appl. Phys. 46, 1975, 3500.
- Goldwasser, R. E., S. I. Long, and P. Terzian, Trans. 5th Biennial Conf. on Active Semiconductor Devices for Microwaves, Cornell Univ., 1975, 367.
- Hall, R., and J. H. Leck, Int. J. Electron. 25, 1968, 539.
- Handbook of Chemistry and Physics, 37th Ed., Cleveland: Chemical Rubber Publishing Co., 1955, 2166.
- Hierl, T. L., J. J. Berenz, and S. I. Long, Trans. 6th Biennial Conf. on Active Semiconductor Devices for Microwaves, Cornell Univ., 1977, 211.
- Hilibrand, J., and R. D. Gold, RCA Review 21, 1960, 245.
- Holway, L. H., Jr., Int. J. Electron. 41, 1976, 411.
- Holway, L. H., Jr., Raytheon Research Division Technical Memorandum T-1023, 1977.

- Houston, P. A., and A.G.R. Evans, Solid-St. Electron. 20, 1977, 197.
- Ito, M., S. Kagawa, T. Kaneda, and T. Yamaoka, J. Appl. Phys. 49, 1978, 4607.
- Kennedy, D. P., P. C. Hurley, and D. Kleinfelder, IBM J. Res. and Dev. 12, 1968, 399.
- Kim, C. K., S. R. Steele, and R. W. Bierig, Electron. Lett. 9, 1973, 173.
- Kuvas, R. L., Electron. Lett. 12, 1976, 143.
- Law, H.D., and C. A. Lee, Solid-St. Electron. 21, 1978, 331.
- Masse, D. J., S. G. Chu, K. K. Johnson, and P. Whittier, presented at the 8th European Microwave Conf., Paris, 1978.
- Munir, A., M. E. Benavides, and D. J. Meschi, High Temp. Sci. 6, 1974, 73.
- Salmer, G., J. Pribetich, A. Farrrayre, and B. Kramer, J. Appl. Phys. 49, 1973, 314.
- Schoonmaker, R. C., and K. L. Lemmerman, J. Chem. Eng. Data 17, 1972, 139.
- Schroder, W. E., and G. I. Haddad, Proc. IEEE 59, 1971, 1245.
- Seidel, T. E., and D. L. Scharfetter, J. Phys. Chem. Solids 28, 1967, 2563.
- Siderov, Yu. G., L.F. Vasileva, I. V. Sabinina, S. A. Dvoretzky, and A. V. Siderova, J. Electrochem. Soc. 123, 1976, 698.
- Silvestri, V. J., and F. Fang, J. Electrochem. Soc. 111, 1964, 1164.
- Steele, S.R., S. P. Runowicz, and K. K. Johnson, Gallium Arsenide and Related Compounds, Conf. Series No. 45, The Inst. of Physics, Bristol and London, 1979, 45-51.
- Steele, S.R., J. W. Thompson, and R. W. Bierig, Trans. 5th Biennial Conf. on Active Semiconductor Devices for Microwaves, Cornell Univ., 1975, 23.
- Stillman, G. E., Conf. Series 33a, The Inst. of Physics, Bristol and London, 1977, 155.
- Stillman, G. E., C. M. Wolfe, J. A. Rossi, and A. G. Foyt, Appl. Phys. Lett. 24, 1974, 471.
- Urgell, J., Electron. Lett. 4, 1968, 447, and Electron. Lett. 5, 1969, 16.
- Van Opdorp, C., Solid-St. Electron. 11, 1968, 397.

Wallace, R. N., S. R. Steele, and M. G. Adlerstein, Trans. 6th Biennial  
Conf. on Active Semiconductor Devices for Microwaves, Cornell Univ.,  
1977, 195.

Wolfe, C. M., G. E. Stillman, and W. T. Lindley, Symp. on GaAs, 1968, 43.